Chem Soc Rev

REVIEW ARTICLE

View Article Online
View Journal | View Issue





Cite this: *Chem. Soc. Rev.*, 2017, **46**, 4774

# Metal–organic frameworks meet metal nanoparticles: synergistic effect for enhanced catalysis

Qihao Yang,[a] Qiang Xu [bc] and Hai-Long Jiang *[a]

Metal–organic frameworks (MOFs), established as a relatively new class of crystalline porous materials with high surface area, structural diversity, and tailorability, attract extensive interest and exhibit a variety of applications, especially in catalysis. Their permanent porosity enables their inherent superiority in confining guest species, particularly small metal nanoparticles (MNPs), for improved catalytic performance and/or the expansion of reaction scope. This is a rapidly developing interdisciplinary research field. In this review, we provide an overview of significant progress in the development of MNP/MOF composites, including various preparation strategies and characterization methods as well as catalytic applications. Special emphasis is placed on synergistic effects between the two components that result in an enhanced performance in heterogeneous catalysis. Finally, the prospects of MNP/MOF composites in catalysis and remaining issues in this field have been indicated.

Received 8th October 2016

DOI: 10.1039/c6cs00724d

rsc.li/chem-soc-rev

[a] *Hefei National Laboratory for Physical Sciences at the Microscale, CAS Key Laboratory of Soft Matter Chemistry, Collaborative Innovation Center of Suzhou Nano Science and Technology, Department of Chemistry, University of Science and Technology of China, Hefei, Anhui 230026, P. R. China. E-mail: jianglab@ustc.edu.cn; Fax: +86-551-63607861; Tel: +86-551-63607861*

[b] *Research Institute of Electrochemical Energy, National Institute of Advanced Industrial Science and Technology (AIST), 1-8-31 Midorigaoka, Ikeda, Osaka 563-8577, Japan*

[c] *AIST-Kyoto University Chemical Energy Materials Open Innovation Laboratory (ChEM-OIL), Yoshida, Sakyo-ku, Kyoto 606-8501, Japan*

## 1. Introduction

Metal–organic frameworks (MOFs), also known as porous coordination polymers (PCPs), have captured widespread interest and have become one of the fastest growing fields in both chemistry and materials science in the last two decades.[1–3] As a class of porous crystalline materials, MOFs feature periodic network structures formed by self-assembly of inorganic metal-containing nodes (metal ions/clusters, also known as secondary building units or SBUs)

**Qihao Yang**

*Qihao Yang was born in 1991 in Ningbo, China. He received his BS degree (2014) in chemistry from Zhejiang Normal University. He is currently a PhD student under the guidance of Prof. Hai-Long Jiang at the University of Science and Technology of China, working on the synthesis and catalytic applications of metal nanoparticles incorporated into metal–organic frameworks.*

**Qiang Xu**

*Qiang Xu received his PhD degree in 1994 from Osaka University. He is Director of the AIST-Kyoto University Chemical Energy Materials Open Innovation Laboratory (ChEM-OIL), Prime Senior Researcher at AIST, Adjunct Professor at Kobe University and at Kyoto University, and Distinguished Honorary Professor at The Hong Kong Polytechnic University. He received the Thomson Reuters Research Front Award in 2012 and was recognized as a highly cited researcher (2014/2015/2016) in both Chemistry and Engineering by Thomson Reuters. His research interests include the chemistry of nanostructured materials and their applications, especially for energy. He is a member of the European Academy of Sciences (EURASC).*

and organic linkers.[4–10] The organic linkers are enormously diverse, are mostly based on carboxylates, N-donor groups, or even phosphonates, and have a variety of configurations. The vast number of metal ions and organic linkers available as well as their diverse assemblies have led to more than 20 000 MOFs being reported, whose structures are not only abundant and intriguing but also designable and tailorable. In addition to their diverse structures and compositions, MOFs possess uniform pore sizes/environments and very high surface areas in contrast to traditional microporous and mesoporous materials, including zeolite, mesoporous $SiO_2$, and activated carbon. These inherent features render MOFs very promising in a variety of applications, such as gas sorption and separation, heterogeneous catalysis, drug delivery, proton conductivity, and sensing.[1–3,11–48]

Amongst different MOF applications, the study of catalysis started very early and is becoming one of the most rapidly growing applications. The main reasons behind this are the inherent properties and remarkable advantages of MOFs toward catalysis: MOFs possess high-density and uniform dispersion of active sites; highly porous structures that render all active sites readily accessible; open channels that greatly facilitate the transport and diffusion of substrates and products; and a solid character that guarantees recyclability. Therefore, MOFs effectively integrate the advantages of both homogeneous and heterogeneous catalysts, with high reaction efficiency and recyclability. In addition, MOFs possess highly uniform pore shapes and sizes, which are of vital importance for size-selective catalysis: small reactants can be effectively converted while molecules larger than the pores will not be able to react. The pore sizes of MOFs are continuously tunable and bridge the gap between zeolite (microporous) and silica (mesoporous);[49] thus, they are applicable to many important reactions. Moreover, MOFs show excellent ability in realizing molecular-level tuning in their structures. Each atom in MOF structures is precisely determined and most of them are tailorable. Particularly, many isoreticular MOFs with alterable functional groups grafted on their pore walls have been reported, *via* either one-step assembly or post-synthetic modification.[50] All these factors make MOFs ideal candidates for the study of structure–activity relationships based on catalysis.[51–55]

Despite the advantages of MOFs for catalysis, as indicated above and also in previous reports,[16,31,36,56–59] the type of active sites on MOF structures is mainly limited to the following two sources, resulting in reactivity toward limited catalytic reactions. (1) Unsaturated metal centers, behaving as Lewis acidic sites, are intensively reported and usually made available by the removal of coordinated solvents upon activation.[60,61] Also, the creation of structural defects on or around the metal clusters was recently reported to lead to remarkable activity.[51] (2) Active sites grafted on the organic linkers are very common. The benzene rings are usually involved in the linkers and they can be modified to connect with additional acidic (–OH, $–SO_3H$), basic ($–NH_2$, –NH, –N), or even diverse groups, resulting in activity originating from the nature of the functional groups. The modified linkers can be directly used during the one-step synthesis of MOFs based on 100% or just a certain proportion of replaced parent linkers.[33,62–64] If the additional active sites take part in the coordination with metal ions or disturb the formation of expected MOF structures, they can be alternatively post-synthetically grafted onto the linkers.[50,65,66]

In addition to the above two approaches introducing active sites into MOF structures, being a class of porous materials, MOFs can incorporate catalytically active guest species into their pore spaces, or they can be partially stabilized on the MOF surface.

Given the diversified organic/inorganic guests available for encapsulation, this strategy greatly promotes the applications of MOFs for catalysis not only with respect to improved performance but also toward a broad scope of reactions that are not attainable by the individual components.

As one of the most promising guest species, metal nanoparticles (MNPs), particularly small MNPs, are rapidly attracting intense interest due to their great importance in catalysis. Unfortunately, due to the high surface energy of small MNPs, they are thermodynamically unstable and prone to aggregate during catalytic reactions, leading to a loss of activity. Consequently, control of the size, shape, and dispersion of MNPs is a critical factor in achieving high and stable activity. To this end, various surface capping agents, such as polyvinylpyrrolidone (PVP), oleylamine, and dendrimers, are commonly accepted to obtain small MNPs with particular shapes. While this has been recognized as an effective solution, capping molecules attached to MNPs with strong chemical interactions are, in most cases, undesired and play negative roles in catalysis. To obtain well dispersed MNPs with clean surfaces, their confinement inside porous materials, for example, porous silica, zeolites, and porous carbons, is paramount for subsequent catalysis.[67–69] Porous materials offer inherent conditions for spatial confinement to prevent the MNPs from aggregation and growth, and their pores serve as a transfer path for the reaction substrates/products. Amongst porous materials, MOFs are the most popular choices because (1) they are versatile with different pore sizes and shapes

**Hai-Long Jiang**

*Hai-Long Jiang received his PhD (2008) from the Fujian Institute of Research on the Structure of Matter, Chinese Academy of Sciences, and then worked with Prof. Qiang Xu at AIST (Japan) as a postdoc and JSPS fellow from 2008–2011. After a postdoctoral stint at Texas A&M University (USA) with Prof. Hong-Cai Zhou, he joined the faculty of the University of Science and Technology of China in 2013. He has published more than 90 papers with over 7000 citations (H index 41). His main research interest is the development of crystalline porous and nanostructured materials, crossing coordination chemistry and nanoscience, for energy-/environment-related catalysis.*

for the particular requirements of MNPs; (2) they possess very high porosity and surface areas, which is desirable for hosting MNPs; (3) the well-defined MOF structures and easily tailorable pore architectures enable clear surrounding environments for MNPs, which are preferable for understanding catalysis.

The combination of MNPs and MOFs for new or enhanced properties, particularly in catalysis, has attracted a surge of research interest in recent years. Previous reviews mainly summarize the preparation and characterization methods of MNP/MOF materials as well as their applications.[46,70–80] Along with ~10 years of active research in this field, we are gradually becoming aware that functional synergy between MNPs and MOFs is of great significance in their catalysis. That is, the rational integration of these two components effectively synergizes their respective strengths and offsets their drawbacks for enhanced catalysis. However, the importance of synergistic catalysis over MNP/MOF composites is far from being well understood. Being at the early stages of the study of MNPs/MOFs, most reports are focused on the stabilization of MNPs by MOFs and discuss the good catalytic properties of MNPs, which represent the simplest functional synergy between the two components. Our most recent reports have clearly demonstrated that the synergistic effect between MNPs and MOFs effectively integrates their respective multiple advantages, resulting in a much enhanced catalytic performance.[81–83]

Therefore, we believe it is time to highlight the synergistic effects in this field. In the present review, we provide an overview of MNP/MOF composites for catalysis. For the completeness of this review, we first summarize the synthetic protocols and characterization tools for MNPs/MOFs (MNPs are loaded into and/or on the surface of MOFs) and MNPs@MOFs (generally, MNPs are only incorporated into MOFs) and discuss some important concerns. Most importantly, particular emphasis is placed on the synergistic effects between the two components in MNP/MOF composites for enhanced catalysis (Scheme 1). Hopefully, this review will inspire the interest and enthusiasm of scientists in chemistry and materials science, who are encouraged also to read the cited articles, leading to deeper understanding and insight into the study of MNP/MOF composites, which thus in turn will promote the further development of related research fields.

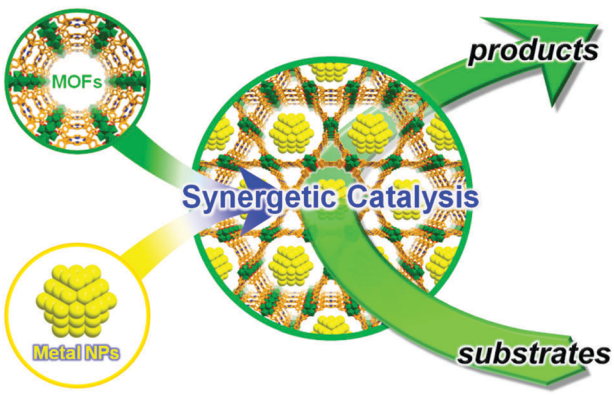


Scheme 1 Schematic illustration showing the integration of the functions of MOFs and metal NPs for synergistic catalysis.

## 2. Synthetic approaches to the formation of MNP/MOF composites

Diverse synthetic methods to stabilize MNPs with MOFs have been developed. In general, the preparation of MNP/MOF composites can be classified into four approaches. The first approach is the introduction of a MOF into a solution with a metal precursor (or the mixing of a MOF with a metal precursor in the solid state), followed by the formation of MNPs inside and/or on the external surface of the MOF. The second is the dispersion of MNPs into a reaction solution for subsequent MOF synthesis, generally, to obtain MNPs incorporated into MOFs. The third is step-by-step synthetic processes, for MNPs/MOFs and sandwich-like structured MOF/MNPs/MOFs. The last step is the simultaneous formation of the two components to afford MNP/MOF composites. The reported examples of MNP/MOF composites synthesized using the first approach are summarized in Table 1.

### 2.1. Synthesis of MOFs prior to the formation of MNPs

Using MOFs as stabilizing host materials provides a confined space for MNPs *via* a "ship-in-a-bottle" approach, in which the incorporation of MNPs in a MOF matrix is expected to prevent agglomeration and restrict the growth of MNPs. It should be noted that it remains a significant challenge to confine all the MNPs inside the pores, and supporting a few MNPs on a MOF surface is sometimes unavoidable. This issue arises from the influence of the MOF microstructure, which involves inner surface characteristics, interactions between the metal precursors or MNPs and the MOF pore surface environment, and the dynamics of wetting and filling MOF pores. In a traditional approach, the introduction of metal precursors can be based on different techniques including solution infiltration, vapour deposition, and solid grinding, followed by various reduction methods (for example with hydrogen, ammonia borane, $NaBH_4$, and hydrazine) for metal precursors, resulting in different sizes and/or distribution control of MNPs relative to MOF particles. The reducing agent, reduction method, and reduction time, which significantly affect the size of MNPs, should be carefully chosen, considering the chemical and thermal stability of the host MOFs.

**2.1.1. Solution impregnation.** In this system, MOF crystals are introduced into a solution containing the metal precursor and mixed effectively. The existing capillary pressure causes the liquid (containing metal precursor) to spontaneously penetrate the interior voids of the MOFs. The solid was then collected by centrifugation and washing, or only evaporation. Subsequently, the metal precursors are reduced to MNPs. In this way, the size and shape of MNPs, formed *in situ*, are expected to be determined by the cavities of the host MOF. The particle distribution depends on the metal precursor and MOF, and some of the metal precursor might be adsorbed on the surface and easily migrate. For this reason, the MNP/MOF composites synthesized

 

Table 1 Summary of the reported MNP/MOF composites

| Preparation method | MOF | Metal precursor | Reduction method | Particle size (nm) | Ref. |
|---|---|---|---|---|---|
| Solution impregnation | MOF-5 | $Pd(acac)_2$ | Vacuum heating or $H_2$ | — | 84 |
| | | $PdCl_2$ | $N_2H_4{\cdot}H_2O$ | 3–6 | 189 |
| | | $Ni(acac)_2$ | $H_2$ | 2–6 | 200 |
| | IRMOF-3 | $NaAuCl_4$ | — | 1.7–3.3 | 221 |
| | MIL-101 | $Pd(NO_3)_2$ | $H_2$ | 2.5 ± 0.5 | 85 |
| | | $Pd(NO_3)_2$ | $H_2$ | 2.6 ± 0.5 | 86 |
| | | $Pd(NO_3)_2$ | $H_2$ | 1.9 ± 0.7 | 89 |
| | | $H_2PtCl_6$ | $H_2$ | 5 ± 0.5 | 88 |
| | | $Pd(acac)_2$ | $H_2$ | 2.6–3.9 | 190 |
| | | $Pd(NO_3)_2$ | Microwave irradiation and $N_2H_4{\cdot}H_2O$ | Less than 3 | 95 |
| | | $Pd(NO_3)_2$ | $H_2$ | 2.6 ± 0.5 | 192 |
| | | $NiCl_2$ and $K_2PtCl_6$ | $NaBH_4$ | 1.8 ± 0.4 | 193 |
| | | $Pd(acac)_2$ | $H_2$ | 2–3 | 199 |
| | | $RuCl_3$ | $H_2$ | 4–5 | 202 |
| | | $H_2PdCl_4$ | $NaBH_4$ | 3.7 | 203 |
| | | $HAuCl_4$ | $H_2$ | 9.8 ± 3.4 | 228 |
| | | $Pd(NO_3)_2$ | $H_2$ | 2–3 | 247 |
| | | $AgNO_3$ | $NaBH_4$ | 1.4 ± 0.4 | 257 |
| | S-MIL-101 | $RhCl_3$ | $NaBH_4$ | 2.35 ± 0.9 | 206 |
| | MIL-101-$SO_3H$ | $Pd(acac)_2$ | $H_2$ | 3.0 ± 0.6 | 213 |
| | | $HAuCl_4$ and $AgNO_3$ | Dopamine | 2–10 | 208 |
| | MIL-101-$NH_2$ | $H_2PdCl_4$ | $NaBH_4$ | 2.49 | 90 |
| | | $PdCl_2(MeCN)_2$ | $NaBH_4$ | ~1 | 196 |
| | | $KAuCl_4$ | Triethylamine | 1.5–2.5 | 216 |
| | | $PdCl_2(MeCN)_2$ | $NaBH_4$ | 2–3 | 217 |
| | | $H_2PtCl_6$ | $H_2$ | 3.75 ± 0.5 | 266 |
| | Al-MIL-101-$NH_2$ | $H_2PdCl_4$ | $NaBH_4$ | 2.8–3.1 | 203 |
| | ED-MIL-101 | $PdCl_2$, $H_2PtCl_6$ and $HAuCl_4$ | $NaBH_4$ | 2–4 | 97 |
| | | $HAuCl_4$ and $H_2PdCl_4$ | $H_2$ | 2–8 | 98 |
| | Al-MIL-53 | $H_2PdCl_4$ | $NaBH_4$ | 4 | 203 |
| | Al-MIL-53-$NH_2$ | $H_2PdCl_4$ | $NaBH_4$ | 2.4 | 203 |
| | | $H_2PdCl_4$ | $NaBH_4$ | 3.12 | 218 |
| | | $H_2PdCl_4$ | $NaBH_4$ | 3.4 | 219 |
| | Al-MIL-100 | $H_2PdCl_4$ | $H_2$ | 1.8 ± 0.4 | 92 |
| | UiO-66 | $Pd(NO_3)_2$ | $H_2$ | Less than 5 | 91 |
| | | $Pd(OAc)_2$ | $H_2$ | Less than 1.2 | 262 |
| | UiO-66-$NH_2$ | $K_2PtCl_4$ | $H_2$ | 1.16 ± 0.16 | 99 |
| | | $AgNO_3$ and $PdCl_2$ | $NaBH_4$ | 5–9 | 210 |
| | | $H_2PdCl_4$ | $H_2$ | 1.5–2.5 | 214 |
| | | $Pd(OAc)_2$ | $H_2$ | Less than 1.2 | 262 |
| | UiO-66-OMe | $Pd(OAc)_2$ | $H_2$ | Less than 1.2 | 262 |
| | UiO-67 | $K_2PtCl_4$ | $NaBH_4$ | 4.5 | 207 |
| | UiO-68 | $Pd(NO_3)_2$ | $NaBH_4$ | Less than 2 | 198 |
| | La-BTC | $RuCl_3$ | $H_2$ | ~2 | 87 |
| | ZIF-8 | $PdCl_2$ | $NaBH_4$ | 2–3 | 93 |
| | | $HAuCl_4$ and $AgNO_3$ | $NaBH_4$ | 2–6 | 96 |
| | | $RhCl_3$ | $NaBH_4$ | — | 194 |
| | Zn(pip)(dpb) | $HAuCl_4$ | $NaBH_4$ | 1.85 ± 0.3 | 100 |
| | | $PdCl_2$ | $NaBH_4$ | 2.8 ± 0.3 | 101 |
| | $\{Ni(C_{10}H_{26}N_6)\}_3(bpdc)_3$ | $AgNO_3$ | $Ni^{II}$ macrocycle | ~3 | 103 |
| | [Ni(cyclam)]$_2$[BPTC] | $AgNO_3$ | $Ni^{II}$ macrocycle | 3.7 ± 0.4 | 104 |
| | | $NaAuCl_4$ | $Ni^{II}$ macrocycle | 2 | |
| | $[\{[Ni(cyclam)]_2(mtb)\}_n]$ | $Pd(NO_3)_2$ | $Ni^{II}$ macrocycle | ~2 | 105 |
| | $[Zn_3(ntb)_2(EtOH)_2]$ | $Pd(NO_3)_2$ | ntb | 3.0 ± 0.4 | 106 |
| | Rb-CD-MOF | $AgNO_3$ | $OH^-$ | 2.0 ± 0.4 | 107 |
| | | $HAuCl_4$ | $OH^-$ | 3–4 | |
| | Ti-MIL-125 | $HAuCl_4$ | Photoreduction | 6 | 108 |
| | | $H_2PdCl_4$ | | 3 | |
| | | $H_2PtCl_6$ | | 3 | |
| | Ti-MIL-125-$NH_2$ | $H_2PtCl_6$ | Photoreduction | — | 110 |
| | | $H_2PtCl_6$ | $H_2$ | — | 264 |
| | $Zr_6O_4(OH)_4(bpdc)_{5.94}(L_1)_{0.06}$ | $K_2PtCl_4$ | Photoreduction | 2–3 | 109 |
| | $Zr_6O_4(OH)_4(L_2)_6$ | $K_2PtCl_4$ | Photoreduction | 5–6 | |
| | Fe-MIL-100 | $HAuCl_4$ | Photoreduction | 15 | 111 |
| | | $H_2PtCl_6$ | | 2 | |
| | | $H_2PdCl_4$ | | 12 | |
| | BIF-20 | $AgNO_3$ | $BH(MeIM)_3^-$ | 3 | 112 |
| | Fe-MIL-88B-$NH_2$ | $Na_2PdCl_4$ | $NaBH(OAc)_3$ | 2 | 195 |
| | MIL-88B-$NH_2$ | $Na_2PdCl_4$ | $NaBH_4$ | 2–3 | 229 |

Table 1 (*continued*)

| Preparation method | MOF | Metal precursor | Reduction method | Particle size (nm) | Ref. |
|---|---|---|---|---|---|
| | $[Zn(Himdc)(bipy)_{0.5}]\cdot DMF$ | $PdCl_2$ | $NaBH_4$ | 1–2 | 220 |
| | Ni-MOF | $AgNO_3$ | Urotropine | 1 | 222 |
| | MIL-120 | $Ni(NO_3)_2$ | Thermal treatment | 5–20 | 224 |
| | Cu(II)-MOF | $Pd(NO_3)_2$ | $NaBH_4$ | 2 | 230 |
| | | $HAuCl_4$ | $NaBH_4$ | 2 | 268 |
| | Tm-MOF | $PdCl_2(CH_3CN)_2$ | $NaBH_4$ | — | 250 |
| | F15-NU-1000 | $Pd(acac)_2$ | $H_2$ | 2.5 | 263 |
| Double-solvent approach | MIL-101 | $H_2PtCl_6$ | $H_2$ | 1.2–3.0 | 113 |
| | | $HAuCl_4$, $NiCl_2$ | $NaBH_4$ | $1.8 \pm 0.2$ | 117 |
| | | $Pd(NO_3)_2$ | $NH_3BH_3$ | 1–3.5 | 114 |
| | | $K_2PdCl_4$ and $NiCl_2$ | $NaBH_4$ | — | 116 |
| | | $Pd(NO_3)_2$ and $AgNO_3$ | $H_2$ | 1.5 | 82 |
| | | $Pd(NO_3)_2$ and $CoCl_2$ | $NH_3BH_3$ | $\sim$2.5 | 118 |
| | | $H_2PtCl_6$ | $H_2$ | $\sim$2.5 | 191 |
| | | $H_2PdCl_4$ | $H_2$ | $1.8 \pm 0.2$ | 235 |
| | UiO-66-$NH_2$ | $Pd(NO_3)_2$ | Photoreduction | 1.2 | 115 |
| Chemical vapor deposition | MOF-5 | $(\eta^5\text{-}C_5H_5)Pd(\eta^3\text{-}C_3H_5)$ | $H_2$ | $1.4 \pm 0.1$ | 119 |
| | | $(\eta^5\text{-}C_5H_5)Cu(PMe_3)$ | $H_2$ | 3–4 | |
| | | $(CH_3)Au(PMe_3)$ | $H_2$ | 5–20 | |
| | | Ru(cod)(cot) | $H_2$ | 1.5–1.7 | 120 |
| | | CpCuL | Photoassisted thermolysis | 1–3 | 121 |
| | | Ru(cod)(cot) and Pt(cod)$Me_2$ | $H_2$ | 3.5 | 122 |
| | | $Pd(C_3H_5)(C_5H_5)$ | Photolysis | 2–5 | 215 |
| | MOF-177 | $Me_3PtCp'$ | $H_2$ | 2–5 | 124 |
| | | $CpPd(\eta^3\text{-}C_3H_5)$ | UV-light irradiation | $\sim$3 | 125 |
| | MIL-101 | $(\eta^3\text{-}C_3H_5)Pd(\eta^5\text{-}C_5H_5)$ | Thermal treatment | 1–3 | 126 |
| | | $(\eta^3\text{-}C_3H_5)Pd(\eta^5\text{-}C_5H_5)$ and $Ni(\eta^5\text{-}C_5H_5)_2$ | $H_2$ | $\sim$3.5 | 127 |
| | | $Pd(C_5H_5)(C_3H_5)$ | $H_2$ | 2–3.5 | 201 |
| | | Ru(cod)(cot) | $H_2$ | $4.2 \pm 1.2$ | 204 |
| | ZIF-8 | $Ni(cp)_2$ | $H_2$ | 2–3.4 | 128 |
| | | Ir(COD)(MeCp) | $H_2$ | $3.3 \pm 1.7$ | 255 |
| | MesMOF-1 | $(\eta^5\text{-}C_5H_5)Ni(\eta^3\text{-}C_5H_5)$ | $H_2$ | 1.4–1.9 | 129 |
| | SNU-90 | $MgCp_2$ | Thermal treatment | $60 \pm 18$ (length) $37 \pm 12$ (thickness) | 130 |
| Solid grinding | CPL-2 | $Me_2Au(acac)$ | $H_2$ | $2.2 \pm 0.3$ | 131 |
| | Al-MIL-53 | | | $1.6 \pm 1.0$ | 132 |
| | ZIF-8 | | | $3.4 \pm 1.4$ | 133 |
| | $Cd_2(L)(H_2O)\cdot 0.5H_2O$ | | | — | 134 |

by solution impregnation, in some cases, show a broad size distribution of MNPs when the process is poorly controlled.

Kaskel and coworkers incorporated Pd NPs into an MOF-5 ($[Zn_4O(BDC)_3]$, BDC = 1,4-benzenedicarboxylate) framework *via* the solution impregnation approach.[84] $Pd(acac)_2$ (acac = acetylacetonate) was employed as a precursor and dissolved in chloroform. The solution was slowly added to the activated MOF-5 dropwise under continuous stirring. Chloroform was slowly evaporated in an argon atmosphere and gave a pre-dried paste of $Pd(acac)_2$/MOF-5, which was completely dried under reduced pressure overnight at room temperature. The resulting slightly yellow powder was heated at 423 K or 473 K under vacuum for 4 h to produce Pd/MOF-5. $Pd(acac)_2$/MOF-5 heated in a $H_2$ flow at 423 K or 473 K for 1 h can also give rise to a Pd/MOF-5 composite. Similarly, a series of catalysts such as Pd/MIL-101 ($Cr_3F(H_2O)_2O(BDC)_3\cdot nH_2O$, $n \approx 25$), Pt/MIL-101, Pd/MIL-101-$NH_2$ ($Cr_3F(H_2O)_2O(BDC\text{-}NH_2)_3\cdot nH_2O$, BDC-$NH_2$ = 2-aminoterephthalate), Pd/UiO-66 ($Zr_6O_4(OH)_4(BDC)_6$), Pd/ZIF-8 ($Zn(MeIM)_2$, MeIM = 2-methylimidazole), Ru/La-BTC (La(1,3,5-BTC)$\cdot 6H_2O$), Pd@Al-MIL-100 ($Al_3O(OH)(H_2O)_2(BTC)_2\cdot nH_2O$, BTC = benzenetricarboxylate), and Au/MOF-545 ($Zr_6(H_2O)_8O_8(TCPP)_2$, TCPP = tetrakis(4-carboxyphenyl)porphyrin) can be synthesized.[85–94] MOFs are not only limited to monometallic NPs; bimetallic NPs stabilized by MOFs can also be obtained *via* a solution impregnation method.[95,96] Xu's group reported core–shell structured bimetallic NPs mainly on a zeolitic imidazolate framework, ZIF-8. The desolvated ZIF-8 was immersed in an aqueous solution containing $HAuCl_4$ and $AgNO_3$, with subsequent reduction by $NaBH_4$ and drying to yield Au@Ag core–shell NPs stabilized by ZIF-8.[96]

Enhancing the interaction between the metal precursors and cavities/channels of the MOF matrix would facilitate the introduction of the metal precursors. The creation of coordinatively unsaturated metal sites (CUSs) makes further functionalization possible (Fig. 1). For instance, the trimeric $Cr^{III}$ octahedral clusters in MIL-101 possess terminal water molecules. CUSs can be generated upon the removal of water molecules from the framework by vacuum treatment, providing strong interaction sites for ethylenediamine (ED) molecules. ED-grafted MIL-101

 

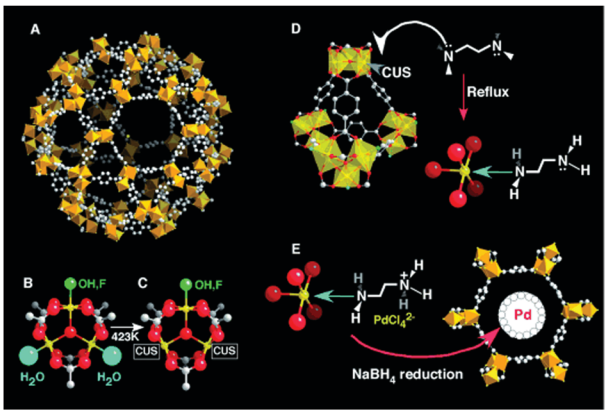


Fig. 1 Functionalization of unsaturated metal sites in MIL-101. (A) View of the mesoporous cage in MIL-101. (B and C) Evolution of coordinatively unsaturated sites (CUSs) from $Cr_3O$ cluster in mesoporous cage of MIL-101 upon activation at 423 K for 12 h. (D) Surface functionalization of the dehydrated MIL-101 through selective grafting of amine molecules onto CUS. (E) Selective encapsulation of Pd NPs into amine-grafted MIL-101. The Cr, C, and O atoms are shown in yellow, pale gray, and red, respectively. The $CrO_6$ octahedra are shaded in yellow. Reproduced from ref. 97 with permission from Wiley-VCH, copyright 2008.

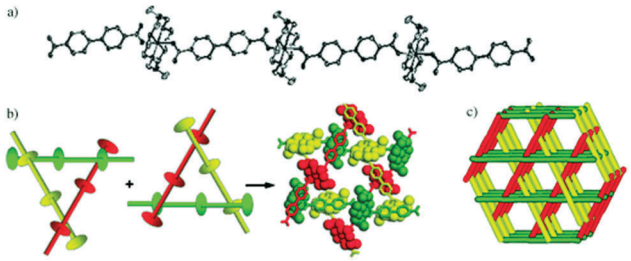


Fig. 2 (a) View of the 1D structure of the coordination polymer. (b) Double network of threefold braids where macrocycles fit into the grooves created by $bpdc^{2-}$ ligands. (c) View of the 1D channels generated by stacking of the linear chains. Reproduced from ref. 103 with permission from Wiley-VCH, copyright 2005.

can be used to encapsulate MNPs with the help of the interactions between positively charged surface ammonium groups and anionic metal salts ($[PdCl_4]^{2-}$, $[PtCl_6]^{2-}$, and $[AuCl_4]^-$), which were finally reduced by $NaBH_4$ to give MNPs with similar sizes of 2–4 nm.[97] Using a similar strategy, AuPd alloy NPs were stabilized by ED-grafted MIL-101.[98] Due to the interaction effect between amino groups and metal precursors, Guo *et al.* obtained small and monodisperse Pt NPs (1.16 ± 0.16 nm) in the cavities of UiO-66-$NH_2$ ($Zr_6O_4(OH)_4(BDC\text{-}NH_2)_6$), even at 10.7 wt% Pt loading.[99] In addition, the outstanding ability of alkyne groups to stabilize metal ions was demonstrated.[100,101] Gole *et al.* employed prefunctionalization of MOFs (Zn(pip)(dpb), pip = 5-(prop-2-yn-1-yloxy)isophthalate, dpb = 1,4-di(pyridin-4-yl)benzene) with terminal alkyne to uniformly stabilize $Au^{3+}$ ions in the MOF matrix and subsequently control the growth of Au NPs during the reduction process. An amazingly high loading amount (50 wt%) of Au NPs with a narrow size distribution throughout the MOF was achieved.[100]

Furthermore, Jiang and coworkers developed a seed-mediated approach to the general and mild synthesis of non-noble MNPs stabilized by MOFs.[102] The basic concept of such a seed-mediated approach to synthesizing non-noble MNPs under mild conditions is to take advantage of the difference in the reduction potentials of the noble and non-noble metal salts. Trace amounts (1/100–1/200, molar ratio of noble metal/non-noble metal) of noble and non-noble metal precursors were introduced into an $NH_3BH_3$ hydrolysis system containing a MOF. The noble metal precursors were quickly reduced to NPs in the MOF cavities, while non-noble metal precursors were subsequently reduced to small NPs stabilized by the MOF, due to the highly reducible intermediate M–H species.

Compared with the traditional method, Suh's group developed a special approach to the fabrication of MNPs by employing redox-active MOFs at a very early stage, leading to the generation of MNPs in a facile one-step process without using additional reducing agent.[103–105] A variety of $Ni^{II}$ macrocyclic complexes were employed as redox-active metal building blocks to construct MOFs (Fig. 2). The resultant redox-active MOFs were soaked in a solution of noble metal precursors such as $AgNO_3$, $Pd(NO_3)_2{\cdot}2H_2O$, and $NaAuCl_4{\cdot}2H_2O$. The metal ions diffused into the MOF cavities and became attached to the aromatic rings of multidentate organic ligands, and then the metal ions were reduced to MNPs with oxidation of the redox-active Ni-centers from $Ni^{2+}$ to $Ni^{3+}$, and the local coordination frameworks were maintained. A redox-active $Ni^{II}$ square-planar macrocyclic complex, $[Ni(C_{10}H_{26}N_6)](ClO_4)_2$, and $bpdc^{2-}$ (biphenyl-4,4′-dicarboxylate) ions were added to a water/pyridine mixture to construct a redox-active MOF, which was then immersed in a methanolic solution of $AgNO_3$ at ambient temperature for 10 min, leading to the formation of Ag NPs (~3 nm in diameter), which were loaded into the MOF.[103] Similar results have been reported by the same group, showing the successful synthesis of Au and Pd NPs with sizes of ~2 nm, respectively based on $NaAuCl_4{\cdot}2H_2O$ and $Pd(NO_3)_2$ precursors, in different redox-active Ni-MOFs with 2D or 3D structures, by using almost the same process.[104,105] In addition to the redox-active metal centers, they also prepared a porous MOF, $[Zn_3(ntb)_2(EtOH)_2]{\cdot}4H_2O$ (ntb = 4,4′,4″-nitrilotrisbenzoate), containing redox-active $ntb^{3-}$ organic building blocks. After the MOF was immersed in an acetonitrile solution of $Pd(NO_3)_2$ for 30 min, the $ntb^{3-}$ was oxidized to the amine radical along with the *in situ* generation of Pd NPs (3.0 ± 0.4 nm).[106]

Grzybowski's group successfully synthesized NPs/MOF with a core–shell architecture by reaction diffusion.[107] Two types of millimeter-sized MOFs, Rb-CD-MOF and Cs-CD-MOF (CD = cyclodextrin), were immersed in acetonitrile solutions of $AgNO_3$ and $HAuCl_4$, respectively. The $OH^-$ counterions homogenously distributed in the CD-MOF reduced the metal precursors to their respective MNPs. By coupling the diffusion of precursors with their reduction, Ag NPs with sizes of 2.0 ± 0.4 nm and Au NPs with sizes of 3–4 nm were produced inside the CD-MOFs. Unexpectedly, Ag NPs were deposited uniformly throughout the MOF, but these were mainly formed in the MOF center. The authors proposed that, by virtue of the reaction and diffusion occurring on similar time scales, multiple electrons were required for the reduction of $Au^{III}$, leading to the formation

of Au NPs as ''cores'' inside the MOF. The loading amount of MNPs can be adjusted by controlling the impregnation time or the concentration of the metal precursors. Moreover, core–shell NPs/CD-MOFs can also be synthesized through a combination of deposition sequences of Ag and Au: an Au core was firstly formed by impregnation of MOF with $HAuCl_4$ solution, washed with acetonitrile and then immersed in $AgNO_3$ solution to deposit Ag shell on the outside of the Au core. By gradually dissolving the MOF, the embedded NPs can be released.

Photodeposition is another alternative method for producing MNPs@MOF composites.[108–111] A series of MNP/Ti-MIL-125 ($Ti_8O_8(OH)_4(BDC)_6$) composites were successfully synthesized under light irradiation. Due to the reducing ability of $Ti^{3+}$, which was generated from optically induced electron trapping at $Ti^{4+}$ sites, noble metal precursors can be directly reduced without an additional reducing agent.[108]

In addition, Zhang *et al.* observed a boron imidazolate framework crystal, BIF-20 ($Zn_2(BH(MeIM)_3)_2(obb)$; obb = 4,4′-oxybis(benzoate)), which could directly produce small noble-metal NPs (Ag or Au) in its pores without the need for an external reducing agent or photochemical reactions, due to the reducing property of the B–H groups that decorate the internal pore surface.[112]

**2.1.2. Double-solvent approach.** Solution impregnation is a classical and effective method to yield MNP/MOF composites, but it is difficult to realize precise control of the loading position of MNPs relative to the host MOF. As mentioned above, some precursors deposit on the external surface of MOFs to form aggregated MNPs. To obtain MNPs exactly encapsulated inside MOF pores and prevent them from aggregating, a double-solvent approach (DSA) was developed to rationally introduce metal precursors into MOF pores, followed by reduction, to afford MNPs@MOFs.[82,113–118] Given the large cages with hydrophilic environments and high pore volumes in some MOFs, particularly MIL-101, the quantitative volume (no larger than the MOF pore volume) of the metal precursor aqueous solution, which is highly dispersed in a large volume of low-boiling-point organic solvent, can be completely incorporated into the MOF pores on the basis of capillary force and hydrophilic interactions during this process. The resultant metal precursors can be further reduced to generate tiny MNPs confined in MOFs.

Xu's group reported, for the first time, the DSA as an effective methodology for immobilizing MNPs completely inside the pores of MOFs without aggregation on the outer surface. They selected MIL-101 because of its high stability, high pore volume, large surface area, and two hydrophilic cavities with large diameters of *ca.* 2.9 and 3.4 nm; this is one of the most ideal MOFs for hosting MNPs based on the DSA. The desolvated MIL-101 was firstly dispersed in a hydrophobic solvent (hexane) through ultrasonication, then a hydrophilic solvent (water) containing $H_2PtCl_6$ with a volume equal to or less than the pore volume of MIL-101 was pumped into the hexane with dispersed MIL-101. The limited volume of the $H_2PtCl_6$ aqueous solution can be completely absorbed into the MIL-101 cavities by capillary force. The large hydrophilic internal pore surface plays a critical role in facilitating the impregnation process. The synthesized sample was treated in a flow of $H_2$/He at 473 K for 5 h to afford

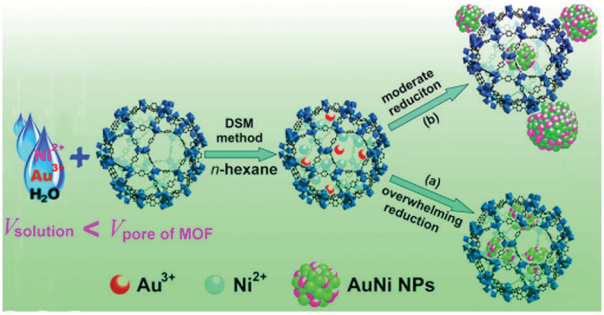


Fig. 3 Schematic representation of immobilization of AuNi NPs into MIL-101 matrix using the DSA combined with a liquid-phase concentration-controlled reduction strategy. Reproduced from ref. 117 with permission from the American Chemical Society, copyright 2013.

Pt NPs with an average size of 1.8 ± 0.2 nm that were well encapsulated in MIL-101.[113] In contrast to the traditional impregnation process, the DSA is very effective and almost no MNPs were deposited on the external surface of the MOF.

This technique is not limited to monometallic NPs; bimetallic AuNi alloy NPs were fabricated inside MIL-101 with the size and location of the AuNi NPs being well controlled by a liquid-phase concentration-controlled reduction strategy combined with the DSA (Fig. 3).[117] $HAuCl_4$ and $NiCl_2$ were initially introduced into the cavities of MIL-101 by using the DSA; when a high-concentration $NaBH_4$ solution (0.6 M) was added, an overwhelming reduction took place in the cavities of MIL-101, resulting in the formation of highly dispersed AuNi alloy NPs with an average size of 1.8 ± 0.2 nm, which were embedded in the pores of MIL-101. However, when a low-concentration $NaBH_4$ solution was used, the reduction of the precursor inside the pores was not completed, and some of the precursor redissolved and diffused out of the pores, resulting in the aggregation of MNPs on the outer surface of the MOF. Accordingly, 0.4 M and 0.2 M $NaBH_4$ solutions led to AuNi@MIL-101 with MNPs with sizes of 2.0–5.0 nm and over 5.0 nm, respectively. Subsequently, ultrafine PdAg alloy NPs (1.5 nm) were successfully obtained in the cavities of MIL-101 *via* the DSA, and these were possibly the smallest bimetallic NPs in the presence of surfactant protection, showing excellent monodispersity throughout the matrix of MIL-101.[82]

In addition to bimetallic alloy NPs, recently, for the first time, Jiang's group reported core–shell structured bimetallic NPs encapsulated into a MOF based on a DSA (Fig. 4).[118] The $Pd(NO_3)_2{\cdot}2H_2O$ and $CoCl_2{\cdot}6H_2O$ pre-incorporated in the pores of MIL-101 by the DSA were sequentially *in situ* reduced by $NH_3BH_3$ to yield ~2.5 nm Pd@Co core–shell NPs mostly embedded inside the MOF. In this study, Pd NPs were formed first and served as cores for the subsequent reduction to yield Co shell NPs. The principle of the formation of core–shell NPs is based on a suitable reducing agent ($NH_3BH_3$) and the difference in the reduction potentials of the two metal salt precursors ($E^{\circ}_{Pd^{2+}/Pd} = +0.915$ eV *vs.* SHE; $E^{\circ}_{Co^{2+}/Co} = -0.28$ eV *vs.* SHE, SHE = standard hydrogen electrode). $NH_3BH_3$ can only reduce $Pd^{2+}$ at first due to its high reduction potential, while

 

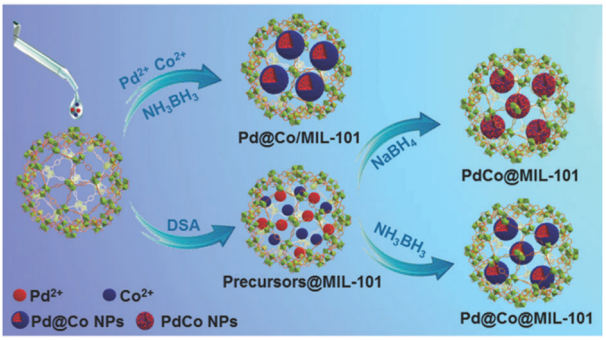


Fig. 4 Synthesis of Pd@Co@MIL-101, Pd@Co/MIL-101, and PdCo@MIL-101 catalysts with different procedures and reducing agents. Reproduced from ref. 118 with permission from Wiley-VCH, copyright 2015.

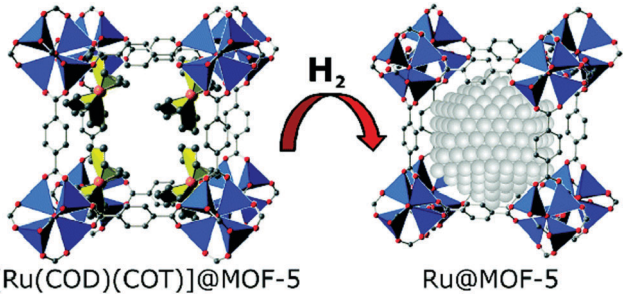


Fig. 5 The [Ru(cod)(cot)] precursors were incorporated in MOF-5 cages and subsequent hydrogenolysis of the adsorbed organometallic precursors gave Ru@MOF-5. Reproduced from ref. 120 with permission from the American Chemical Society, copyright 2008.

$Co^{2+}$ was reduced by the subsequently generated M–H species during $NH_3BH_3$ hydrolysis.

**2.1.3. Chemical vapor deposition.** Chemical vapor deposition (CVD) was adopted for the preparation of MNP/MOF composites in the very early stages, based on organometallic precursors that are highly volatile even at room temperature or are readily sublimed at elevated temperatures. In this synthetic system, a desolvated MOF and volatile metal precursor are usually placed in two separate glass vials in a Schlenk tube, and the tube is tightly sealed and kept under vacuum. The desolvated MOF is exposed to the vapor of the volatile metal precursor, and then the precursor will be diffused into the MOF pores at a suitable temperature depending on the vapor pressure of the metal precursor under a static vacuum. Thus, this method is a solvent-free process that allows the loading of a large amount of MNPs. The color of the MOF changes when it is infiltrated by the metal precursor. MNPs are then embedded in the MOF after being treated with thermal/chemical processes, UV irradiation, or reactive gases. Care and experience are required during the CVD process. Otherwise, the obtained MNPs may have a broad size distribution and be larger than the pore size of the MOFs.

Fischer's group first reported MNPs stabilized with MOFs using the CVD method.[119] MOF-5 was firstly employed as a host matrix to capture organometallic complexes such as $[(\eta^5\text{-}C_5H_5)Pd(\eta^3\text{-}C_3H_5)]$, $[(\eta^5\text{-}C_5H_5)Cu(PMe_3)]$, and $[(CH_3)Au(PMe_3)]$. Activated MOF-5 was exposed to the vapor of organometallic precursors in a static vacuum (1 Pa) at room temperature in a tightly sealed Schlenk tube. When the volatile metal precursors diffused into MOF-5, the original light-colored microcrystalline material turned dark. Finally, Pd/MOF-5, Cu/MOF-5, and Au/MOF-5 were formed by treating with a $H_2$ stream at hydrogenolysis temperatures. Similarly, Ru NPs with sizes in the range 1.5–1.7 nm, embedded in MOF-5, were successfully synthesized *via* this CVD process.[120] Desolvated MOF-5 powder and [Ru(cod)(cot)] (cod = 1,5-cyclooctadiene, cot = 1,3,5-cyclooctatriene) were placed in two separate glass vials in a Schlenk tube and kept at 303 K for 6 days in a static vacuum. The organometallic precursors were evenly distributed in MOF-5, and subsequent hydrogenolysis of the adsorbed organometallic precursors was operated under 3 bar $H_2$ at 423 K for 48 h (Fig. 5). The authors attempted to operate the hydrogenolysis step under mild conditions such as 298 K for 30 min, but Ru NPs could not be formed; $^{13}C$ MAS (magic angle spinning) NMR (nuclear magnetic resonance) spectra showed that some of the [Ru(cod)(cot)] was fragmented to 12-electron [(cod)Ru(0)] at room temperature, and this was trapped by ligands to form a new coordination bond with a benzene ring. The strong interaction between Ru(0) and the benzene ring prevented the generation of Ru NPs. MOF-5 can also be loaded with other metal precursors such as $[Fe(\eta^6\text{-toluene})(\eta^4\text{-}C_4H_6)]$, $[Sn((C_4H_9)_2)(OOC_2H_3)_2]$, and $[Pt(\eta^5\text{-}C_5H_5)(CH_3)_3]$ to produce the corresponding MOF-based composites.[121–123]

As MOF-5 is extremely unstable when exposed to moisture or even a trace of water, its practical applications are limited. Its window size (7.8 Å) might rule out organometallic precursors with larger dimensions. Thus, the highly porous MOF-177 ($Zn_4O(btb)_2$, btb = 1,3,5-benzenetribenzoate) would be a more favorable candidate, which features a larger pore opening size and cavities. A series of volatile precursors were loaded into activated MOF-177 through the CVD method. In Pt/MOF-177, Pt NPs with a size range of 2–5 nm were encapsulated in the MOF matrix *via* loading of $Me_3PtCp'$ (Cp′ = methylcyclopentadienyl) and subsequent reduction under 100 bar $H_2$ at 373 K for 24 h.[124] In the same year, the organometallic compounds $[Cp_2Fe]$ ($Cp = \eta^5\text{-}C_5H_5$), $[Zn(C_5Me_5)_2]_2$, $[Cu(OCHMeCH_2NMe_2)_2]$, [CpCuL] (L = $PMe_3$, CN*t*Bu), and $[CpPd(\eta^3\text{-}C_3H_5)]$ were loaded into MOF-177.[125] Remarkably, the loading amounts of $[Cp_2Fe]$ and $[CpPd(\eta^3\text{-}C_3H_5)]$ were extremely high with up to 11 and 10 molecules per MOF cavity, respectively. Pd@MOF-177 and Cu@MOF-177 composites with similar MNP sizes of ~3 nm can be obtained by treating with UV-light irradiation and thermal hydrogenolysis, respectively.

To avoid the water instability of MOFs for MNPs, a typical water-stable MOF, MIL-101, was selected as the host. Kempe's group synthesized Pd@MIL-101 by loading MIL-101 with a Pd precursor compound, $CpPd(\eta^3\text{-}C_3H_5)$.[126] In particular, the loading amount can be even higher than 50 wt% and the Pd NP sizes are closely related to the reduction temperature. The same group also fabricated $Pd_xNi_y$@MIL-101, in which the proportions of Pd and Ni can be accurately controlled through the simultaneous

loading of CpPd($\eta^3$-$C_3H_5$) and $Cp_2Ni$.[127] Furthermore, chemically robust ZIF-8 was also chosen as the host matrix to load Ni NPs (2–3.4 nm) *via* gas-phase infiltration of nickelocene ($NiCp_2$) followed by hydrogen reduction.[128] This CVD method was also used to prepare Ni NPs (1.4–1.9 nm) in a mesoporous MOF, MesMOF-1 ($Tb_{16}(TATB)_{16}$, TATB = triazine-1,3,5-tribenzoate), which has two mesocages with diameters of 3.9 and 4.7 nm.[129] After gas-phase loading of nickelocene into MesMOF-1, the composite material was treated with hydrogen gas at 368 K for 5 h. The amount of Ni NPs embedded in MesMOF-1 can be controlled by changing the loading time of the Ni precursor.

Suh and coworkers presented Mg nanocrystals (NCs) in SNU-90 ($Zn_4O(atb)_2{\cdot}22DMF{\cdot}9H_2O$, atb = aniline-2,4,6-tribenzoate) by a CVD process in combination with a simple thermal decomposition with no hydrogenolysis step.[130] They loaded the vapor of bis-cyclopentadienyl magnesium ($MgCp_2$) into SNU-90 at 353 K for 1 day. The obtained $MgCp_2$@SNU-90 was thermally decomposed at 473 K under an argon atmosphere followed by evacuation, resulting in Mg NCs embedded in guest-free SNU-90′ ($Zn_4O(atb)_2$). The loading amount of Mg NCs in the SNU-90′ was adjusted by controlling the length of the deposition time and the pre-vacuum state of the reaction bottle. The hexagonal-disk-shaped Mg NCs with a diagonal length of 60 ± 18 nm and a thickness of 37 ± 12 nm were well covered with MOFs. The MOF structure was maintained after the formation of Mg NCs, which were not oxidized to MgO even after the sample was exposed to air for 2 days.

**2.1.4. Solid grinding.** Solid grinding can also induce volatile organometallic precursors to form activated MOFs, where the solid-state materials must be adequately mixed. During grinding, the sublimated vapor of the organometallic precursors diffuses rapidly into the MOF cavities. Subsequently, the organometallic precursor embedded in the MOFs is treated with $H_2$ gas at appropriate temperatures, leading to MNP/MOF composites. A significant advantage of solid grinding lies in its easy operation, and waste solvent can be avoided. Another advantage is the complete loading of all introduced precursors, so their loading amounts can be easily controlled. A disadvantage is that the metal precursor must be volatile and is usually expensive. The few reports on solid grinding are so far limited to Au/MOF composites.[131–134]

Haruta's group firstly demonstrated effective loading of Au NPs into various types of MOFs, including Al-MIL-53 ($[Al(OH)(BDC)]_n$), MOF-5, CPL-1 ($[Cu_2(pzdc)_2(pyz)]_n$, pzdc = pyrazine-2,3-dicarboxylate, pyz = pyrazine), CPL-2 ($[Cu_2(pzdc)_2(bpy)]_n$, bpy = 4,4′-bipyridine), and HKUST-1 ($Cu_3(BTC)_2$).[131,132] Dimethyl Au(III) acetylacetonate ($Me_2Au(acac)$), a slightly volatile complex with a vapor pressure of 1.1 Pa at room temperature, as the Au precursor was mixed with the solvent-free MOFs and ground in an agate mortar in air for 20 min at room temperature. The mixture was then treated in a flow of 10 vol% $H_2$ in $N_2$ at 393 K for 2 h to yield Au/MOF composites (Fig. 6). The Au NPs obtained with Au/CPL-2 were small and had a nearly uniform size with a mean diameter of 2.2 ± 0.3 nm. In comparison, the CVD method yielded larger Au NPs with a particle size of 3.1 ± 1.9 nm through the thermal hydrogenolysis of $Me_2Au(acac)$. The sublimation of $Me_2Au(acac)$ and diffusion into the MOF cavities takes place rapidly, while CVD requires more time to produce $Me_2Au(acac)$/MOFs. In addition, the size of the Au NPs was found to strongly depend on the properties of the MOFs, including structures, cavity sizes, and surface nature. Among the investigated MOFs, Al-MIL-53 is the best candidate to confine Au NPs with a mean diameter of 1.5 nm and a standard deviation of 0.7 nm. These results indicated that solid grinding was a simple and effective way to synthesize NP/MOF composites without solvent or a washing procedure.

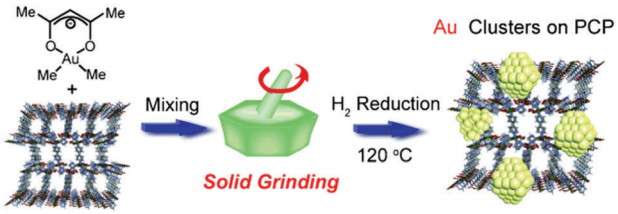


Fig. 6 Synthesis of Au/CPL-2 composite *via* solid grinding of CPL-2 with $Me_2Au(acac)$ followed by $H_2$ reduction. Reproduced from ref. 131 with permission from Wiley-VCH, copyright 2008.

With ZIF-8 as a host material, Au NPs were also formed based on the solid grinding method.[133] Pretreated ZIF-8 and desired quantitative $Me_2Au(acac)$ (0.5, 1.0, 2.0, and 5.0 wt% Au) were ground uniformly in an agate mortar in air for 35 min at room temperature, followed by treating in a stream of 10 vol% $H_2$ in He at 503 K for 2.5 h. The 1.0 and 5.0 wt% Au@ZIF-8 showed Au NP sizes of 3.4 ± 1.4 and 4.2 ± 2.6 nm, respectively. To deliberately encapsulate Au NPs inside MOF pores, a 3D porous Cd-MOF ($Cd_2(L)(H_2O){\cdot}0.5H_2O$, L = 4,4′-(hexafluoroisopropylidene)diphthalate) with hydrophobic fluorinated channels (7.8 Å in size) was synthesized and employed as the host (Fig. 7).[134] Desolvated Cd-MOF and 1 wt% $Me_2Au(acac)$ were ground for about 30 min at room temperature, followed by treating in a flow of 10 vol% $H_2$ in He at 443 K for 2 h to obtain Au NPs embedded in Cd-MOF. Unexpectedly, although the Au clusters were not observable by microstructural observation, the X-ray absorption fine structure (XAFS) data analyses unambiguously demonstrate the presence of Au clusters with an average atom number of 2.5. It is assumed that the $-CF_3$ groups grafted on the walls of the hydrophobic channels are responsible for the formation of the ultrafine $Au_2$ and $Au_3$ clusters inside the MOF.

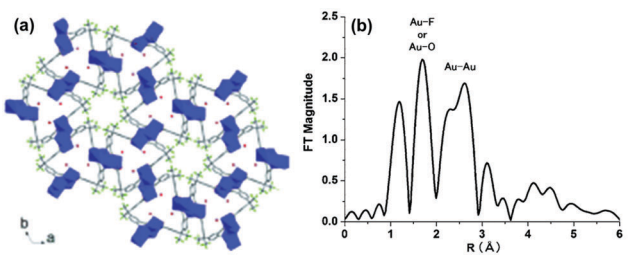


Fig. 7 (a) View of the 3D network of $Cd_2(L)(H_2O){\cdot}0.5H_2O$. (b) Au $L_{III}$-edge FT-EXAFS spectrum for Au/$Cd_2(L)(H_2O){\cdot}0.5H_2O$. Reproduced from ref. 134 with permission from Wiley-VCH, copyright 2011.

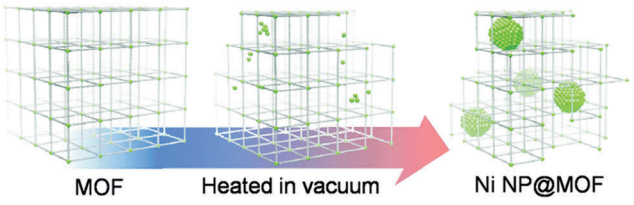


Fig. 8 Schematic synthesis of Ni@MOF *via* partial thermal decomposition of Ni-MOF-74. Reproduced from ref. 135 with permission from The Royal Society of Chemistry, copyright 2015.

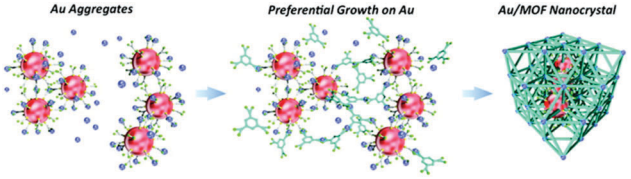


Fig. 9 Schematic representation of preferential self-assembly of HKUST-1 on aggregates of Au NPs. Reproduced from ref. 138 with permission from the American Chemical Society, copyright 2011.

**2.1.5. Thermal decomposition.** Thermal decomposition is a relatively new method of synthesizing MNPs@MOF materials. A significant advantage of this method is its extreme simplicity as no additional metal precursors are introduced. MNPs are generated during the partial thermal decomposition of MOFs and it is crucial to choose an appropriate temperature. If the temperature is too high, the MOF structures completely collapse, while a very low temperature cannot generate MNPs. The successful reports based on thermal decomposition are thus far limited to HKUST-1 and Ni-MOF-74 ($Ni_2(dobdc)(H_2O)_2{\cdot}8H_2O$, dobdc = 2,5-dihydroxyterephthalate).[135,136]

Mukoyoshi *et al.* successfully synthesized a Ni/Ni-MOF-74 composite *via* thermal decomposition by simply heating Ni-MOF-74 under vacuum (Fig. 8).[135] Powder X-ray diffraction (XRD) patterns showed that Ni-MOF-74 heated at 573 K for 12 h yielded an identical diffraction pattern to Ni-MOF-74; when the temperature was increased to 623 K for 12 h, broad peaks corresponding to a face-centered-cubic (fcc) Ni lattice appeared along with the Ni-MOF-74 pattern. A higher temperature heat treatment at 673 K for 12 h caused complete elimination of the initial Ni-MOF-74 diffraction pattern, and only an fcc-Ni pattern was observed.

## 2.2. Introducing MNPs for subsequent MOF growth

Introducing preformed MNPs as seeds or nucleation centers into MOF starting materials is a rational strategy to induce subsequent MOF growth/assembly around MNPs, giving MNPs@MOF composites. This strategy is also known as "bottle-around-ship", for which the prerequisite is a "binder" on the surface of the MNPs to anchor the heterogenous growth of MOF and avoid homogeneous MOF nucleation. Two significant advantages of this strategy are: (1) the size, shape, and composition of MNPs in the composite can be precontrolled; (2) the formation of core–shell structured MNPs@MOF is reasonably probable. Unfortunately, the introduction of MNPs into the systems sometimes causes difficulties with subsequent growth of the MOF. That is, foreign MNPs disturb the MOF formation. Therefore, not all MOFs are suitable for this synthetic approach and current reports are mostly based on ZIF-8 and a UiO series of "star" MOFs. In addition, the binder (for example, PVP) between MNPs and MOFs is difficult to completely wash away and this might be unfavorable with respect to the accessibility of the active sites.

Sugikawa *et al.* demonstrated the encapsulation of Au nanorods (NRs) inside a porous MOF ($Zn_4O(bpdc)_3$) by heating an *N*,*N*-diethylformamide (DEF) solution containing zinc nitrate hexahydrate, bpdc, and 11-mercaptoundecanoic acid (MUA) modified Au NRs at 353 K for 12 h in an oil bath.[137] The smooth surface and the purple color of the crystals, plus microstructural observation, demonstrated that Au NRs were incorporated inside the MOF. Based on a similar approach, Tsuruoka *et al.* prepared Au NP/MOF composites by the self-assembly of a MOF around MUA functionalized Au NPs (Fig. 9).[138] The bifunctionality of MUA is the key to its success: its terminal thio groups anchor to the Au NPs while the terminal carboxylic acid groups connect with metal ions for MOF growth. Therefore, HKUST-1 consisting of $Cu^{2+}$ ions and benzene-1,3,5-tricarboxylate preferentially grew on Au NPs, resulting in the formation of an Au NP/HKUST-1 composite. Moreover, cyano groups can also be used as binders between NPs and MOFs to obtain a single-layer Au@Prussian blue analogue (PBA) and double-layer Au@PBA@PBA core–shell nanostructure through the growth of a cyano-bridged coordination network on the gold surface.[139]

Lu *et al.* reported an elegant strategy allowing a variety of MNPs to be encapsulated into ZIF-8 in a well-controlled manner.[140] By surface modification with surfactant PVP, MNPs with various sizes, shapes, and compositions can be well dispersed inside the ZIF-8 matrix. The spatial distribution of embedded PVP-capped MNPs within ZIF-8 crystals can be controlled by an addition sequence (that is, addition at the beginning or after a certain time during the ZIF-8 synthesis). One or two types of MNPs can be controlled in the central areas or off the central areas of ZIF-8 particles (Fig. 10). The strategy of introducing MNPs for subsequent ZIF-8 growth was demonstrated to be very successful based on a variety of PVP-capped particles, such as Au, Pt, Pd, Ag NCs, polystyrene spheres, $Fe_3O_4$, CdTe, CdSe, β-FeOOH nanorods, $NaYF_4$ rods, and $NaYF_4$ NPs.[140–142] This method is limited to ZIFs composed with N-donor ligands; it was reported that MNPs can be encapsulated with good dispersity inside MOF particles constructed from carboxylate linkers,[143–145] which are the largest branch of the MOF family. UiO-66 as a "star" MOF was chosen because of its high surface area, intersecting 3D structure, and high stability. In a typical process, pre-synthesized Pt NPs were added to a DMF solution containing $ZrCl_4$, BDC, and acetic acid, and then the homogeneous mixture was heated at 393 K for 24 h without stirring, resulting in octahedral crystals of Pt/UiO-66. Furthermore, the encapsulation strategy is suitable for various solvents, including water, DMF, methanol, and benzyl alcohol, and it is applicable to other MOFs such as UiO-66-$NH_2$ and Fe-MIL-53-$NH_2$ ($[Fe(OH)(BDC\text{-}NH_2)]_n$).

Tang and coworkers synthesized a core–shell catalyst, Pd@IRMOF-3 ($Zn_4O(BDC\text{-}NH_2)_3$) consisting of a Pd core and

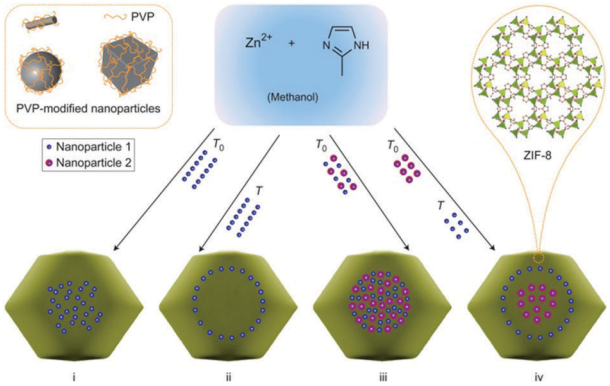


Fig. 10 Schematic illustration showing the controlled encapsulation of NPs in ZIF-8 crystals. Through surface modification with surfactant PVP, NPs of various sizes, shapes, and compositions can be encapsulated with a controlled spatial distribution into ZIF-8 crystals. Reproduced from ref. 140 with permission from Nature Publishing Group, copyright 2012.

MOF (IRMOF-3) shell, by a strategy of introducing MNPs for subsequent MOF growth.[146] The precursors $Zn(NO_3)_2$ and 2-amino terephthalic acid for synthesizing IRMOF-3 were added to a solvent containing DMF, ethanol, and PVP, followed by addition of pre-synthesized Pd NPs and subsequent solvothermal treatment. A typical core–shell structure was successfully formed, in which the monodisperse spherical Pd NPs (~35 nm in diameter) were coated with a uniform IRMOF-3 shell (~145 nm in thickness). Similarly, core–shell Ag@ZIF-8 nanowires (NWs) were also reported by the same group using a similar method.[147] The pre-synthesized Ag NWs were directly mixed with ZIF-8 precursors in methanol with stirring at 288 K for 3 h. Subsequently, the mixed solution was held at room temperature without stirring for 12 h. A shell of ZIF-8 was generated along the surface of the Ag NWs.

In a recent study, Jiang and coworkers rationally coated a representative MOF, ZIF-8, on PVP-capped Pd nanocubes to obtain Pd nanocubes@ZIF-8 with a core–shell structure.[81] The Pd nanocubes have a well-defined structure with a size of $17 \pm 3$ nm and are enclosed by {100} facets. The thickness of the ZIF-8 shell can be controlled by simply changing the reaction time, and an approximately 130 nm thick ZIF-8 shell can be obtained by growth at 277 K for 60 minutes. Subsequently, Zeng and coworkers reported the incorporation of Pt nanocubes and Au nanocages within the nanostructures of ZIF-8 by a similar process.[148] In a typical synthesis of Au&Pt@ZIF-8, a methanolic solution of zinc nitrate, 2-methylimidazole, Pt nanocubes, and Au nanocages were initially mixed, and then the system was kept at room temperature for 24 h without stirring. The Pt nanocubes and Au nanocages were well embedded in the rhombic dodecahedral ZIF-8 crystals. Replacing ZIF-8 by UiO-66 structured MOFs, Jiang and coworkers adopted a similar approach to disperse Pt NPs with a size of approximately 3 nm into the starting material, UiO-66-$NH_2$, to afford Pt@UiO-66-$NH_2$.[149] The Pt NPs did not aggregate and their sizes were maintained at around 3 nm in the obtained composites. Moreover, an Au@UiO-66-$NH_2$ composite was also formed by encapsulation of pre-synthesized Au NPs in a subsequently grown MOF.[150] A typical process involved sequentially adding $ZrCl_4$, acetic acid, and PVP capped-Au NPs with a uniform size (~15 nm) into a solution of DMF containing BDC-$NH_2$, and then the resulting mixture was bubbled with argon before being heated at 393 K for 24 h. It was noteworthy that if the oxygen was not removed from the synthetic system by argon bubbling, or acetic acid was not introduced into the reaction mixture, no Au@UiO-66-$NH_2$ was formed. This might be because Au NPs are readily oxidized to $Au^+$ and/or $Au^{3+}$ by oxygen with the assistance of $Cl^-$ ions. Similarly, Somorjai, Yaghi and coworkers also observed the dissolution of MNPs during the synthesis of UiO-66.[151] The pre-synthesized Cu NCs were not stable and dissolved during the subsequent attempted growth of UiO-66, even when oxygen was excluded from the solution. They found that the choice of zirconium precursors dramatically affected the encapsulation process. Both typical zirconium precursors ($ZrOCl_2 \cdot 8H_2O$ and $ZrCl_4$) for the synthesis of UiO-66 led to the dissolution of Cu NCs. Using $Zr(OPr^n)_4$ instead of the above precursors successfully solved the issue and produced a Cu/UiO-66 composite with a single Cu core inside each UiO-66 particle. Most recently, Yaghi, Yang, and coworkers coated a zirconium MOF that was covalently attached with a $CO_2$-to-CO conversion photocatalyst, $Re(CO)_3$(BPYDC)Cl (BPYDC = 2,2′-bipyridine-5,5′-dicarboxylate), onto PVP-capped Ag nanocubes. The Ag nanocubes with a size of 98 nm were well encapsulated with MOFs and the thickness of the MOF shell is controllable under synthetic conditions.[152]

Ke *et al.* synthesized a core–shell MNPs@MOF composite with a controllable MOF shell thickness by using a stepwise layer-by-layer (LBL) method.[153] The Au@Fe-MIL-100 ($Fe_3O(OH)$-$(H_2O)_2(BTC)_2 \cdot nH_2O$) composite was formed by repeated cycles of dispersing mercaptoacetic acid (MAA)-functionalized Au NPs into ethanol solutions of $FeCl_3$ and $H_3BTC$ separately at 343 K. The shell thickness of Fe-MIL-100 can be rationally controlled by changing the number of assembly cycles. Following a similar strategy, core–shell structured Au–$Fe_3O_4$@Fe-MIL-100 NPs can also be formed by an even easier synthesis with efficient magnetic separation due to the superparamagnetic component of $Fe_3O_4$.[154]

In addition to the common ''binder agents'', PVP, MUA, and MAA, polydopamine (PDA) was recognized as another excellent binder on the surface of MNPs. Duan and coworkers reported a versatile strategy using multifunctional PDA to construct well-defined core–shell MNPs@MOF composites.[155] The ability of PDA to form a robust conformal coating on substrates and to direct the heterogeneous nucleation and growth of MOFs makes it possible to fabricate a broad range of NP/MOF hybrid materials. Moreover, the unique redox activity of PDA gives it the additional ability to form functional nanohybrids between the core and shell *via* localized reduction. In particular, composites with Au NPs sandwiched between the magnetic core and MOF shell *via* localized reduction with PDA can rationally integrate the magnetic recyclability of the core and molecular size selectivity of the shell. Interestingly, Tsung's group successfully utilized an ionic surfactant, cetyltrimethylammonium bromide (CTAB), to control interfaces between Pd NCs and ZIF-8 in a core–shell Pd@ZIF-8 composite.[156] In the composite, Pd NCs are individually encased in ZIF-8 NCs. The CTAB layer can

 

bridge the interaction between Pd NCs and ZIF-8 with its hydrophobic tails, as well as stabilizing the {100} facets of Pd NCs and ZIF-8. At first, small ZIF-8 nuclei enclosed by low surface energy {100} facets formed in the solution, then a single ZIF-8 nucleus attached to Pd NCs with {100} facets *via* bridging of the CTAB layer and generated a ZIF-8 {100} to metal {100} interface. The authors speculate that this one-core-to-one-nucleus attachment is responsible for the final one-in-one single-crystalline structure. In addition, Zheng *et al.* demonstrated a general strategy of encapsulating single metal NPs capped with ammonium surfactant ($CTA^+$) into ZIF-8, in which MNPs with arbitrary morphologies can be readily applied.[157]

Wang *et al.* successfully incorporated surfactant-free highly dispersed Pt NPs within ZIF-8.[158] The 2-methylimidazole not only acted as an organic linker to construct ZIF-8 but also served as an effective stabilizing agent for small Pt NPs. Furthermore, the synthesis operated at room temperature to obtain a Pt@ZIF-8 composite with a uniform distribution of Pt NPs with a size of $\sim$2.0 nm in a ZIF-8 matrix.

Khaletskaya *et al.* reported a well-defined single Au NR confined in each particle of an Al-based MOF ($[Al(OH)(1,4\text{-ndc})]_n$, 1,4-ndc = naphthalenedicarboxylate).[159] To ensure precise control of the MOF growth around a single Au NR, the Au NRs were first coated with an amorphous alumina layer. Then, the $Al_2O_3$-capped Au NRs behaved as reactive seeds and the localized aluminum source, *i.e.*, the coated amorphous alumina, was dissolved during microwave treatment in the presence of 1,4-ndc, promoting the nucleation of MOF on the surface of the Au NRs. Recently, Zhao *et al.* achieved Ag@MOF mesoscopic constructs by atomic layer deposition of $Al_2O_3$ onto Ag NCs, and the addition of a tetratopic porphyrinic linker ($H_4TCPP$) to react with $Al_2O_3$ led to the MOF $[Al_2(OH)_2TCPP]$ enclosing the Ag NCs. The interface between Ag and the MOF was pristine and the MOF was oriented on the Ag NCs. The achieved $Al_2O_3$ thickness can be precisely controlled from 0.1 to 3 nm, and the MOF thickness ranged from 10 to 50 nm.[160]

Notably, MNPs can also act as sacrificial templates for constructing MOFs without an additional coating of metal. Li, Wu, and coworkers innovatively fabricated a Pt–Ni frame within MOFs (Fig. 11).[161] They pre-synthesized Ni-rich PtNi alloy NCs, then used organic linkers ($H_4$dobdc, 2,5-dihydroxyterephthalic acid) to capture the dissociated $Ni^{2+}$ ion during the dealloying process to *in situ* grow a shell of Ni-MOF-74 on the surface of the Pt–Ni alloy, leading to a unique Pt–Ni frame@Ni-MOF-74 composite. Upon treatment of the obtained composite with acetic acid, the coating MOF can be removed by preventing coordination between carboxylic oxygen atoms and $Ni^{2+}$, leaving a bare Pt–Ni frame with a hollow interior and the interconnecting edges in space, which is significantly different from the original PtNi alloy. Kuang's group successfully synthesized a Rh–Ni@Ni-MOF-74 heterostructure *via* a similar method. The encapsulation state and thickness of the MOF shell were effectively tuned by changing the Ni content in the templated Rh–Ni-alloyed nanoflowers.[162] Moreover, Cu@Cu-MOF-74 ($Cu_2$(dobdc)$(H_2O)_2\cdot 8H_2O$) was also constructed *via* partial conversion of naked Cu NCs into Cu-MOF-74 in the presence of $H_4$dobdc in a solvent mixture of DMF and EtOH.[163] The organic ligand ($H_4$dobdc) served as a framework strut of MOF and its deprotonation was attributed to the oxidative etching of Cu NCs. There were two main processes involved in the formation of the Cu@Cu-MOF-74 composite: oxidative etching of the Cu NCs (dissolution reaction) and heterogeneous nucleation of Cu-MOF-74 (precipitation reaction). The authors mentioned that the Cu@Cu-MOF-74 hybrid with a uniform morphology and a homogeneous distribution of embedded Cu NCs could only be formed under ideal synthetic conditions (EtOH/DMF volume ratio of 1, ligand-to-Cu molar ratio of 2, reaction temperature of 333 K, and reaction time of 40 min).

Sindoro and Granick observed that core–shell MNPs@ZIF-8 composites can evolve to yolk–shell nanostructures along with ZIF-8 recrystallization. Voids between core and shell were formed due to shell polycrystallinity. It was proposed that the shell domains were initiated at multiple nucleation points and had a similar growth rate. This procedure generates stress when the crystalline domains push against each other. This stress can be released by outward growth away from the core.[164] Furthermore, yolk–shell nanostructures can be achieved by introducing MNPs for subsequent MOF growth, involving $Cu_2O$ as an intermediate and void creator, which opens a new avenue to the construction of special core@void@shell structures. Tsung and coworkers coated pre-synthesized MNPs with a $Cu_2O$ layer as a sacrificial template to grow an outer shell on polycrystalline ZIF-8 (Fig. 12).[165] The clean $Cu_2O$ surface assisted in the formation of the ZIF-8 shell and was simultaneously etched off by the protons generated during the formation of ZIF-8. The trace amount of $Cu_2O$ residue can be removed by treating with a solution of 3% $NH_4OH$ in methanol. Through this strategy, a series of MNPs@ZIF-8 yolk–shell composites were constructed. The size and morphology of the Pd NCs were well preserved during coating of the ZIF-8 shell. Chen's group developed a simple strategy to fabricate Au-HKUST-1 composite nanocapsules consisting of HKUST-1 shells and embedded Au NPs. The novel synthesis procedure involves the formation of Au NPs on the surface of $Cu_2O$, partially converting $Cu_2O$ to HKUST-1 shell *via* coordination replication, and removing the residual $Cu_2O$ by acid etching.[166] Moreover, Au@HKUST-1

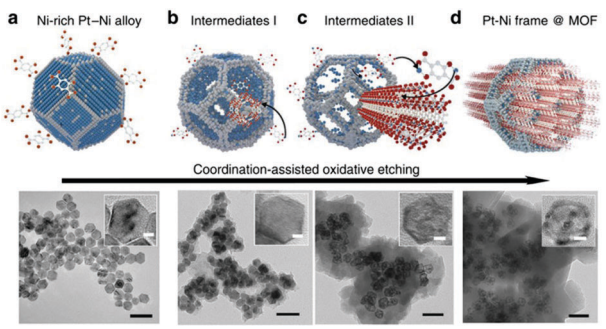


Fig. 11 (a) Initial solid Pt–Ni polyhedron. (b) PtNi frame@MOF intermediates I. (c) PtNi frame@MOF intermediates II. (d) Final PtNi frame@MOF. The scale bars: 50 nm; insets: the magnified TEM image with scale bars of 5 nm. Reproduced from ref. 161 with permission from Nature Publishing Group, copyright 2015.

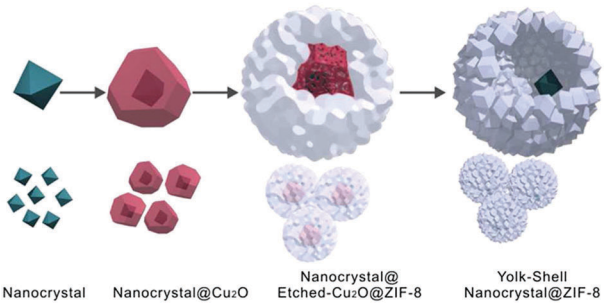


Fig. 12 Schematic growth procedure for the nanocrystal@ZIF-8 yolk–shell nanostructure. Reproduced from ref. 165 with permission from the American Chemical Society, copyright 2012.

ball-in-cage heterostructures were synthesized *via* a similar method. The $Cu_2O$@HKUST-1 core–shell heterostructure was synthesized by firstly soaking $Cu_2O$ NPs in $H_3BTC$ solution with subsequent $HAuCl_4$ impregnation, resulting in an Au@HKUST-1 ball-in-cage heterostructure. Due to the porosity of HKUST-1 and the reducibility of $Cu_2O$, $HAuCl_4$ could pass through the HKUST-1 shell and be reduced by the $Cu_2O$ core, providing Au NPs. Whether the $Cu_2O$ core remained or disappeared after the formation of Au NPs could be determined by controlling the concentration of Au precursors.[167]

Polystyrene (PS) and $SiO_2$ spheres are not only limited to $Cu_2O$ but can also act as templates to create hollow spaces in similar composites. For example, surfactant-free Pd NPs in hollow ZIF-8 nanospheres were obtained with the help of a PS template. First, Pd NPs were loaded onto carboxylate-terminated polystyrene (CPS) spheres through an *in situ* reduction with $Sn^{II}$ ions. ZIF-8 was then grown on the surface of CPS to give a CPS/Pd@ZIF-8 core–shell nanostructure. The CPS cores were finally removed with DMF to afford Pd@ZIF-8 hollow nanospheres.[168] Recently, a yolk–shell nanostructure (Au@ZIF-8) was reported *via* a sacrificial $SiO_2$ template strategy (Fig. 13). After $SiO_2$ removal, macropores in the ZIF-8 shell were created with Au NPs inside.[169]

Yang *et al.* developed a facile emulsion-based interfacial reaction method to synthesize yolk–shell Pd@ZIF-8 composites.[170] A water-in-oil nanoemulsion can be prepared using PVP as stabilizer and 1-octanol as the oil phase. Zinc ions in the aqueous phase coordinate with 2-methylimidazole in 1-octanol at the spherical interfaces of emulsion droplets, forming ZIF-8 NCs, which further grow to form nanospheres at room temperature. Controlling the concentration of 2-methylimidazole and the reaction time can lead to the formation of hollow ZIF-8 nanospheres with different shell thicknesses. Functional MNPs, such as Pd nanocubes dispersed in the liquid phase, can be encapsulated during the emulsification process.


Fig. 13 Schematic illustration showing the synthesis of Au@ZIF-8 nanoreactor. Reproduced from ref. 169 with permission from Wiley-VCH, copyright 2016.

### 2.3. Stepwise synthesis of MNPs/MOFs and MOF/MNPs/MOFs

For both general approaches discussed above, *i.e.*, pre-synthesis of MOF or preformation of MNPs followed by subsequent growth of the other component, the aim is to obtain MNPs confined inside MOF particles. To particular ends, we sometimes obtained MNPs exclusively on the external surface of the MOF. This can be achieved by preformation of both MOFs and MNPs, which are mixed and vigorously stirred or ultrasonicated to assemble them together based on physical adsorption and/or electrostatic interaction, thus giving MNPs/MOFs. An AuPd/MIL-101 composite was synthesized *via* direct assembly, in which AuPd NPs were initially prepared by a sol–gel method, and then the activated MIL-101 was added to the colloidal solution and stirred for 6 h. The sample was washed twice with water and dried under vacuum at 373 K for 2 h, then subsequently heated at 573 K in $H_2$ for 2 h.[171] Recently, a Pt/UiO-66-$NH_2$ composite was successfully constructed by a similar method. The as-synthesized UiO-66-$NH_2$ was immersed in a colloidal suspension of Pt NPs and sonicated for 10 h at room temperature. The gray precipitates were separated by centrifugation and washed with ethanol four times before drying in an oven under vacuum at 323 K overnight; this gave Pt/UiO-66-$NH_2$ with Pt NPs that had sizes of 3 nm both before and after assembly. It is worth noting that, as the electrostatic interaction between the two components is weak, the self-assembled MNP/MOF composites produced by this strategy are usually not very stable during catalytic recycling.[149]

A stepwise assembly strategy was recently further developed to afford stable MOF/MNP/MOF composites.[172,173] The synthesis of a three-layered MOF/MNPs/MOF takes at least three steps and seems complicated, but the composites possess special advantages: the MOF core not only acts as a support for the MNPs located in the middle-layer but also induces the subsequent growth of the MOF outer shell (usually, the crystalline lattice between the inner and outer MOFs is well matched); the MOF shell covers the middle-layer MNPs for better stability of the composite and determines the size selectivity of the catalysis. For core–shell structured MNP/MOF catalysts, while the thickness control of the MOF shell poses a significant challenge, it is crucial for the reaction efficiency, as the thick MOF shell significantly slows down the transport of substrates/products. The current design endows the resultant core–shell structured MOF/MNP/MOF catalyst with especially high selectivity (excluding large-size substrates/products with MOF outer shell) and high reaction efficiency (ease of maintaining a thin shell).

In a very recent study, Zhao *et al.* systematically fabricated a series of sandwich-like structures of MOF/MNPs/MOFs by such a step-by-step synthetic strategy (Fig. 14).[172] The pre-synthesized NPs can be easily assembled on the surface of the MOF core by physical adsorption and/or electrostatic interaction under vigorous stirring or ultrasonication, as indicated above and also in other reports.[149,171] To guarantee a perfect lattice match, MOFs with the same lattice structure as that in the MOF core are favorable for the shell. To demonstrate the

 

universality of the present approach, ten typical sandwich-like nanostructures: two Fe-MIL-101@Pt@Fe-MIL-101 with shell thicknesses of about 9.2 nm and 22.0 nm, two Cr-MIL-101@Pt@Fe-MIL-101 with shell thicknesses of about 2.8 nm and 8.8 nm, one Cr-MIL-101@Pt@Cr-MIL-101 with a shell thickness of about 5.1 nm, one Fe-MIL-101@Ru@Cr-MIL-101 with a shell thickness of around 8.3 nm, one MOF-525(Zr)@Pt@MOF-525(Zr) with a shell thickness of around 26.5 nm, one UiO-66(Zr)@Pt@UiO-66(Zr) with a shell thickness of around 11.2 nm, one UiO-67(Zr)@Pt@UiO-67(Zr) with a shell thickness of around 24.1 nm, and one MOF-74(Co)@Pt@MOF-74(Co) with a shell thickness of around 8.4 nm were successfully prepared by the authors. Another independent group also recently reported MOF/Pt/MOF composites *via* a similar synthetic strategy.[173] Fe-MIL-100 and Al-MIL-101-$NH_2$ ($Al_3O(OH)(H_2O)_2(BDC\text{-}NH_2)_3\cdot nH_2O$) were selected for investigation in this study. The thickness of the MOF shell was adjusted by controlling the number of assembly cycles, and Fe-MIL-100@Pt@Fe-MIL-100 with shell thicknesses of around 11 nm, 24 nm, and 35 nm was obtained with two, four, and six cycles of assembly, respectively.

### 2.4. One-step synthesis of MNPs/MOFs

Although the above stepwise approaches show great success in the synthesis of MNP/MOF composites with controlled composition and structure, a facile and efficient one-step synthesis is urgently desired. The most simple and direct approach is to mix the metal precursor and starting materials for the MOF together, followed by a self-assembly process to afford MNP/MOF composites. In the reaction process, DMF and/or $H_2$ were used as mild reductants for metal precursors. Compared with previous methods, this methodology is straightforward but it usually requires specific atoms or functional groups in the organic linkers to trap the metal precursors.

Tang's group reported a core–shell Au@MOF-5 nanoconstruction with a single Au NP core coated with a uniform MOF-5 shell by a one-step synthesis strategy.[174] Unlike the common multi-step method to form MNP/MOF composites, the core–shell Au@MOF-5 was prepared by directly mixing both the Au and MOF precursors ($HAuCl_4$, $Zn(NO_3)_2\cdot 6H_2O$, and $H_2BDC$) in the reaction solution containing DMF, PVP, and ethanol. Under the reaction conditions, $HAuCl_4$ was first reduced to Au NPs with DMF; subsequently, MOF-5 spontaneously grew on the surface of the PVP-capped Au NPs. The thickness of the MOF shell can be controlled by simply changing the amount of precursor. With a similar one-step synthesis, bimetallic alloy NPs confined in a MOF matrix were also achieved by Zhu and coworkers.[175] They prepared a core–shell structured AgPd@Fe-MIL-100 composite by directly mixing $AgNO_3$, $Pd(NO_3)_2$, and MOF precursors ($FeCl_3$ and $H_3BTC$) in the reaction solution containing PVP, DMF, and ethanol. The $AgNO_3$ and $Pd(NO_3)_2$ were first reduced to AgPd alloy NPs with DMF within 20 min at 413 K, followed by the formation of MIL-100(Fe) on the surface of the PVP-modified AgPd NPs, until a uniform AgPd@Fe-MIL-100 composite was produced.

It was found that PVP cannot always effectively prevent the aggregation of MNPs during the one-step synthesis process. Li and coworkers developed another one-step strategy to encapsulate small MNPs inside MOFs.[176] They allowed the Pd(II) complex to be coordinated with a pre-designed organic linker involving a 2,2-bipy unit, which contained two neighboring, chelating N sites, to give metal-incorporated ligands. Upon MOF formation, the involved Pd(II) can be reduced to yield uniformly distributed Pd NPs ($3.0 \pm 0.5$ nm) inside the MOF cavities. The anchoring sites on the ligand and the geometry of the MOF might synergistically limit the aggregation of the MNPs and fix them inside the cavities during the reduction. Improving this strategy one step further, the same group recently prepared tiny Pt NPs, with control over the size and spatial distribution, embedded in a UiO-66 matrix, by employing acetic acid as modulator for the MOF and/or $H_2$ as an additional reducing agent.[177] Owing to the much slower rate of formation of Pt NPs by reduction of DMF only, compared to the generation of UiO-66, most of the Pt NPs were not well embedded in the MOF, thus leading to an uneven and uncontrollable distribution of Pt NPs.[178] However, the reduction rate of Pt NPs can be markedly increased with the help of $H_2$ (Fig. 15). $H_2PtCl_6$ was first reduced to Pt NPs in a short time at 393 K in the presence of

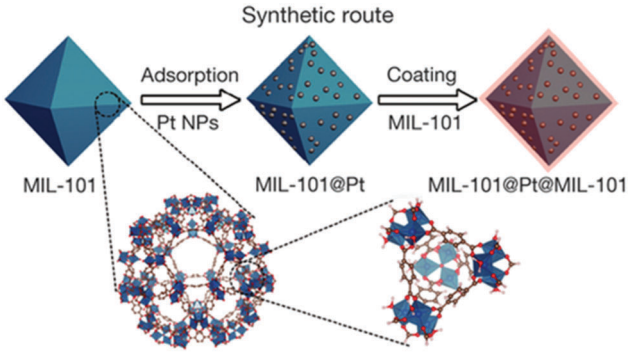


Fig. 14 Synthetic route to generating sandwich-like MIL-101@Pt@MIL-101, comprising Pt NPs sandwiched between a core and a shell of MIL-101. Reproduced from ref. 172 with permission from Nature Publishing Group, copyright 2016.

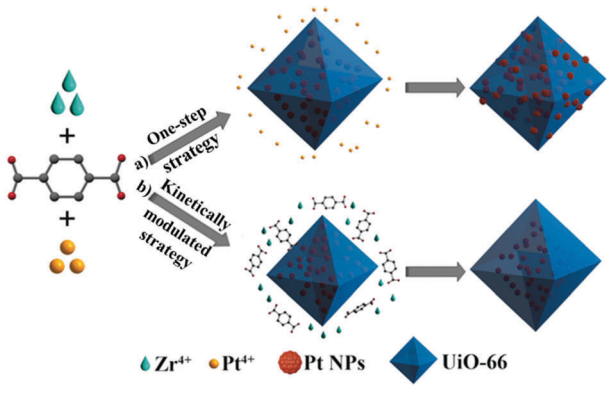


Fig. 15 Incorporation of Pt NPs in MOFs through (a) an *in situ* one-step strategy by the reduction of DMF only and (b) a kinetically modulated *in situ* one-step strategy. Reproduced from ref. 177 with permission from Wiley-VCH, copyright 2016.

both $H_2$ and DMF as reducing agents. The Pt NPs ($1.7 \pm 0.3$) generated *in situ* might preferentially combine with the soft C–N group of DMF, while $Zr^{4+}$ and MOF would show a preferential interaction with the hard C═O group of DMF. Thus, DMF served as a bridge between the MOF precursors and Pt NPs, inducing preferential anisotropic growth of UiO-66 on the surface of Pt NPs rather than self-nucleation.

# 3. Characterization tools

As MNP/MOF composites are complex systems with organic and inorganic components, various analytical and spectroscopic tools should be employed for their characterization. Different characterization tools give respective information on the structure, composition, and pore properties. The combined characterization results obtained by various methods enable us to understand the composite materials more comprehensively. It is worth noting that, to understand the status of catalysts during the reaction, their characterization is necessary both before and after catalytic reactions.

## 3.1. Composition determination

To clarify the detailed compositions of MNP/MOF composites, the basic characterization tools, including inductively coupled plasma (ICP) spectroscopy, elemental analysis, infrared (IR) spectroscopy, UV-vis spectroscopy, and nuclear magnetic resonance (NMR) spectroscopy, are commonly employed during the synthesis procedure.

## 3.2. Powder X-ray diffraction

Powder XRD is one of the most important characterization techniques to check the crystallinity and phase purity of almost all materials. For MNP/MOF composites, powder XRD is of paramount importance due to the following reasons. (1) Most MOFs are not very robust and their structures are prone to collapse during the catalytic reaction, even during the preparation of the composite and especially under harsh conditions. The stability of MOFs is a significant concern with respect to their catalytic application. Therefore, the investigation of phase purity, crystallinity, and structural integrity of MOFs, based on powder XRD, is almost indispensable. (2) Powder XRD patterns of MNP/MOF composites offer preliminary evaluation of the MNP sizes based on the Scherrer equation ($D = K\lambda/\beta \cos\theta$, where $D$ is the crystallite size, $K$ is a dimensionless shape constant, $\lambda$ is the X-ray wavelength, $\beta$ is the full width at half-maximum of the diffraction peak, and $\theta$ is the Bragg angle). (3) In particular, examination of the powder XRD pattern is usually necessary for MNP/MOF composites after catalytic reactions, in order to evaluate whether or not the MOF structure and/or the MNP sizes are retained.

## 3.3. $N_2$ sorption

A uniform pore size and large surface area are important features of MOFs. $N_2$ sorption is an effective way to characterize the pore size distribution and pore volume as well as the surface area of MOFs before and after both loading MNPs and catalytic reactions. Moreover, to evaluate whether or not a MOF structure is maintained after catalysis, $N_2$ sorption is able to provide even greater sensitivity than that of powder XRD data; the latter does not change significantly upon degradation of a small percentage of the MOF.

It is noteworthy that the decrease in the surface area of the MOF after loading MNPs is not suitable as an individual criterion to evaluate whether MNPs are incorporated inside MOF pores. In almost all cases, considering the mass occupation of MNPs, the introduction of MNPs will lead to a decrease in the surface area of the MOFs, to a certain degree. It is undeniable that the surface area of a MOF presents an apparent decrease if MNPs are embedded inside it and/or located at the pore entrance to block the access to the internal surface (in both cases, the migration and aggregation of MNPs will be obstructed by the MOFs to some extent).

## 3.4. X-ray photoelectron spectroscopy

X-ray photoelectron spectroscopy (XPS) is a powerful tool for understanding the electronic structure of MNP/MOF composites. XPS can determine the oxidation state of different species in MNP/MOF composites. For example, the remaining XPS signals of Pd between Pd@UiO-66 and polydimethylsiloxane (PDMS) coated Pd@UiO-66, the latter being obtained by treatment at 573 K, indicate that Pd is uncharged during the heating process.[91] Moreover, XPS is an effective way to identify whether the MNPs are in an alloy state. Chen *et al.* introduced Ag and Pd into the cavity of MIL-101 by a double solvent approach to give PdAg@MIL-101. The XPS results showed that both Pd and Ag are in reduced states and the 3d peaks for Pd(0) and Ag(0) in PdAg@MIL-101 shift to lower binding energies by $\sim$0.2 and $\sim$0.8 eV, respectively, in comparison to those in monometallic Pd@MIL-101 and Ag@MIL-101. The 3d peaks for Ag(0) shift gradually to lower binding energies with decreasing contents of Ag, and the $3d_{5/2}$ peak of Pd(0) also gradually shifts to lower binding energies with decreasing contents of Pd in PdAg@MIL-101. Such observed shifts indicate the formation of PdAg alloy NPs in MIL-101.[82] In addition, the transfer of electrons between MNPs and MOFs can be evidenced by XPS. For MIL-101@Pt composites, a partial transfer of electrons from Pt NPs to MIL-101(Fe) occurs, whereas there is no obvious electron transfer between Pt NPs and MIL-101(Cr). This slight change in the Pt electron density in MIL-101@Pt catalysts can cause significant differences in their hydrogenation activity.[172]

## 3.5. Electron paramagnetic resonance

Electron paramagnetic resonance (EPR) spectroscopy is sensitive to the bulk properties of a sample and has been employed to study small Ag clusters located in MOFs. The EPR spectrum of Ag@MOF exhibits a well-defined isotropic quartet centered at $g = 2.001$, indicating the formation of $Ag_3(0)$ clusters.[179] EPR spectroscopy has also been used to verify redox reactions during the *in situ* formation of MNPs/MOFs. For example, a MOF involving a redox-active $Ni^{II}$ square-planar macrocyclic complex, $[Ni(C_{10}H_{26}N_6)](ClO_4)_2$, was immersed in a methanolic solution

 

of $AgNO_3$ at room temperature. The redox reaction between the $Ag^{I}$ ions and the $Ni^{II}$ macrocycles of the host occurred rapidly. The EPR spectrum of the resulting solid shows peaks at $g$ = 2.183 and $g$ = 2.024, indicative of tetragonally distorted $Ni^{III}$ species, and a peak at $g$ = 2.005 for Ag NPs.[103] In addition to redox-active metal centers, redox-active $ntb^{3-}$ organic species in a porous MOF were employed to reduce noble metal precursors. After immersing the MOF in an acetonitrile solution of $Pd(NO_3)_2$ for 30 min, a brown solid was formed. The EPR spectrum showed a peak at $g$ = 2.003, which belongs to the oxidized $ntb^{3-}$ species with free radicals, indicating that a redox reaction occurred between $Pd^{2+}$ and $ntb^{3-}$.[106] Moreover, EPR spectroscopy is an effective method for exploring the reaction mechanism of a photocatalysis over MNP/MOF composites. Jiang's group demonstrated that the location of Pt NPs inside or on the surface of UiO-66-$NH_2$ was directly correlated with the activity of photocatalytic hydrogen production by water splitting. EPR spectra reveal the generation of a $Zr^{III}$ intermediate due to electron transfer in the above samples during photocatalysis. Pt@UiO-66-$NH_2$ gave a stronger $Zr^{III}$ signal and higher activity than Pd/UiO-66-$NH_2$, which were probably caused by much accelerated electron-transfer in the former catalyst.[149]

### 3.6. Microstructural characterization

The catalytic properties of MNP/MOF composites are closely related to their compositions and microstructures. Therefore, to better understand the catalytic properties of MNP/MOF composites, it is necessary to conduct microstructural observations on all catalysts. Scanning electron microscopy (SEM) determines the size and morphology of MOFs and MNP/MOF composites on a relatively large scale. Transmission electron microscopy (TEM) determines the size, distribution, and dispersion of MNPs. Particularly, it is usually necessary to check the size and dispersity of MNPs relative to MOF particles after catalysis to ascertain the stability and recyclability of the composite catalyst. To determine the size and morphology of very tiny MNPs, high-angle annular dark-field imaging-scanning transmission electron microscopy (HAADF-STEM) is sometimes more helpful. Selected area electron diffraction (SAED) is a useful tool to check the crystallinity of MNPs and also indentify the phase based on the lattice fringe.

It is relatively difficult to identify bimetallic NPs, particularly small ones, in a core–shell or alloyed structure. To address this issue, energy-dispersive X-ray spectroscopy (EDS), elemental mapping, and electron energy loss spectroscopy (EELS) offer important information. Recently, core–shell structured Pd@Co and Pd@Ag NPs confined inside MOF pores were successfully identified by elemental mapping.[118,180]

It remains a significant challenge to determine whether MNPs are encapsulated inside MOF matrices or on their external surface, even with TEM and HAADF-STEM images. In the early stages, it was simply thought that MNPs with sizes smaller than the MOF pore diameters were incorporated in MOFs, while they would be attached to the MOF surface if they were larger than the pore sizes—this is not necessarily correct according to the current view. To meet this challenge, the tomographic

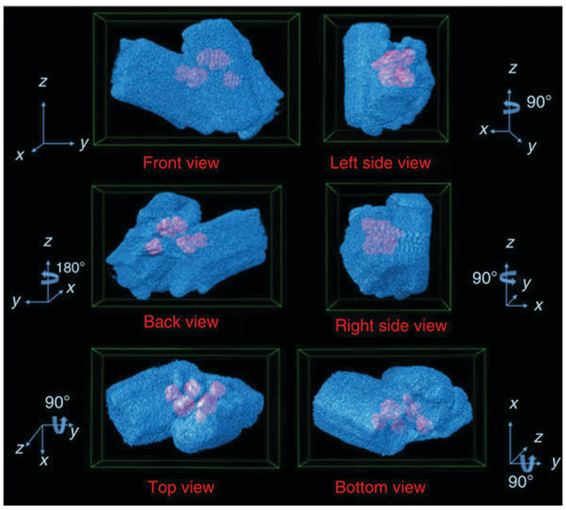


Fig. 16 Six projected images of 3D visualization of tomographic reconstruction of Pt–Ni frame@Ni-MOF-74. Reproduced from ref. 161 with permission from Nature Publishing Group, copyright 2015.

reconstruction of a MNP/MOF composite has been recognized as an effective technique, which affords 3D spatial distributions of both components with distinct contrast.[82,113,117,120,121,134,161,179,181] Li *et al.* fabricated a Pt–Ni frame within Ni-MOF-74. The morphology and spatial distribution of the Pt–Ni frame@Ni-MOF-74 structure were examined by tomographic reconstruction (Fig. 16). The tomographic images were reconstructed based on a series of 2D HAADF-STEM data, which were obtained at consecutive tilt angles from $-72^{\circ}$ to $72^{\circ}$ with $4^{\circ}$ tilt increments. Based on the differences in Z-contrast between the Pt–Ni frame and MOF, the 3D tomography data of the Pt–Ni frame@Ni-MOF-74 structure were finally obtained. The tomographic reconstruction images demonstrated that the Pt–Ni frames were fully encapsulated by Ni-MOF-74.[161] It is worth noting that some MOFs are vulnerable to long-term exposure to electron beams, especially those with high energy. As indicated in a previous report,[179] TEM observation of Ag@MIL-68 under electron beam irradiation causes damage to the MOF network, resulting in the aggregation of Ag NPs larger than MOF pore sizes in resultant images—this is an artefact because the original $Ag_3$ clusters, characterized by EPR spectra, are small enough to be incorporated inside the MOF pores. Bright-field TEM tomography was reported to be able to lower the electron beam damage to MOFs during the long time needed for the tomographic reconstruction.[182] Furthermore, a TEM image of an ultrathin slice can also be used to determine whether MNPs are located inside or on the surface of the MOF. Only the MNPs loaded at the outside surface of the MOF can be observed bulging out from slice edges.[176,183] Chen *et al.* observed that almost no MNPs can be seen bulging from the MOF edges in an ultrathin slice of a $Pd_7Ni_3$-in-UiO-67 composite, suggesting that most of the MNPs were encapsulated inside the UiO-67 matrix.[183] With the above points in mind, TEM studies on MNP/MOF composites should be conducted with great care.

### 3.7. X-ray absorption spectroscopy

Although TEM observation is very powerful for understanding the microstructure of MNP/MOF composites, it provides only limited information on ultrasmall particles. As an additional support, X-ray absorption spectroscopy (XAS) can precisely determine the size, coordination environment, and chemical form of very small metal clusters or even single atoms; this information is of great importance in catalysis. Jiang *et al.* successfully incorporated ultrafine Au clusters into a pre-designed MOF with fluorinated channels by solid grinding. No evident Au clusters could be found by TEM and HAADF-STEM observation. In contrast, Au $L_{III}$-edge X-ray absorption near-edge structure (XANES) and extended X-ray absorption fine structure (EXAFS) spectral analyses demonstrated the presence of Au(0) and ultrafine Au clusters with an average atom number of $\sim$2.5 (Fig. 7).[134]

## 4. Important concerns

Significant progress has been achieved by more than 10 years of intensive studies on MNPs/MOFs. To further develop this field, some important concerns and challenges indicated below, some of which are interdependent, should be addressed.

The MOF stability remains an ongoing concern. The classical MOF-5 and MOF-177 were used to stabilize MNPs in the early stages before being gradually replaced by more stable MOFs, such as ZIF-8, UiO, and the MIL series of MOFs, which can guarantee stability during catalytic recycling under most reaction conditions. Fortunately, more and more stable MOFs have been reported in recent years, for example, Zr carboxylate-based MOFs,[184–186] which will promote the development of MNPs/MOFs in catalysis.

The size control of MNPs stabilized by MOFs is another important concern. While MOF cavities can theoretically prevent the migration and aggregation of MNPs, their size is difficult to control as this is affected by many factors: (1) the type of metal precursor; (2) the concentration of the metal precursor; (3) the nature of the solvent; (4) the reductant for the metal precursor; (5) the nature of the MOF, and (6) the synthetic conditions for producing the MNPs/MOF. Several of the parameters indicated above usually work together to determine the final results. In addition, the particular functional groups or MOF pore environment interacting with the MNPs significantly influences the size of the MNPs.[187]

Direct evidence regarding the location of MNPs relative to MOF particles, that is, whether MNPs are inside the MOFs or on their outer surfaces, remains uncertain in some reports. Although we have mentioned that tomographic reconstruction works for the above, the measurement is time-consuming and relies heavily on the experience of the TEM operator. Moreover, the attachment of a correlative accessory to the microscope is necessary. All these factors render this characterization technique unavailable for many scientists. Therefore, it is necessary to develop suitable techniques that can offer relevant structural information and are easily accessible by most scientists.

Along with the development of this topic, the synthesis of MNP/MOF composites containing MNPs with particular sizes and morphologies is highly desirable. While the introduction of pre-synthesized MNPs with special sizes and morphologies for subsequent MOF growth works to this end, the problem of this strategy lies in the large amount of surfactant on the surface of the MNPs, which might not meet the requirements of particular applications. In contrast, the preformation of MOFs followed by incorporation of a metal precursor and reduction is able to provide surface-clean MNPs but does not realize satisfactory size and morphology control. This creates a dilemma regarding the expected target. Xu and coworkers immobilized cubic Pt, tetrahedral Pd, and octahedral PtPd NCs in MIL-101 by an incipient solution impregnation method in combination with a reduction process by using a CO–$H_2$–He mixture as the gas-phase reducing agent.[188] The formation of Pt and Pd polyhedra was directed by preferential binding of CO on their (100) and (111) facets. Moreover, due to a higher adsorption enthalpy of CO on Pt than on Pd, PtPd NCs showed a Pd-rich core and a Pt-rich shell. Despite this success, further adjustment of the resultant MNPs with respect to morphology and size was not realized. To our knowledge, there has not yet been an effective and general solution to overcome this challenge, *i.e.*, the synthesis of surface-clean MNPs with specific morphologies confined in MOFs.

It is worth noting that, rather than being limited to the cavities offered by the pristine MOF structures, additional pore space can be created during MOF assembly. The newly generated pores with usually mesoporous sizes are suitable for accommodating MNPs, and the interspace between an MNP core and MOF shell acting as a nanoreactor would be ideal for hosting catalytic reactions, improving reaction efficiency. A yolk–shell Au@ZIF-8 nanostructure, recently created with a sacrificial $SiO_2$ template strategy (Fig. 13), exhibited a remarkably enhanced activity compared to the corresponding core–shell Au@ZIF-8 composite toward the aerobic oxidation of alcohols.[169]

## 5. Synergistic catalysis between MNPs and MOFs

The main targets of the development of MNP/MOF composites are to broaden the scope of catalytic reactions and enhanced catalysis. In other words, one needs to ask how MNP/MOF composites can enable improved catalysis. It is necessary to recognize the roles of both components and how they synergize to achieve enhanced properties, with suitably designed MNP/MOF composite catalysts. In this section, the synergistic effect between MNPs and MOFs toward catalysis will be discussed in detail with examples taken from previously discussed studies.

### 5.1. MNPs as active centers, stabilized by MOFs

Given their permanent porosity and tunable pore sizes/environment, MOFs are ideal candidates for the stabilization of MNPs. Small MNPs can be confined or stabilized by MOFs, showing excellent catalytic activity and recyclability.[189–214]

 

In these composites, MNPs are active centers and MOFs behave as stabilizers for MNPs; this represents the simplest synergy between MNPs and MOFs and is demonstrated by a series of important publications in this field. In general, almost all reported MNP/MOF catalysts may include this basic synergy—MNPs and MOFs as active sites and stabilizer, respectively.

Palladium-catalyzed carbon–carbon coupling reactions of aryl halides, such as Suzuki–Miyaura and Ullmann reactions, are of great importance as versatile routes to construct biaryl units in organic synthesis.[215,216] Yuan *et al.* reported water-mediated coupling reactions of aryl chlorides over Pd/MIL-101.[89] The large surface area, large pore sizes/openings, and high stability of MIL-101 are desirable for depositing Pd NPs for catalytic applications. The Suzuki–Miyaura coupling of 4-chloroanisol with phenylboronic acid over Pd/MIL-101 was efficient when using NaOMe as a base. Diverse substrates with electron-rich/-poor aryl chlorides can give the corresponding biphenyl compounds with excellent yields. Moreover, the catalytic activity of Pd/MIL-101 for the Ullmann coupling reaction was also excellent. Various aryl chlorides can be smoothly homocoupled to give their corresponding products with high yields. The Pd/MIL-101 catalyst was stable, showed negligible metal leaching, and maintained high catalytic activity even after a number of cycles. Subsequently, Pd/MIL-101-$NH_2$ and Pd/MIL-53-$NH_2$ were investigated with respect to Suzuki–Miyaura reactions and presented excellent activity.[196,217,218] The amino group might effectively prevent the aggregation of Pd NPs, achieving better dispersion.

Hwang *et al.* rationally fabricated Pd@MIL-101 with Pd NPs (2–4 nm) inside MOF pores for efficient Heck reactions of acrylic acids with iodobenzene.[97] Likewise, Pd NPs encapsulated in other MOFs exhibited excellent catalytic performances for Heck reactions.[101,219] In addition, a Pd/MOF composite was also employed as a catalyst for an $A^3$ (alkyne, amine, and aldehyde) coupling reaction.[220] The Pd NPs were loaded to a 2D layer structured MOF, {[Zn(Himdc)(bipy)$_{0.5}$]·DMF} (bipy = 4,4′-bipyridine, Himdc = 4,5-imidazoledicarboxylate), with carboxylate functional groups decorated on the pore surface. Pd NPs (1–2 nm) were found to be well distributed throughout the MOF. The hybrid Pd@MOF catalyzed the three-component coupling reaction of benzaldehyde, piperidine, and phenyl acetylene to form propargylamine derivatives. Almost simultaneously, another group independently synthesized Au functionalized IRMOF-3 catalysts by post-synthetic covalent modification. The Au/IRMOF-3 catalysts provided an efficient and economic route for the one-pot synthesis of structurally divergent propargylamines *via* three-component coupling of alkyne, amine, and aldehyde without the need for any additive or an inert atmosphere.[221] The Au/IRMOF-3 catalyst was easily recycled at least five times. In addition, the Ag/MOF also presented activity for $A^3$ coupling reactions.[222]

Both Au/MOF and Ag/MOF composites were also found to be active in the reduction of 4-nitrophenol (4-NPh).[96,100,153,223] Bimetallic AuAg NPs with a size range of 2–6 nm supported on ZIF-8 were reported for the catalytic reduction of 4-NPh by $NaBH_4$ in water.[96] Compared with monometal catalysts embedded in ZIF-8, such as Au/ZIF-8 and Ag/ZIF-8, the catalytic activity was significantly improved by applying the AuAg/ZIF-8 catalyst, clearly illuminating the synergistic effect between Au and Ag species. Moreover, the catalyst exhibited an excellent recycling performance. This catalyst is not limited to 4-NPh; a series of nitro compounds can be reduced over Pd@MIL-101, where *in situ* generated hydrogen from $NH_3BH_3$ can efficiently boost their hydrogenation.[114] A variety of nitro compounds were selectively and efficiently reduced to the corresponding amines. When $NH_3BH_3$ was replaced by an $H_2$ flow while other conditions remained unaltered, the reduction of nitrobenzene was completed 20 times more slowly than in the process with $NH_3BH_3$.

To realize highly efficient dehydrogenation of $NH_3BH_3$ by hydrolysis, Xu's group reported that Pt NPs well encapsulated in MIL-101 were fabricated and displayed outstanding catalytic activity, where hydrogen could be completely released within a short time.[113] Subsequently, the same group synthesized an AuNi@MIL-101 catalyst, which exhibited superior catalytic activity in the hydrolytic dehydrogenation of $NH_3BH_3$ to its monometallic counterparts.[117] In a recent study, Jiang and coworkers incorporated core–shell Pd@Co, Pd, Co, and PdCo NPs into MIL-101, as well as Pd@Co NPs supported on MIL-101 (denoted as Pd@Co/MIL-101), for the hydrolytic dehydrogenation of $NH_3BH_3$. The catalytic results show that Pd@Co@MIL-101 possesses the highest activity, revealing the synergistic effect between the Pd core and Co shell. The encapsulated Pd@Co NPs exhibited much better stability than the core–shell NPs on the external surface of the MOF, highlighting the better synergistic effect for the catalytic process in the former catalyst: MNPs act as active centers and the MOF stabilizes them.[118]

Compared with noble metal NPs, non-noble metal NPs possess obvious advantages due to their abundant reserves on the earth and low prices. Therefore, the synthesis of small and high-activity non-noble metal NPs is desirable in practice. Ni/MOF composites were widely studied.[128,129,200,224] ZIF-8 was chosen as the host matrix to load Ni NPs (2–3.4 nm) *via* gas-phase infiltration of Ni(cp)$_2$ to give Ni/ZIF-8, with which $NH_3BH_3$ was rapidly hydrolyzed to $H_2$ at room temperature with no significant decrease in catalytic activity even after five runs of hydrolytic reactions.[128] CuCo/MIL-101 also exhibited excellent activity with a very high turnover frequency (TOF) of 51.7 $mol_{hydrogen}\ mol_{cat}^{-1}\ min^{-1}$ toward the hydrolytic dehydrogenation of $NH_3BH_3$.[225]

Formic acid decomposition is an alternative way to realize chemical hydrogen storage.[226] A series of MNPs were immobilized to ethylenediamine-grafted MIL-101, among which AuPd/ED-MIL-101 exhibited higher catalytic activity than the monometallic and alloy NP composites in hydrogen generation from formic acid. Formic acid can be completely converted to $H_2$ and $CO_2$ at 363 K in the presence of the AuPd/ED-MIL-101 catalyst, in which the synergistic interaction between Pd and Au was assumed to play a crucial role.[98] Yamashita's group demonstrated that Pd/Ti-MIL-125-$NH_2$ ($Ti_8O_8(OH)_4$(BDC-$NH_2$)$_6$) had a high activity for hydrogen production from formic acid even at ambient temperature.[227] The small Pd NPs with a mean diameter of 3.1 nm were well encapsulated by the matrix of Ti-MIL-125-$NH_2$. However, the size of the Pd NPs was found not to be the most

important factor for the activity, which was essentially caused by the amine functional groups. The reaction intermediate was Pd-formate, while the weakly basic $-NH_2$ group acted as a proton scavenger, forming $-^{+}HNH_2$ species, and then the Pd-formate species underwent β-hydride elimination to produce $CO_2$ without the unfavorable formation of CO. Therefore, in this system, the MOF not only acted as a stabilizer for Pd NPs but also provided a platform to synergize the functions of the amino groups and Pd NPs to enhance the catalytic performance.

Liquid-phase aerobic oxidation of alcohols, being of great interest in both academia and industry, was extensively studied over MNP/MOF catalysts.[178,187,198,211,228–234] Li and coworkers prepared a composite catalyst of highly dispersed Pd NPs ($2.5 \pm 0.5$ nm) deposited onto MIL-101 by using a simple colloidal method. The resulting Pd/MIL-101 catalyst was very active, even at ambient temperature, using air instead of pure $O_2$, toward liquid-phase aerobic oxidation with a wide range of alcohols.[232] The solvent-free oxidation of benzyl alcohol gave a remarkably high TOF of approximately 16 900 $h^{-1}$. Interestingly, the catalytic activity was significantly suppressed when ethylenediamine was grafted onto the uncoordinated Cr sites in MIL-101, indicating that the open Cr sites might play a key role in promoting the oxidation of alcohols. The oxidation of alcohols was also achieved over MNPs/MOFs *via* photocatalysis. Single- or multi-core Au@ZIF-8 nanocomposites were synthesized by adjusting the incubation temperature and time at the initial reaction stage. Due to the Au localized surface plasmon resonance (LSPR), light absorption of single- and multi-core Au@ZIF-8 was around 530 nm and 540 nm, respectively. The photocatalysis of benzyl alcohol oxidation over Au@ZIF-8 displayed 25.8% conversion for single-core Au@ZIF-8 and 51.6% for multi-core Au@ZIF-8 upon light irradiation ($\lambda > 400$ nm) for 24 h. So, the LSPR of Au takes part in the catalysis in addition to the basic synergy between Au and ZIF-8, and the conversion difference might be due to plasmonic coupling between Au NPs in multi-core structures.[233]

### 5.2. MNPs as active centers, with MOFs stabilizing MNPs and controlling size selectivity

Along with the perfect control of MNPs encapsulated inside MOFs, the uniform pore size of the MOF shell allows it to function as a molecular sieve for the MNP/MOF composites. Therefore, MOFs can selectively allow substrates/products that are smaller than the MOF pores to pass through and access the MNPs (active sites) while blocking larger molecules. Such a size-exclusion effect finds important application in MNPs@MOFs in size-selective catalysis.[81,99,140,155,158,165,170,235–239]

Core–shell MNPs@MOF nanostructures have attracted recent research interest because of their potential application in catalysis. Integrating the functions of the MNP core and the MOF shell would efficiently endow new properties and expand the scope of application of the obtained MNPs@MOF composites. Lu *et al.* synthesized a series of core–shell MNP@ZIF-8 nanostructures through the strategy of introducing MNPs for subsequent MOF growth and demonstrated the synergistic effect between the MNP core and ZIF-8 shell.[140] The core–shell nanostructure denoted as Pt/PVP/ZIF-8 integrated the catalytic properties of Pt NPs and the molecular sieving capability of the ZIF-8 matrix to probe the liquid-phase hydrogenation of *n*-hexene *versus* that of *cis*-cyclooctene. Pt/PVP/ZIF-8 realized the hydrogenation of the linear *n*-hexene molecule and a similar conversion was obtained for three consecutive runs (7.3%, 9.6%, and 7.1% for the first, second, and third runs, respectively). However, this nanostructure showed no propensity to catalyze the hydrogenation of *cis*-cyclooctene, which required a larger reaction space; this was consistent with the small opening of ZIF-8 and the indicated encapsulation of Pt NPs inside ZIF-8. In contrast, although pure ZIF-8 crystals showed no catalytic activity towards either *n*-hexene or *cis*-cyclooctene, Pt NPs loaded onto carbon nanotubes (denoted as Pt/CNTs) displayed indiscriminate catalytic activities for alkene (*i.e.*, *n*-hexene and *cis*-cyclooctene) hydrogenation. Compared with the Pt/PVP/ZIF-8 catalyst, Pt/ZIF-8 prepared by a solution impregnation method showed lower selectivity for the catalytic hydrogenation of *n*-hexene *versus* that of *cis*-cyclooctene. The non-negligible residual activity for the hydrogenation of *cis*-cyclooctene was due to the Pt NPs formed on the outer surface of ZIF-8, further indicating the molecular sieving function of the MOF.

Stephenson *et al.* substituted the 2-methylimidazolate linkers in Pt@ZIF-8 with imidazole to form Pt@SALEM-2. Both catalysts were active for the hydrogenation of 1-octene, whereas the hydrogenation of *cis*-cyclohexene occurred only when using Pt@SALEM-2 as a catalyst, due to its larger apertures. The largest substrate, β-pinene, was unreactive with $H_2$ when either catalyst was employed, highlighting the size exclusion effect (Fig. 17).[237] Moreover, Pt@ZIF-8 exhibits excellent regioselective hydrogenation. Terminal alkenes and alkynes were readily hydrogenated while internal unsaturated sites were unreacted. For example, the regioselective hydrogenation of the terminal C=C bond in linear alkene 1,3-hexadiene was realized with Pt@ZIF-8 to give 3-hexene with 95% selectivity, but only 20% 3-hexene was obtained over a Pt/C catalyst.[238]

In addition, the Pt@ZIF-8 composite with highly dispersed uncapped Pt NPs (~2.0 nm) was demonstrated for size-selective hydrogenation of alkenes under mild conditions.[158] The catalytic

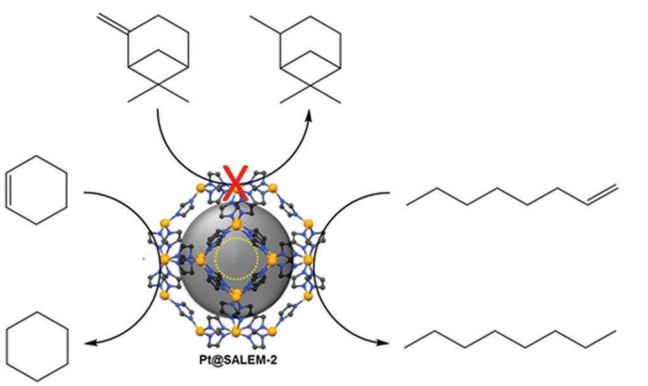


Fig. 17 Schematic illustration showing size-selective catalysis over Pt@SALEM-2. Reproduced from ref. 237 with permission from the American Chemical Society, copyright 2016.

 

performance of Pt@ZIF-8 was investigated for olefin hydrogenation under 1 bar $H_2$ at 293 K. The alkene 1-hexene has a molecular width of 1.7 Å while *cis*-cyclooctene has a molecular width of 5.5 Å, which exceeds the size of the pore opening in ZIF-8 (3.4 Å). Under the same conditions, Pt@ZIF-8 exhibited excellent activity for the hydrogenation of 1-hexene, but almost no hydrogenation products of *cis*-cyclooctene were observed. In contrast, Pt/C can catalyze the hydrogenation of both 1-hexene and *cis*-cyclooctene, and no obvious differences were observed. Recently, Aguado *et al.* employed the imidazolate-based MOF, SIM-1 ($Zn(MIM)_2$, MIM = 4-methyl-5-imidazolecarboxaldehyde), to construct a core–shell composite with $Pt/Al_2O_3$ as the core.[239] A homogeneous SIM-1 layer at the surface of $Pt/Al_2O_3$ was formed by a solvothermal process. Due to the narrow pore opening of SIM-1 (5 Å), ethylene can easily cross the SIM-1 shell and be converted to ethane, but toluene, with a larger molecular size, was excluded, although the hydrogenation of both toluene and ethylene over $Pt/Al_2O_3$ can be achieved.

As well as ZIF-8, Pt NPs incorporated inside UiO-66 also perform well in size-selective catalysis.[99,143,177] Liquid-phase hydrogenation of hexene, cyclooctene, *trans*-stilbene, *cis*-stilbene, triphenyl ethylene, and tetraphenyl ethylene was carried out to evaluate the size selectivity of Pt@UiO-66. The catalytic activity with these substrates was distinctly different due to their different molecular sizes. Hexene (molecular size: 2.5 Å), which is small enough to diffuse through the aperture of the UiO-66 (6 Å), can be completely converted after 24 h, while 66%, 35%, and 8% conversions were obtained for cyclooctene, *trans*-stilbene, and triphenyl ethylene, respectively, which have gradually increasing molecular sizes (cyclooctene: 5.5 Å, *trans*-stilbene: 5.6 Å, triphenyl ethylene: 5.8 Å); thus, the diffusion limitation caused by the UiO-66 frame cannot be ignored.[143] Particularly, no propensity to catalyze the hydrogenation of the sterically more demanding tetraphenyl ethylene (6.7 Å) was observed. A similar phenomenon was observed with clean Pt NPs completely encapsulated within UiO-66 by Li's group.[177] The hydrogenation of 1-hexene and tetraphenylethylene over the Pt@UiO-66 composites was operated at 298 K under atmospheric $H_2$ pressure. For comparison, the hydrogenation of 1-hexene and tetraphenylethylene over Pt/UiO-66, which was obtained by solution impregnation, was also carried out. Pt@UiO-66 afforded the complete conversion of 1-hexene but no activity was detected for tetraphenylethylene within 1 h. However, with Pt/UiO-66, 73% and 15% conversions of 1-hexene and tetraphenylethylene, respectively, were obtained; here, size exclusion was less apparent as some of the Pt NPs were attached to the outer surface of UiO-66 by solution impregnation. In this case, tetraphenylethylene could be easily adsorbed onto the surface of Pt NCs without the steric-hindrance effect of UiO-66. When UiO-66 was replaced by UiO-67 with a larger pore size, size-selective catalysis could be achieved; the well confined Pd NPs only catalyzed the conversion of styrene to ethylbenzene but no activity was detected for tetraphenylethylene.[176]

Huang's group fabricated a robust catalyst based on monodisperse Pt NCs encapsulated inside the cavities of UiO-66-$NH_2$, demonstrating its chemoselective hydrogenation of

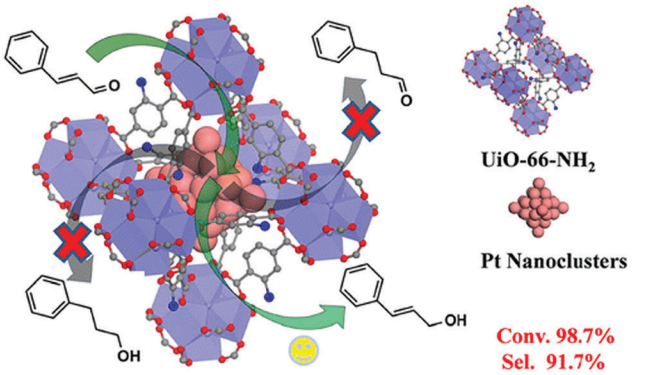


Fig. 18 Schematic illustration showing the highly chemoselective hydrogenation of cinnamaldehyde over Pt@UiO-66-$NH_2$. Reproduced from ref. 99 with permission from the American Chemical Society, copyright 2014.

cinnamaldehyde (Fig. 18).[99] While both high conversion and selectivity of cinnamaldehyde to cinnamyl alcohol were achieved in the presence of Pt@UiO-66-$NH_2$, high selectivity to cinnamyl alcohol could not be obtained over the catalyst of Pt NPs loaded onto the external surface of UiO-66-$NH_2$, Pt/UiO-66-$NH_2$. It is worth noting that various heterogeneous and homogeneous noble metal-based catalysts, including Au, Pd, Pt, Ru, Rh, and Ir, were found to be active for this reaction, but low selectivity to cinnamyl alcohol was usually observed, because C=C hydrogenation is more thermodynamically favorable than C=O hydrogenation. For example, the selectivity to cinnamyl alcohol over Pt/C was found to be ~70%. Various factors affect the selectivity in the cinnamaldehyde hydrogenation such as supports, MNP size, and additives. Among these, the steric-hindrance effect imposed by MOF pores seems to be predominant. With Pt NCs encapsulated in UiO-66-$NH_2$, the access to the Pt NCs is strongly restricted by the 6 Å triangular windows that connect the tetrahedral and octahedral cages inside UiO-66-$NH_2$. Due to the steric hindrance of UiO-66-$NH_2$, the C=C bond in the middle of cinnamaldehyde was hardly accessible to the surface of Pt compared to the C=O bond at the end of the molecule. Even at the 10th run, 98.7% conversion of cinnamaldehyde and 91.7% selectivity to cinnamyl alcohol could be obtained over Pt@UiO-66-$NH_2$ (Pt content: 10.7 wt%) after 44 h, clearly highlighting the pore size effect of the MOF in addition to the common synergistic effect between Pt and the MOF; Pt functioned as the active site and the MOF as the stabilizer of Pt.[99]

The hydrodeoxygenation process as one of the best ways to improve the quality of biofuels has been widely studied.[213,214,240,241] Xu's group fabricated two similar catalysts of surfactant-free Pd NPs immobilized on MIL-101, Pd NPs with a size of 1.0–2.2 nm incorporated into MIL-101 (denoted as Pd@MIL-101), and Pd NPs with a size of 5.0 ± 0.5 nm immobilized onto MIL-101 (denoted as Pd/MIL-101), which exhibited remarkably different reaction pathways and catalytic selectivity toward the reaction of biofuel hydrodeoxygenation.[241] Vanillin, a large component of pyrolysis oil derived from the lignin fraction, was selected as the substrate, where the transformation of the carbonyl group in vanillin into a methyl group could proceed *via* two paths: (1) direct hydrogenolysis and (2) hydrogenation/hydrogenolysis (Fig. 19).

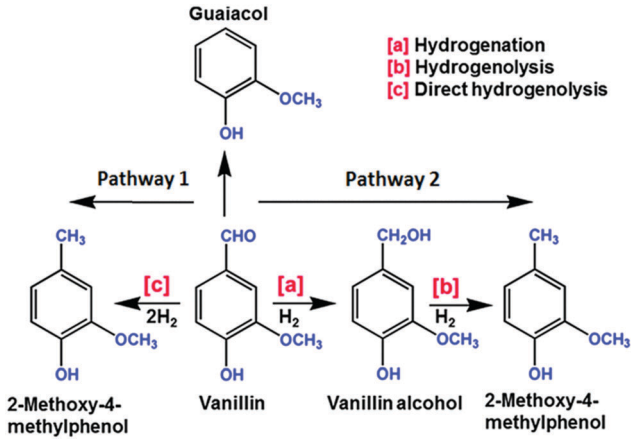


Fig. 19 Possible reaction pathways for vanillin hydrodeoxygenation. Reproduced from ref. 241 with permission from The Royal Society of Chemistry, copyright 2015.

Vanillin (49%) was converted over Pd@MIL-101 in the first 1 h with ~100% selectivity to 2-methoxy-4-methylphenol (pathway 1) under 2 bar $H_2$ at 348 K. However, Pd/MIL-101 generated a significant amount of vanillin alcohol and a low yield of 2-methoxy-4-methylphenol under the same conditions, indicating pathway (2) for Pd/MIL-101. The higher activity of Pd@MIL-101 should be attributed to the smaller size of the Pd NPs, and its outstanding selectivity to 2-methoxy-4-methylphenol might be associated with the steric hindrance and strong interaction of vanillin alcohol caused by the encapsulation of ultrafine Pd within MIL-101, resulting in blocking of reaction pathway (2).

In addition to core–shell structured composites, sandwich-like structured composites also work well toward such size-selective catalysis.[172,173,236,242] Li and coworkers reported a sandwich-like MOF/MNPs/MOF formed by the epitaxial growth of a MOF shell on the surface of a MNPs/MOF, with which the selective hydrogenation of cinnamaldehyde was investigated. Pt/MIL-100 was able to provide over 99% cinnamaldehyde conversion in 2 h with low selectivity (55%) to the target cinnamyl alcohol. With the help of the outer MIL-100 shell (a mean thickness of 11 nm) grown on Pt/MIL-100, the selectivity to cinnamyl alcohol was enhanced to 78% when cinnamaldehyde was completely consumed. MIL-100/Pt/MIL-100 with an outer shell thickness of 24 nm displayed 95% conversion with 96% selectivity to cinnamyl alcohol. The results unambiguously indicated that the selectivity to cinnamyl alcohol through C=O hydrogenation was endowed by the MIL-100 shell coating. The reduction of the C=C bond in the middle of the long substrates over the Pt NPs that were fully encapsulated by the MIL-100 shell was strongly restricted, while the C=O bond at the end of the molecule was more likely to be reduced.[173] With a similar goal, a general strategy to achieve controllable encapsulation of various NPs in ZIF-8 thin films with a sandwich-like structure was developed.[242] The NPs were initially loaded on the pre-synthesized ZIF-8 thin films by means of spin coating, and then they were coated with a new ZIF-8 thin film, repeating the above step to afford a sandwich-like structure. Pt–ZIF-8 hybrid thin films exhibited high size-selectivity in the hydrogenation of linear *n*-hexene and cycloolefins due to the synergy between the catalytic properties of Pt NPs and the size exclusion of ZIF-8 thin films. As a result, Pt–ZIF-8 hybrid thin films effectively catalyzed the conversion of *n*-hexene, but no cyclooctane was detectable under similar conditions.

Compared with core–shell nanostructures, yolk–shell nanohybrids have unique advantages, and the void, behaving as a nanoreactor, optimizes the performance of the catalysts. Tsung's group coated ZIF-8 layers onto pre-synthesized Pd@$Cu_2O$ core–shell particles with $Cu_2O$ as the sacrificial template; the $Cu_2O$ was then etched off to leave a void.[165] Gas-phase hydrogenations of ethylene, cyclohexene, and cyclooctene were chosen to study the catalytic behavior of yolk–shell Pd@ZIF-8, Pd NPs directly deposited on ZIF-8 (denoted as Pd–ZIF-8), and core–shell Pd@ZIF-8. For ethylene, all these catalysts showed similar conversion, indicating that the ZIF-8 shell had no significant influence on diffusion. For cyclooctene, neither the core–shell nor yolk–shell catalysts showed any detectable activity, but Pd–ZIF-8 showed good activity, clearly demonstrating the size exclusion effect of the ZIF-8 shell. Interestingly, the catalytic efficiency of cyclohexene hydrogenation over yolk–shell Pd@ZIF-8 and Pd–ZIF-8 was similar and higher than that over core–shell Pd@ZIF-8, which was attributed to the diffusion of the substrate. It is assumed that configurational diffusion dominates in core–shell Pd@ZIF-8, while the diffusion in the yolk–shell catalyst is a combination of configurational diffusion (shell) and Knudsen diffusion (cavity), which results in the faster diffusion speed with yolk–shell Pd@ZIF-8 and thus superior catalytic activity. Likewise, Huo's group employed a MNPs@$Cu_2O$ core–shell nanohybrid as a sacrificial template, followed by the capture of a dissociated $Cu^{2+}$ ion from $Cu_2O$ by BTC to grow HKUST-1, resulting in a unique yolk–shell MNPs@HKUST-1 composite with a petalous shell.[243] The seamless shell of HKUST-1 may serve as a molecular sieve for size-selective catalysis, and PtAu NPs encapsulated in the petalous heterostructures were active sites for liquid-phase hydrogenation of olefins. Both *n*-hexene and *cis*-stilbene exhibited complete conversion with bare PtAu NPs, while PtAu@HKUST-1 only showed activity toward *n*-hexene hydrogenation, and no conversion of *cis*-stilbene occurred. Yang *et al.* developed a facile emulsion-based interfacial reaction method to synthesize yolk–shell Pd@ZIF-8 nanospheres with controllable shell thickness, in which the ZIF-8 shell also allowed the size-selective catalysis of hydrogenation.[170] The yolk–shell Pd@ZIF-8 with a thin ZIF-8 shell showed the highest conversion (98%) for 1-hexene after 24 h, indicating that the thin ZIF-8 shell had a negligible influence on the diffusion of 1-hexene molecules. The conversion decreased to 87% when Pd@ZIF-8 with a thicker layer was used. In contrast, core–shell Pd@ZIF-8 with the thickest shell gave 58% conversion due to the low diffusion rate through the much thicker ZIF-8 shell. *trans*-Stilbene with a larger size than the pore aperture of ZIF-8 can only diffuse through the voids among ZIF-8 NCs in the shell, and its conversion decreased considerably to 4.3–1.3% with the thicker ZIF-8 shell.

 

### 5.3. MNPs as active centers, with MOFs stabilizing MNPs and concentrating gaseous reactants

In many important reactions, gas molecules are involved. Previous reports have shown that MNPs/MOFs can enrich gas molecules around the active sites, thus boosting the catalytic efficiency. The influence of MOFs on the hydrogen sorption of Pd nanocubes was reported by Kitagawa's group. The solid-state $^2$H NMR spectra indicated that the pressure of the plateau-like region in Pd@HKUST-1, where solid solution (Pd + H) and hydride (Pd−H) coexist, was greater than that in the Pd nanocubes. The total amount of hydrogen adsorption at atmospheric pressure was enhanced from 0.5 H per Pd atom in Pd nanocubes to 0.87 H per Pd atom for the Pd@HKUST-1. Moreover, the hydrogen pressure-composition isotherm of Pd nanocubes did not completely return to the starting point on reversing the process, whereas the Pd@HKUST-1 showed a fully reversible absorption/desorption response. These results indicated that the HKUST-1 coating on the Pd nanocubes can enhance the hydrogen capacity and improve the hydrogen absorption/desorption speed.[145]

Dang *et al.* demonstrated an efficient amide synthesis by atmospheric pressure aminocarbonylation over Pd/MOF-5 under moderate temperatures (353–393 K) and CO pressure (1 atm). Compared with traditional porous supports such as $SiO_2$, $Al_2O_3$, and celite, Pd stabilized by MOF-5 exhibited the best catalytic activity due to the high porosity and gas enrichment function of MOF-5. The aminocarbonylation of various aryl iodides with morpholine afforded the desired products in good yields over Pd/MOF-5.[244] Wang and coworkers demonstrated alkoxycarbonylation of aryl iodides over Zn/Ni-MOF-2 immobilized Pd NPs (denoted as Pd/MOF-2) in the presence of CO.[245] The kinetic curves for the alkoxycarbonylation reactions over Pd NPs, Zn/Ni-MOF-2, Pd/MOF-2, Pd/$TiO_2$, and commercial Pd black showed that Pd/MOF-2 gives the highest activity. The enhanced catalytic activity of Pd/MOF-2 can be ascribed to the synergistic effect: the unique structure and gas adsorption behavior of Zn/Ni-MOF-2 contribute to both the stabilization of Pd NPs and the CO enrichment, which further improved the activity of Pd NPs.

Hydrogenation with molecular hydrogen is a common reaction and is extensively involved in many chemical processes, providing atom economy and a "green" route. Recently, hydrogenation reactions over MNPs/MOFs were studied by different groups.[132,183,246–249] Zhang *et al.* demonstrated the synthesis of a series of well-defined hollow MOF (MOF-5, $Fe^{II}$-MOF-5, $Fe^{III}$-MOF-5) nanocages without a template by a facile solvothermal method. The addition of pre-synthesized PVP-modified MNPs into the synthetic system of MOF hollow nanocages yielded yolk–shell MNPs@MOF nanohybrids.[249] A challenging industrial process of selective hydrogenation of 1-chloro-2-nitrobenzene was examined, and the yolk–shell PdCu@$Fe^{III}$-MOF-5 composite presented much higher activity, with complete consumption of 1-chloro-2-nitrobenzene in 4 h, than PdCu NPs, which showed a maximum conversion of only 78% even after 8 h. Notably, the selectivity to 2-chloroaniline over PdCu@$Fe^{III}$-MOF-5 remained at 100% even after complete conversion of 1-chloro-2-nitrobenzene. The superior catalytic performance of PdCu@$Fe^{III}$-MOF-5 was ascribed to the synergistic effect between the active PdCu core and the hollow nanostructure of the MOF shell, the latter serving as a confined nanoreactor for catalysis, and hydrogen enrichment in the shell, which accelerated the hydrogenation process.

Hydrogenation of the C=C bond over MNPs/MOFs has been intensively studied.[81,250–253] In a recent study, Jiang and coworkers rationally synthesized a Pd nanocubes@ZIF-8 composite by the encapsulation of Pd nanocubes in ZIF-8 for efficient and selective catalytic hydrogenation of olefins at room temperature under 1 atm $H_2$ and light irradiation (Fig. 20 left).[81] The Pd nanocubes are not only the active sites for the hydrogenation process but also greatly promote the reaction based on their plasmonic photothermal effect—light can be converted into heat to accelerate the endothermic olefin hydrogenation. In addition, the ZIF-8 shell contributes to the reaction process by serving multiple roles: it greatly boosts the reaction by the $H_2$ enrichment effect (Fig. 20 right), acts as a "molecular sieve" to differentiate olefins with specific sizes for size selectivity, and stabilizes the Pd cores for better recyclability. Therefore, the judicious integration of the multiple functionalities of the Pd nanocubes and the MOF shell results in the multifunctional Pd nanocubes@ZIF-8 catalyst, which exhibits an excellent catalytic performance in olefin hydrogenation.

The catalytic partial hydrogenation of alkynes to alkenes is involved in many important transformations in petrochemistry and industry.[254] However, the challenge to achieve high selectivity to alkenes with high conversion of alkynes has not been overcome and related explorations have been conducted over MNPs@MOF composites.[180,238,255,256] Li and coworkers designed Pd@Ag core–shell NPs inside UiO-67 *via* a seed-mediated growth strategy, in which activated hydrogen atoms on embedded Pd NPs can act as a reducing agent to selectively direct the deposition of Ag onto Pd while minimizing Ag self-nucleation.[180] The obtained Pd@Ag@UiO-67 composites exhibited a significant increase in selectivity in the partial hydrogenation of phenylacetylene as compared to their monometallic counterparts, due to the surface dilution and electron modification of the surface Pd sites by Ag deposition. Although the role of the MOF in hydrogen enrichment was not mentioned in the report, we assume that this effect might exist and thus speed up the reaction process to some extent. Moreover, Pd@Ag@UiO-67 possessed high stability and recyclability in the catalytic reactions, which was

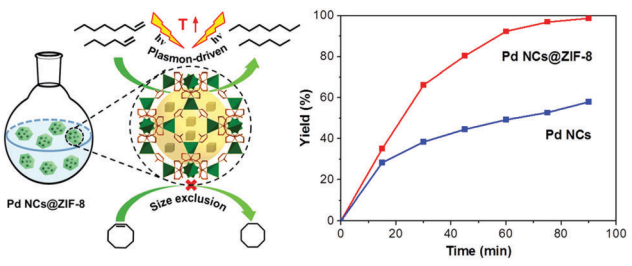


Fig. 20 The Pd NCs@ZIF-8 for plasmon-driven selective catalysis of the hydrogenation of olefins (left) and hydrogenation yield of 1-hexene over Pd NCs or Pd NCs@ZIF-8 along with reaction time (right). Reproduced from ref. 81 with permission from Wiley-VCH, copyright 2016.

related to the nanoconfinement effect and the strong metal–support interaction offered by the UiO-67 framework.

Liu *et al.* employed Ag@MIL-101 to catalyze the conversion of terminal alkynes into propiolic acids with $CO_2$.[257] Given the excellent catalytic activity of Ag@MIL-101, the reaction can be completed at atmospheric pressure and low temperature. Apparently, in the Ag@MIL-101 catalyst, MIL-101 is able to enrich $CO_2$ molecules around Ag NPs, which behave as active centers to further catalyze the $CO_2$ addition with alkynes. A series of alkyne compounds were transformed to the corresponding propiolic acids with high yields.

Cao's group demonstrated a facile synthetic strategy *via* introducing MNPs for subsequent MOF growth to form ZIF-8-encapsulated PtPd NPs with tunable compositions, denoted as PtPd@ZIF-8, for oxidative degradation of ethylene—an effective method to remove low concentrations of ethylene.[258] ZIF-8 not only served as a stabilizer to prevent the aggregation of the alloy NPs, but might also adsorb ethylene around the active sites. Due to the synergistic functions between PtPd and MOF, the PtPd@ZIF-8 catalyst showed excellent photocatalytic activity in the transformation of adsorbed ethylene into $CO_2$ and $H_2O$ at room temperature.

It is noteworthy that the gas enrichment behavior of MOFs in a real reaction solution might be different from the results of measured gas sorption with activated MOF samples under vacuum. Given that the gas enrichment capacity of MOFs is usually limited at elevated temperatures, MNPs@MOF composites might have no or very weak gas enrichment capacity during the catalytic process at high temperatures. Although these reactions involve gas reactants, they will not be discussed here in detail.[133,148,151,188,259,260]

### 5.4. MNPs as active centers, with MOFs stabilizing MNPs and regulating their electronic properties

The properties of catalytically active centers are closely related to their surrounding chemical environment. Given the highly tunable character of MOF structures, the tailored functional groups dangling on the ligands/metal clusters can regulate electronic properties at an atomic level. Ligands with diverse functional groups give different interactions with MNPs, thus leading to a change in the catalytic activity and selectivity of the MNPs.[261,262] Post-synthetically grafting additional groups onto metal clusters in the MOF host was also reported to improve the activity and selectivity of encapsulated MNPs.[263] Particularly, on the basis of the semiconductor-like behaviour of MOFs, alterations in the intensity of light irradiation can affect the direction of electron transfer between the MOF and MNPs and thus change the electronic state of the MNPs and the catalytic activity.[83] Related reports, although very limited, perfectly reflect the structural advantages of MOFs and the importance of optimizing the catalytic efficiency of MNPs. The mechanism for the regulation of electronic properties along with the reported results will be discussed in detail.

Recently, Huang's group demonstrated that the catalytic properties of Pd NPs can be controlled through changes in the chemical environments in pore walls in isoreticular MOFs.[262] Pd NPs were stabilized in an atomically tunable chemical environment by UiO-66-type structures to give Pd/MOFs (denoted as Pd@UiO-66-X, X = H, $NH_2$, and OMe) for the aerobic reaction between benzaldehyde and ethylene glycol. Notably, the reaction between benzaldehyde and ethylene glycol has two reaction pathways: (1) benzaldehyde condensation with ethylene glycol to give the hemiacetal and (2) further condensation to obtain the acetal or oxidation to the ester. For Pd@UiO-66-$NH_2$, the selectivity to benzaldehyde ethylene acetal reached 94%, while both Pd@UiO-66 and Pd@UiO-66-OMe exhibited high selectivity (90% and 97%, respectively) to the ester 2-hydroxyethyl benzoate (Fig. 21). It seems that the product selectivity can be completely changed from an acetal to an ester by varying the functional group from $-NH_2$ to –H/–OMe on the organic linkers in UiO-66-X. Diffuse reflectance infrared fourier transformation spectroscopy (DRIFTS) indicated that the interaction between $-NH_2$ and Pd NPs in Pd/UiO-66-$NH_2$ affected the electron density of Pd NPs and reactant adsorption. To gain a deeper understanding of the influence of different functional groups on the oxidation capability of Pd NPs, density functional theory (DFT) calculations were conducted to show that increased chemical potential will impair the oxidation properties of Pd NPs and UiO-66-$NH_2$, resulting in a greater increase in the chemical potential in comparison to the UiO-66-OMe. Thus, Pd@UiO-66-$NH_2$ with relatively weak oxidation properties can impede the withdrawal of electrons from reactants, thus hindering the generation of esters and leading to high acetal selectivity. In contrast, the moderate oxidation capability of the Pd@UiO-66-OMe composite resulted in higher catalytic activity toward ester formation.

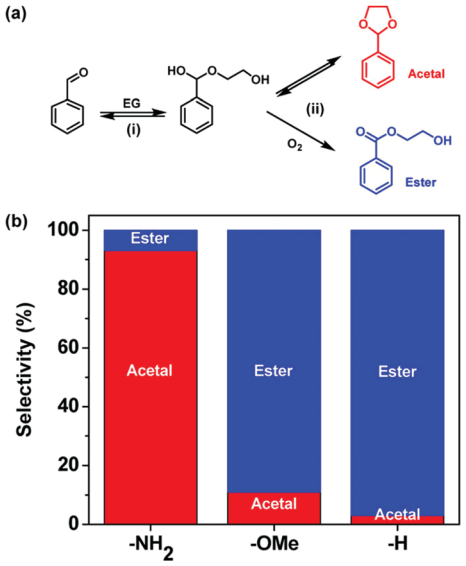


Fig. 21 (a) Possible pathways of aerobic reaction between benzaldehyde and ethylene glycol and (b) product distribution using Pd@UiO-66-X (X = H, $NH_2$, OMe) catalysts. Reproduced from ref. 262 with permission from the American Chemical Society, copyright 2016.

Zhao *et al.* reported that the strong interfacial electron-transfer effect between MNPs and MOFs played crucial roles in the resultant catalytic selectivity.[172] A series of sandwich-like structures were successfully fabricated by the step-by-step synthesis strategy, including two Fe-MIL-101@Pt@Fe-MIL-101

 

structures with shell thicknesses of about 9.2 nm (1) and 22.0 nm (2), one Cr-MIL-101@Pt@Cr-MIL-101 structure with a shell thickness of about 5.1 nm (3), two Cr-MIL-101@Pt@Fe-MIL-101 structures with shell thicknesses of about 2.8 nm (4) and 8.8 nm (5), and some controlled catalysts, for selective hydrogenation of cinnamaldehyde to cinnamyl alcohol. There was no noticeable conversion of cinnamaldehyde over MIL-101, while Pt NPs efficiently catalyzed this reaction, although the selectivity to cinnamyl alcohol was only ~18.3%. Fortunately, the Pt/MIL-101 composite showed remarkably increased selectivity to cinnamyl alcohol, with 86.4% for Pt/Fe-MIL-101 and 44.0% for Pt/Cr-MIL-101. The dramatic promotion of the selective hydrogenation of the C=O bond in the presence of MIL-101 might be due to Lewis acid sites from the CUSs in MIL-101, which could interact with the C=O bonds and activate them. A Fourier transform infrared (FTIR) survey indicated the selective interaction between the C=O bond of cinnamaldehyde and MIL-101, evidenced by an obvious red shift of $\nu_{C=O}$ while $\nu_{C=C}$ for cinnamaldehyde was unchanged after mixing with MIL-101. The sandwich-like MIL-101@Pt@MIL-101 for selective hydrogenation of cinnamaldehyde to cinnamyl alcohol was further explored. Notably, the selectivity to cinnamyl alcohol was further improved: the selectivity for Cr-MIL-101@Pt@Cr-MIL-101 was 79.2%, while for the catalysts coated with an Fe-MIL-101 shell, the selectivity was always higher than 94%. XPS measurements suggested a partial transfer of electrons from Pt NPs to Fe-MIL-101, whereas electron transfer between Pt NPs and Cr-MIL-101 was absent, which explains the above selectivity difference between the Cr-MIL-101 and Fe-MIL-101 shells. The interfacial electron-transfer effect between the Pt NPs and Fe-MIL-101 is responsible for the excellent selectivity to cinnamyl alcohol based on MIL-101@Pt@Fe-MIL-101 catalysts. This work elegantly illustrates the synergistic functions of the Pt active centers and MOF stabilizer as well as the electron interaction between them.

Most recently, Jiang's group have observed an interesting electron transfer between MNPs and porphyrinic MOFs, PCN-224(M), which regulates the electronic state of the Pt surface and thus the catalytic efficiency of alcohol oxidation by changing the intensity of light irradiation.[83] The Pt NCs were stabilized by PCN-224(M) to give Pt/PCN-224(M) composites, which combine the advantages of both Pt NCs and PCN-224(M); these lie in the photothermal effect and $^1O_2$ production ability of both components and result in excellent activity and selectivity in the light-assisted catalytic oxidation of primary alcohols to aldehydes *via* a $^1O_2$-engaged oxidation process using $O_2$ under mild conditions. Particularly, the electron transfer between Pt NCs and PCN-224(Zn), as the optimized MOF, was further studied by transient photocurrent measurements for Pt NCs, PCN-224(Zn), and Pt/PCN-224(Zn). The current densities of Pt NCs and PCN-224(Zn) were positively correlated with light intensity from 60 to 120 mW cm$^{-2}$, while the current densities of Pt/PCN-224(Zn) initially increased with increasing light intensity up to 100 mW cm$^{-2}$ but then decreased when the light intensity was further increased. These results were in accord with the trend obtained from the reaction yield *vs.* light intensity, indicating improved charge separation in Pt/PCN-224(Zn),

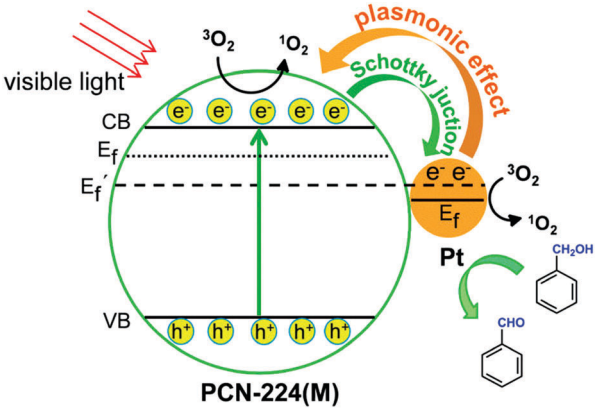


Fig. 22 Proposed mechanism for the $^1O_2$ generation and electron transfer between Pt and PCN-224(M) in the oxidation of benzyl alcohol over Pt/PCN-224(M) under visible-light irradiation. Reproduced from ref. 83 with permission from the American Chemical Society, copyright 2017.

driven by the Schottky barrier at a relatively low light intensity (<100 mW cm$^{-2}$) and the reverse injection of energetic hot electrons from plasmonic Pt NCs to reach the noble metal/semiconductor interface and enter the LUMO of PCN-224(Zn) at high light intensity over 100 mW cm$^{-2}$ (Fig. 22). That is, the light intensity change greatly affects the electron transfer between Pt and PCN-224(Zn) and regulates the electronic state/density of the Pt surface, which further controls the $^1O_2$ generation and the catalytic efficiency. Apparently, the functions of Pt and PCN-224(M) have been highly synergized in this work to achieve optimized catalysis.

### 5.5. MNPs as electron acceptors and active centers, with MOFs as photosensitizers and stabilizers

Along with studies of gradually increasing depth, more functions of MOFs have been explored. In addition to the widespread attention to catalysis in the common organic reactions described above, MNP/MOF composites are demonstrated to be important in the research field of photocatalysis. With particular organic linkers, MOFs are responsive toward UV and even a broad range of visible light, making them suitable as photosensitizers.[108–111,149,264–266] The MNPs stabilized by MOFs usually behave as excellent electron acceptors and active centers, which accept electrons from excited MOFs, and the photocatalytic reactions can be effectively promoted by the integration of the functionalities of both MOFs and MNPs.

Lin and coworkers prepared a photoactive UiO-type MOF, based on an $[Ir^{III}(ppy)_2(bpy)]^+$-derived dicarboxylate linker and $Zr_6(\mu_3\text{-}O)_4(\mu_3\text{-}OH)_4(carboxylate)_{12}$ SBUs, in which Pt NPs were *in situ* generated by the photoreduction of $K_2PtCl_4$.[109] The resultant Pt@MOF composite was efficient for photocatalytic hydrogen evolution from water using visible light (>420 nm), with the highest hydrogen evolution turnover number (TON) for Ir phosphors (Ir-TON) of 1620 in 6 h, showing a high photochemical quantum yield. The catalyst can be recovered from the solution by centrifugation after the reaction and used again for hydrogen evolution in a fresh solution without additional $K_2PtCl_4$. The Ir-TONs of the recovered catalysts could be

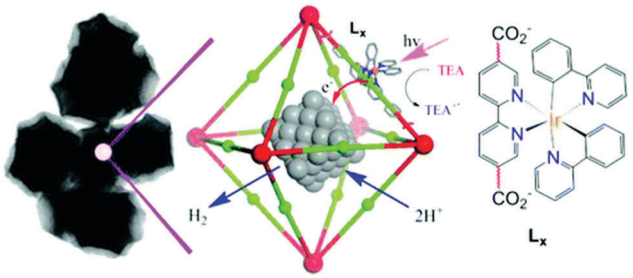


Fig. 23 Scheme showing synergistic photocatalytic hydrogen evolution *via* injection of electrons from the light-harvesting MOF into Pt NPs. Reproduced from ref. 109 with permission from the American Chemical Society, copyright 2012.

maintained at the same level and the catalyst could be recycled at least three times. Control experiments without addition of the MOF or $K_2PtCl_4$ to the solution were operated under the same conditions, but no hydrogen evolution from water was detected, clearly demonstrating the synergistic function of both species. From the contrast experiments, the authors believed that the synergistic photocatalytic hydrogen evolution took place *via* the process of photoinjection of electrons from the light-harvesting MOF into the Pt NPs. The $[Ir^{III}(ppy)_2(bpy^{\bullet -})]$ radicals generated by TEA-mediated photoreduction can transfer electrons to Pt NPs to reduce protons for hydrogen production (Fig. 23).

Shen *et al.* demonstrated a facile and general method to fabricate highly dispersed MNPs/Ti-MIL-125 (MNPs = Au, Pd, and Pt) based on an *in situ* redox reaction for the photocatalytic oxidation of benzyl alcohol.[108] Compared with pristine Ti-MIL-125, the conversion with MNPs/Ti-MIL-125 was improved and a high selectivity to aldehyde was maintained. The photocatalytic degradation of RhB over MNPs/Ti-MIL-125 was also much more efficient than with blank Ti-MIL-125. The enhanced activity of MNPs/Ti-MIL-125 was ascribed to the presence of a Schottky barrier between the MNPs and Ti-MIL-125 and photoelectron transfer from Ti-MIL-125 with a low work function to MNPs with a high work function because of their intimate interfacial contact, which significantly improved the separation and lifetime of photogenerated carriers. Moreover, a series of MNPs@Fe-MIL-100 composites with highly dispersed noble metal NPs (Au, Pd, Pt) were synthesized *via* a photodeposition technique for enhanced activity toward the photocatalytic degradation of methyl orange (MO) and the reduction of heavy-metal Cr(VI) ions under visible-light irradiation ($\lambda \geq 420$ nm), in reference to pristine Fe-MIL-100.[111] The enhanced photoactivity strongly relies on the MNPs acting as electron reservoirs, which improves the separation and lifetime of charge carriers that are photogenerated by the MOF photosensitizer.

In a recent study, Xiao *et al.* investigated the efficiency of electron–hole separation and charge-carrier utilization for photocatalysis in a system of MNPs/MOFs.[149] The authors deliberately synthesized two types of composites: Pt NPs of *ca.* 3 nm were incorporated inside or supported on a representative MOF, UiO-66-$NH_2$, to afford Pt@UiO-66-$NH_2$ and Pt/UiO-66-$NH_2$, respectively, for photocatalytic hydrogen production *via* water splitting. Compared with the pristine MOF, both Pt-decorated MOF composites displayed remarkably improved but distinctly different hydrogen-production activities. In order to determine the charge-separation efficiency, photocurrent measurements were carried out and the results showed that the photocurrents for both Pt-decorated UiO-66-$NH_2$ composites were enhanced as compared to the pristine UiO-66-$NH_2$, indicating that the formation of a Pt-MOF Schottky junction was useful for separating the photogenerated electron–hole pairs. Pt@UiO-66-$NH_2$ displays an even stronger photocurrent response than Pt/UiO-66-$NH_2$, sugggesting a higher efficiency of charge transfer from the MOF to the Pt NPs in the former. This argument was also supported by the electrochemical impedance spectroscopy (EIS) results, where Pt@UiO-66-$NH_2$ showed a smaller radius, indicating a lower charge-transfer resistance. Photoluminescence (PL) emission spectroscopy further verified this conclusion: the PL of UiO-66-$NH_2$ was slightly weakened for Pt/MOF but greatly suppressed for Pt@MOF. Furthermore, ultrafast transient absorption spectroscopy disclosed the underlying electron-transfer mechanism and showed that more efficient charge separation was achieved in Pt@MOF than in Pt/MOF and pure MOF. All these results demonstrated that, compared to MOF and Pt/MOF, the electron–hole recombination was more effectively suppressed by Pt@MOF, in which the photogenerated electrons of the MOF can be rapidly extracted by the well encapsulated Pt NPs (with short electron transport distances from MOF to Pt), thus resulting in the far superior catalytic activity of Pt@UiO-66-$NH_2$ compared to that of Pt/UiO-66-$NH_2$ and UiO-66-$NH_2$.

### 5.6. Both MOFs and MNPs as active sites for tandem catalysis

In the studies of functional synergy between MNPs and MOFs described above, although the resultant catalytic performance is excellent, the catalytic activity almost comes from MNPs and MOF rarely exhibits their catalytic behavior, which is obviously a pity. It is highly desirable to judiciously integrate the MOF catalysis and MNP catalysis toward one-pot multistep tandem reactions. Several studies have successfully realized this exciting target, in which both MOFs and MNPs, as active sites, exert their respective functions and cooperatively catalyze cascade reactions. The catalytic effect of each component in MNP/MOF composites toward the cascade reactions will be thoroughly discussed.

Tang's group fabricated a core–shell structured Pd@IRMOF-3 catalyst, consisting of a Pd NP ($\sim$35 nm) core and an amino-functionalized IRMOF-3 shell for a cascade reaction, including the Knoevenagel condensation of 4-nitrobenzaldehyde (A) and malononitrile to 2-(4-nitrobenzylidene)malononitrile (B), which was catalyzed by the basic amino group in the IRMOF-3 shell, followed by selective hydrogenation of the nitro group to an amino product (C), catalyzed by Pd NPs (Fig. 24).[146] Due to a combination of factors including selective sorption, a constant diffusion direction, and suitable pore sizes, the core–shell Pd@IRMOF-3 catalyst exhibited better hydrogenation selectivity and stability than a catalyst of Pd NPs loaded on IRMOF-3. The amino groups on the surface of IRMOF-3 exhibited a preferential interaction with the nitro group of the substrates. When the core–shell Pd@IRMOF-3 composite is employed as the catalyst,

 

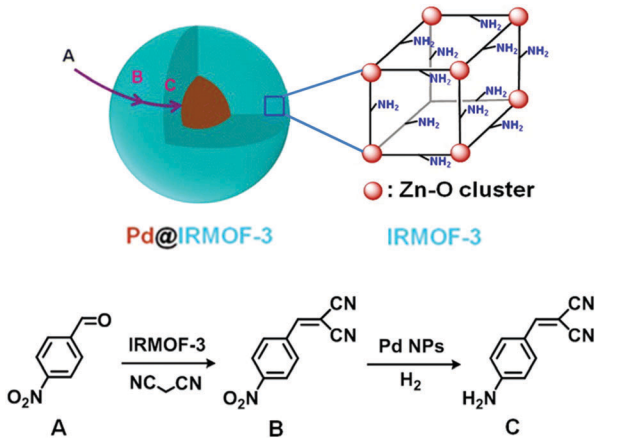


Fig. 24 Tandem reaction involving Knoevenagel condensation of A with malononitrile, catalysed by the IRMOF-3 shell, and subsequent selective hydrogenation of intermediate B to C, catalyzed by the Pd NP cores. Reproduced from ref. 146 with permission from the American Chemical Society, copyright 2014.

A preferentially enters the catalyst behind the $-NO_2$ group. After entering, the limited pore size of the core–shell nanostructures becomes another important factor in the control of the selectivity to C. Due to the large size of B and the small $-NO_2$ group, B must keep a constant direction behind the $-NO_2$ group inside the IRMOF-3 channels, leading to the selective generation of C instead of the other possible hydrogenation products, 2-(4-nitrobenzyl)malononitrile or 2-(4-aminobenzyl)malononitrile.

In addition, Huang and colleagues employed Pd@UiO-66-$NH_2$ for a one-pot tandem oxidation-acetalization reaction.[181] Combining the oxidation activity of Pd NPs and the acetalization activity of Lewis acid sites in UiO-66-$NH_2$, Pd@UiO-66-$NH_2$ exhibited excellent catalytic activity and selectivity. In this study, benzyl alcohol was firstly oxidized to benzaldehyde by Pd NPs, followed by benzaldehyde acetalization with ethylene glycol over Lewis acid sites in UiO-66-$NH_2$, resulting in 99.9% selectivity to benzaldehyde ethylene acetal and 99.9% conversion of benzyl alcohol. The authors also examined various substituted benzyl alcohols and found that alcohols with electron-donating groups showed better conversion and selectivity compared to those with electron-withdrawing groups. No leaching of Pd NPs occurred during the reaction and the catalyst could be reused at least five times without significant deactivation.

To take one step further than simply combining the single functions of both the host MOF and guest MNPs, Chen *et al.* synthesized monometallic and bimetallic NPs@MOF catalysts, featuring tiny metal NPs inside MIL-101 cages, for a one-pot multistep selective reaction.[82] The Pd@MOF cooperatively catalyzed a tandem reaction on the basis of both the MOF Lewis acidity and Pd sites. Strikingly, the bimetallic PdAg@MOF composite involving three active sites (Lewis acid, Pd, and Ag) was able to successfully realize a one-pot multistep cascade reaction in the synthesis of secondary arylamines, by not only perfect cooperation between the MOF host and the metal NP guest but also synergistic catalysis between the bimetallic Pd and Ag species, in which the MOF affords Lewis acid sites, Pd

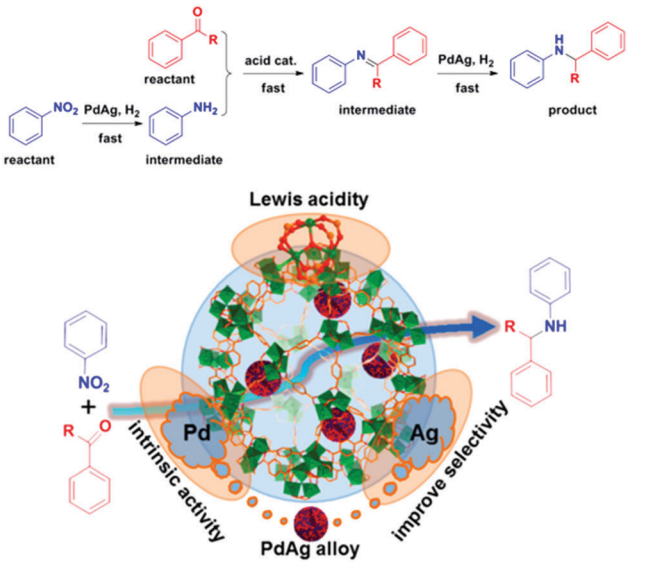


Fig. 25 (upper) Multi-step synthesis of secondary arylamine *via* cascade reactions. (below) Schematic illustration showing the one-pot cascade reactions over PdAg@MIL-101 achieved by synergizing the functions of the three components. Reproduced from ref. 82 with permission from the American Chemical Society, copyright 2015.

offers hydrogenation activity, and Ag greatly improves the selectivity toward the desired product (Fig. 25). Moreover, the ideal confinement effect of MIL-101 results in ultrafine PdAg alloy NPs of ~1.5 nm, which are possibly the smallest bimetallic NPs in the presence of surfactant protection, and the MNP sizes are maintained even after three cycles, highlighting the stabilization capability of the MOF. This work demonstrated a MOF host and the two species in a bimetallic NP guest functioning as "three legs of a tripod" in catalysis, which cooperatively boosted one-pot multistep cascade reactions. The authors claim that this is the first report on catalytic cooperation between a MOF host and guest MNPs together with synergistic catalysis of bimetallic NPs.

Colloidal deposition of Au NPs onto UiO-66-$NH_2$ was also demonstrated with the resulting hybrid catalyst being used for one-pot and heterogeneous selective oxidation of primary alcohols in tandem with Knoevenagel condensation reactions.[267] The Au NPs were the active sites for the selective oxidation of alcohols to aldehydes, while the functional amine groups in the framework of UiO-66-$NH_2$ offered nucleophilic or basic sites to catalyze the condensation step. Similarly, an Au@Cu(II)-MOF nanohybrid with good Au dispersion was synthesized *via* solution impregnation and exhibited a bifunctional heterogeneous catalytic nature to catalyze benzyl alcohol oxidation and Knoevenagel condensation reactions in a successive manner.[268] The same group prepared another solid catalyst, Pd@UiO-68-AP, *via* a chelation-directed post-synthetic approach and subsequent reduction. By synergistically combining the aerobic oxidation activity of the encapsulated Pd NPs and Knoevenagel condensation activity of the Zr-Lewis acid sites, the obtained Pd@UiO-68-AP could promote benzyl alcohol oxidation-Knoevenagel condensation in a stepwise way.[198]

## 6. Synergistic effect between MOFs and other guest species for enhanced catalysis

There is infinite potential to functionalize the pore space in MOFs, where a variety of guest species can be located, not just MNPs. There have been a variety of functional species coupled with MOFs for enhanced catalysis, including metal oxides,[269–273] enzymes,[274–279] quantum dots,[280,281] and polyoxometalates (POMs).[282–289] The synthetic approaches and the improved catalysis based on the synergistic effect of a combination of different functions of MOFs and these guest species are similar to those of the MNP/MOF composites described in this review. For example, Li *et al.* fabricated a HKUST-1@$TiO_2$ core–shell structure for photocatalytic $CO_2$ reduction with $TiO_2$ as a photocatalytic active site for conversion of $CO_2$ to $CH_4$ (with the aid of $H_2O$), while HKUST-1 acted as an excellent material for $CO_2$ enrichment. The ultrafast spectroscopy data indicated that the photogenerated electrons can be effectively transferred from $TiO_2$ to the MOF, which not only facilitated charge separation in $TiO_2$ but also offered energetic electrons to the $CO_2$ adsorbed on the MOF. $CO_2$ can be reduced to $CH_4$ with a dramatically improved performance in both activity and selectivity.[273] Moreover, Sun *et al.* synthesized a series of POMs@HKUST-1 composites based on $H_nXM_{12}O_{40}$ (X = Si, Ge, P, As; M = W, Mo) through one-pot hydrothermal reactions.[289] The $PW_{12}O_{40}$@HKUST-1 displayed good catalytic activity and size selectivity in the hydrolysis of esters in excess water, in which the conversion of methyl acetate (4.87 × 3.08 Å) and ethyl acetate (6.11 × 3.11 Å) reached 64% and 63% after 5 h, respectively. In contrast, the conversion of ethyl benzoate (8.96 × 4.65 Å) was reduced to below 20% under similar conditions. With a substrate with a further expanded molecular size, the conversion of 4-methyl-phenyl propionate (10.61 × 4.04 Å) was below 1% even after 24 h. Moreover, the catalyst could be recycled 15 times without activity loss or leaching. The work unambiguously presents the synergistic functions of the active POM guests and the size selectivity and stability effect endowed by the MOF. Given that the current review focuses on catalysis over MNP/MOF composites, the related studies on a variety of MOF-based composites have not been discussed in detail, although they are of great importance and are indispensable parts of the development of MOF application in catalysis. Reader who are interested in these might refer to a recent review.[41]

## 7. Conclusions and perspectives

Considering the important features of MOFs and recent interest in exploiting their properties, MOFs undoubtedly possess important potential and advantages in catalysis and thus MOF catalysis has attracted much interest in recent years. However, the types of active sites on MOFs are usually limited to acid/base sites or metal centers built into organic linkers. The introduction of MNPs, applicable in catalysis for a broad scope of reactions, to MOFs as guest active sites to afford composite materials, in which each component exerts respective functions for enhanced catalysis, should be a judicious choice. Various synthetic strategies for incorporating MNPs in MOFs have been developed. Generally, the MNP/MOF composites introduced in this review can be classified according to four synthetic approaches: (1) MOFs are synthesized first, followed by the formation of MNPs inside and/or partially on the external surface of the MOF; (2) pre-synthesized MNPs are introduced into the reaction solution for subsequent MOF growth, generally, to obtain MNPs incorporated into the MOF; (3) stepwise synthesis of the MNPs/MOF and MOF/MNPs/MOF; (4) one-step synthesis of MNP/MOF composites. In the first approach, MOFs act as porous supports to accommodate MNPs. To introduce MNPs into pre-synthesized MOFs, five typical methods: solution impregnation, the double-solvent approach, chemical vapor deposition, solid grinding, and thermal decomposition have been adopted. These five methods are very useful for obtaining small NPs with clean surfaces, but the control of the size, shape, and composition of the resultant MNPs is relatively poor. In contrast, introducing MNPs as seeds and growing MOFs around them is a rational strategy and the size, shape, and composition of the MNPs are precontrolled. Moreover, the formation of core–shell or yolk–shell structured MNPs@MOFs is probable. Unfortunately, the MNP surface is usually coated, which is unfavorable for the complete exposure of active sites. The third approach seems complicated but has special advantages: the MOF core not only behaves as a support for MNPs but also induces subsequent growth of the MOF shell, which not only reinforces the MNPs for better stability but also offers size-selective catalysis. The fourth approach is the most direct for synthesizing MNP/MOF composites. It appears simple but usually requires specific atoms or functional groups in the organic linkers to trap the metal precursors.

By synergizing the functions of the MNPs and MOFs, expanded reaction scope and enhanced catalysis can be achieved through the MNP/MOF composites. Thus, it is necessary to recognize the roles of both components and understand how they synergize to achieve these ends. In this review, we summarized six synergistic combinations of MOFs and MNPs: (a) MNPs as active centers, stabilized by MOFs; (b) MNPs as active centers, with MOFs stabilizing MNPs and controlling size selectivity; (c) MNPs as active centers, with MOFs stabilizing MNPs and concentrating gaseous reactants; (d) MNPs as active centers, with MOFs stabilizing MNPs and regulating their electronic properties; (e) MNPs as electron acceptors and active centers, with MOFs as photosensitizers and stabilizers; (f) both MOFs and MNPs as active sites for tandem catalysis. In MNP/MOF systems, MNPs serve as active centers and MOFs behave as stabilizers for MNPs, which is the simplest synergy between MNPs and MOFs, and exists in almost all MNP/MOF catalysts, regardless of the other functions of both components. For core–shell or yolk–shell structured MNPs/MOFs, the uniform pore sizes of the MOFs allow the composites to function as molecular sieves. For catalytic reactions involving gas molecules at relatively low temperatures, MOFs can enrich the gas molecules around the active sites (MNPs) to a certain degree, thus boosting the catalytic activity. In addition, the performance of the MNPs is

 

closely related to their surrounding chemical environment. Given the tailorability of MOF structures, the alterable functional groups dangling on the ligands can regulate the electronic properties at an atomic level. The ligands with diverse functional groups interact differently with the MNPs, thus leading to a change in the catalytic activity and selectivity of the MNPs. Recently, MNP/MOF composites showed great potential in photocatalysis. Many MOFs are responsive toward UV and even a broad range of visible light, making them suitable as photosensitizers to transfer electrons to MNPs, resulting in excellent photocatalytic properties. In addition, given the multifunctional roles of both MOFs and MNPs, several MNP/MOF catalysts have shown the ability to promote one-pot multistep cascade reactions, which will save energy and costs in industry and are thus exciting.

Although dramatic advances, as summarized above, have been achieved over more than 10 years, this field is currently in its infancy and more effort should be dedicated to exploiting the future of MNPs/MOFs in catalysis. Some underdeveloped but anticipated issues based on MNPs/MOFs are indicated below.

Noble metal NPs, and even bimetallic NPs involving noble metals and base metals, show very promising catalysis by coupling with MOFs. The scarcity and high cost of noble metals are very realistic considerations. Moreover, many base metals have presented significant potential in catalyzing a wide range of organic reactions. The replacement of noble metal NPs with base metal NPs in MNPs/MOFs for catalysis should be considered, particularly from an industrial point of view.

The perfect MOF shell endows MNPs@MOF catalysts with excellent size-selective behavior in catalysis, due to the uniform pore size in the MOFs. Unfortunately, most related reports are based on the selectivity of the catalytic substrates, which is conceptually important but seldom useful in industry, as it is unnecessary to sieve substrates with different sizes in practical applications. An industrially more relevant outcome is the achievement of size selectivity for the products, that is, only products with specific molecular sizes are produced while other byproducts are avoided. This represents an important goal in the design of MNP/MOF-based catalysts.

Combinations of nanoparticulate composite catalysts, for example, MNPs/metal oxide and MNPs/graphene oxide, with MOFs will be more powerful catalysts. As the catalytic activity of MNPs is usually dependent on the nature of the support, the introduction of this special support and also MNP/support interactions to MOFs would improve the catalytic performance of MNPs. Meanwhile, as mentioned in this review, the multifunctionalities of MOFs can be synergized together with the MNPs/support for considerably enhanced catalysis.

The detailed structure of MNPs incorporated into MOFs is unclear, which impedes the clarification of structure–property relationships. If atomically precise metal clusters are encapsulated into MOFs, it would help to better understand the structure–catalysis relationship,[211] as both components would have well-defined structures. Moreover, theoretical calculations on a metal cluster@MOF with a precise structure would be more reliable.

The highly tailorable pore environments in MOFs play vital roles in regulating the catalytic behavior of the encapsulated MNPs and have great potential in catalysis, which, despite the substantial number of reports that have appeared,[172,262,263] is far from being well developed. The functional groups dangling from the linkers are not only able to regulate the electronic state of the MNPs, regardless of the presence or absence of additional stimuli (for example, light irradiation),[83] but also enable a confined reaction space for optimized catalysis.

In almost all current reports on MNPs/MOFs, MNPs are limited to random arrangements, although the encapsulation in and on the external surface of an MOF can be rationally controlled. Ordered/periodic arrays of MNPs would significantly benefit their properties due to the intrinsic interactions between the MNPs. Therefore, it would be desirable to realize spatial arrangements of MNPs, with their size, shape and location being well controlled inside the MOFs, which will offer unique properties.

Last but not least, progress in the field of MNP/MOFs cannot be independent of research on MOFs. The development of highly stable MOFs with hierarchical pores and tailorable pore environments is very important, as stability guarantees catalytic recyclability; large pore sizes eliminate mass transfer limitations and pore wall environments will tailor the electronic properties of MNPs. Large-scale synthetic methods to afford low-cost MOFs are also necessary for practical applications. In addition, several studies on MNPs/MOFs are thus far based on probe reactions to conceptually explain the superiority of the catalysts. In the future, we would seek interdisciplinary views to exploit more important reactions in industry using MNP/MOF catalysts. With persistent efforts toward these challenges, we have every reason to believe that MNP/MOF catalysis has a very bright future.

## List of acronyms and abbreviations

| | |
|---|---|
| ATB | Aniline-2,4,6-tribenzoate |
| BDC | 1,4-Benzenedicarboxylate |
| BDC-$NH_2$ | 2-Aminoterephthalate |
| BDC-$SO_3H$ | 2-Sulfoterephthalate |
| BPDC | Biphenyl-4,4′-dicarboxylate |
| BPTC | 1,1′-Biphenyl-2,2′,6,6′-tetracarboxylate |
| BPY | 4,4′-Bipyridine |
| BPYDC | 2,2′-Bipyridine-5,5′-dicarboxylate |
| BTB | 1,3,5-Benzenetribenzoate |
| BTC | Benzenetricarboxylate |
| CD | Cyclodextrin |
| CTAB | Cetyltrimethylammonium bromide |
| Cyclam | 1,4,8,1-Tetraazacyclotetradecane |
| DOBDC | 2,5-Dihydroxyterephthalate |
| DPB | 1,4-Di(pyridin-4-yl)benzene |
| L | 4,4′-(Hexafluoroisopropylidene)-diphthalate |
| MeIM | 2-Methylimidazole |
| MIM | 4-Methyl-5-imidazolecarboxaldehyde |
| 1,4-NDC | Naphthalenedicarboxylate |
| OBB | 4,4′-Oxybis(benzoate) |
| PDMS | Polydimethylsiloxane |

| | |
|---|---|
| PIP | 5-(Prop-2-yn-1-yloxy)isophthalate |
| PVP | Polyvinylpyrrolidone |
| PYZ | Pyrazine |
| PZDC | Pyrazine-2,3-dicarboxylate |
| TPDC | [1,1′:4′,1″-Terphenyl]-4,4″-dicarboxylate |
| TATB | Triazine-1,3,5-tribenzoate |
| TCPP | Tetrakis(4-carboxyphenyl)porphyrin |
| Al-based MOF | $[Al(OH)(1,4\text{-NDC})]_n$ |
| Al-MIL-53 | $[Al(OH)(BDC)]_n$ |
| Al-MIL-100 | $Al_3O(OH)(H_2O)_2[BTC]_2\cdot nH_2O$ |
| Al-MIL-101-$NH_2$ | $[Al_3O(OH)(H_2O)_2(BDC\text{-}NH_2)_3]\cdot nH_2O$ |
| BIF-20 | $Zn_2(BH(MeIM)_3)_2(OBB)$ |
| Cd-MOF | $Cd_2(L)(H_2O)\cdot 0.5H_2O$ |
| CPL-1 | $[Cu_2(PZDC)_2(PYZ)]_n$ |
| CPL-2 | $[Cu_2(PZDC)_2(BPY)]_n$ |
| Cu-MOF-74 | $Cu_2(dobdc)(H_2O)_2\cdot 8H_2O$ |
| Fe-MIL-88B-$NH_2$ | $Fe_3O(solvent)_3Cl(BDC\text{-}NH_2)_3(solvent)_m$ |
| Fe-MIL-100 | $Fe_3O(OH)(H_2O)_2[BTC]_2\cdot nH_2O$ |
| Fe-MIL-101 | $[Fe_3(OH)(H_2O)_2O(BDC)_3]\cdot nH_2O$ |
| HKUST-1 | $Cu_3(BTC)_2$ |
| IRMOF-3 | $Zn_4O(ATA)_3$ |
| La-BTC | $[La(1,3,5\text{-BTC})\cdot 6(H_2O)]$ |
| MesMOF-1 | $Tb_{16}(TATB)_{16}$ |
| MIL-53-$NH_2$ | $[M(OH)(BDC\text{-}NH_2)]_n$, M = Al or Fe |
| MIL-68 | M(OH)(BDC), M = Ga or In |
| MIL-88B-$NH_2$ | $Cr_3O(solvent)_3F(BDC\text{-}NH_2)_3(solvent)_m$ |
| MIL-100 | $Cr_3F(H_2O)_3O[BTC]_2\cdot nH_2O$, $n \sim 28$ |
| MIL-101 | $[Cr_3F(H_2O)_2O(BDC)_3]\cdot nH_2O$, $n \sim 25$ |
| MIL-101-$NH_2$ | $[Cr_3F(H_2O)_2O(BDC\text{-}NH_2)_3]\cdot nH_2O$ |
| MIL-101-$SO_3H$ | $[Cr_3F(H_2O)_2O(BDC\text{-}SO_3H)_3]\cdot nH_2O$ |
| MOF-5 | $[Zn_4O(BDC)_3]$ |
| MOF-177 | $Zn_4O(BTB)_2$ |
| MOF-508 | $[Zn(bdc)(4,4'\text{-bipyridine})_{0.5}]$ |
| MOF-545 | $Zr_6(H_2O)_8O_8(C_{48}N_4O_8H_{26})_2$ |
| Ni-MOF-74 | $Ni_2(dobdc)(H_2O)_2\cdot 8H_2O$ |
| Ni-MOFs | $\{[Ni(cyclam)]_2[BPTC]\}_n\cdot 2nH_2O$ |
| PCN-224(Zn) | $Zr_6O_4(OH)_8(Zn\text{-}TCPP)_2$ |
| SIM-1 | $Zn(C_{10}H_{10}N_4O_2)$ |
| SNU-90 | $Zn_4O(ATB)_2\cdot 22DMF\cdot 9H_2O$ |
| Ti-MIL-125 | $Ti_8O_8(OH)_4(BDC)_6$ |
| Ti-MIL-125-$NH_2$ | $Ti_8O_8(OH)_4(BDC\text{-}NH_2)_6$ |
| UiO-66 | $[Zr_6O_4(OH)_4(BDC)_6]$ |
| UiO-66-$NH_2$ | $Zr_6O_4(OH)_4(BDC\text{-}NH_2)_6$ |
| UiO-67 | $[Zr_6O_4(OH)_4(BPDC)_6]$ |
| UiO-68 | $[Zr_6O_4(OH)_4(TPDC)_6]$ |
| ZIF-8 | $Zn(MeIM)_2$ |
| Zn/Ni-MOF-2 | $Ni_{5.9}Zn_{3.3}C_{32}H_{36}O_{22}N_{0.6}$ |
| MNPs/MOFs | MNPs are loaded into and/or on the surface of MOFs |
| MNPs@MOFs | MNPs are only incorporated into MOFs |

## Acknowledgements

This work was supported by the NSFC (21371162, 21673213, and 21521001), the National Research Fund for Fundamental Key Project (2014CB931803) and the Recruitment Program of Global Youth Experts. Q. X. thanks METI, JSPS, and JST for financial support.

## References

1 J. R. Long and O. M. Yaghi, *Chem. Soc. Rev.*, 2009, **38**, 1213–1214.
2 H.-C. Zhou, J. R. Long and O. M. Yaghi, *Chem. Rev.*, 2012, **112**, 673–674.
3 H.-C. Zhou and S. Kitagawa, *Chem. Soc. Rev.*, 2014, **43**, 5415–5418.
4 M. Eddaoudi, D. B. Moler, H. Li, B. Chen, T. M. Reineke, M. O'Keeffe and O. M. Yaghi, *Acc. Chem. Res.*, 2001, **34**, 319–330.
5 B. Moulton and M. J. Zaworotko, *Chem. Rev.*, 2001, **101**, 1629–1658.
6 G. Férey, C. Mellot-Draznieks, C. Serre and F. Millange, *Acc. Chem. Res.*, 2005, **38**, 217–225.
7 R. J. Hill, D.-L. Long, N. R. Champness, P. Hubberstey and M. Schröder, *Acc. Chem. Res.*, 2005, **38**, 335–348.
8 S. T. Meek, J. A. Greathouse and M. D. Allendorf, *Adv. Mater.*, 2011, **23**, 249–267.
9 S. Qiu and G. Zhu, *Coord. Chem. Rev.*, 2009, **253**, 2891–2911.
10 W. Lu, Z. Wei, Z.-Y. Gu, T.-F. Liu, J. Park, J. Park, J. Tian, M. Zhang, Q. Zhang, T. Gentle III, M. Bosch and H.-C. Zhou, *Chem. Soc. Rev.*, 2014, **43**, 5561–5593.
11 J. S. Seo, D. Whang, H. Lee, S. I. Jun, J. Oh, Y. J. Jeon and K. Kim, *Nature*, 2000, **404**, 982–986.
12 T. Li, M. T. Kozlowski, E. A. Doud, M. N. Blakely and N. L. Rosi, *J. Am. Chem. Soc.*, 2013, **135**, 11688–11691.
13 H. Kitagawa, *Nat. Chem.*, 2009, **1**, 689–690.
14 S. Kitagawa, R. Kitaura and S. Noro, *Angew. Chem., Int. Ed.*, 2004, **43**, 2334–2375.
15 B. Chen, S. Xiang and G. Qian, *Acc. Chem. Res.*, 2010, **43**, 1115–1124.
16 A. Corma, H. García and F. X. Llabrés i Xamena, *Chem. Rev.*, 2010, **110**, 4606–4655.
17 S. Ma and H.-C. Zhou, *Chem. Commun.*, 2010, **46**, 44–53.
18 H.-L. Jiang and Q. Xu, *Chem. Commun.*, 2011, **47**, 3351–3370.
19 Z.-G. Gu, C. Zhan, J. Zhang and X. Bu, *Chem. Soc. Rev.*, 2016, **45**, 3122–3144.
20 P. Horcajada, R. Gref, T. Baati, P. K. Allan, G. Maurin, P. Couvreur, G. Férey, R. E. Morris and C. Serre, *Chem. Rev.*, 2012, **112**, 1232–1268.
21 A. J. Howarth, Y. Liu, P. Li, Z. Li, T. C. Wang, J. T. Hupp and O. K. Farha, *Nat. Rev. Mater.*, 2016, **1**, 15018.
22 J.-R. Li, J. Sculley and H.-C. Zhou, *Chem. Rev.*, 2012, **112**, 869–932.
23 M. P. Suh, H. J. Park, T. K. Prasad and D.-W. Lim, *Chem. Rev.*, 2012, **112**, 782–835.
24 K. Sumida, D. L. Rogow, J. A. Mason, T. M. McDonald, E. D. Bloch, Z. R. Herm, T.-H. Bae and J. R. Long, *Chem. Rev.*, 2012, **112**, 724–781.

 

25 A. Schneemann, V. Bon, I. Schwedler, I. Senkovska, S. Kaskel and R. A. Fischer, *Chem. Soc. Rev.*, 2014, **43**, 6062–6096.
26 L. Sun, M. G. Campbell and M. Dincă, *Angew. Chem., Int. Ed.*, 2016, **55**, 3566–3579.
27 H. Furukawa, K. E. Cordova, M. O'Keeffe and O. M. Yaghi, *Science*, 2013, **341**, 1230444.
28 J.-P. Zhang, Y.-B. Zhang, J.-B. Lin and X.-M. Chen, *Chem. Rev.*, 2012, **112**, 1001–1033.
29 I. Stassen, M. Styles, G. Grenci, H. V. Gorp, W. Vanderlinden, S. De. Feyter, P. Falcaro, D. De Vos, P. Vereecken and R. Ameloot, *Nat. Mater.*, 2016, **15**, 304–310.
30 P. Nugent, Y. Belmabkhout, S. D. Burd, A. J. Cairns, R. Luebke, K. Forrest, T. Pham, S. Ma, B. Space, L. Wojtas, M. Eddaoudi and M. J. Zaworotko, *Nature*, 2013, **495**, 80–84.
31 J. Gascon, A. Corma, F. Kapteijn and F. X. Llabrés i Xamena, *ACS Catal.*, 2014, **4**, 361–378.
32 A. Dhakshinamoorthy, A. M. Asiri and H. García, *Angew. Chem., Int. Ed.*, 2016, **55**, 5414–5445.
33 C. Wang, Z. Xie, K. E. deKrafft and W. Lin, *J. Am. Chem. Soc.*, 2011, **133**, 13445–13454.
34 Z. Zhang, Z.-Z. Yao, S. Xiang and B. Chen, *Energy Environ. Sci.*, 2014, **7**, 2868–2899.
35 Z. Hu, B. J. Deibert and J. Li, *Chem. Soc. Rev.*, 2014, **43**, 5815–5840.
36 J. Liu, L. Chen, H. Cui, J. Zhang, L. Zhang and C.-Y. Su, *Chem. Soc. Rev.*, 2014, **43**, 6011–6061.
37 P. Ramaswamy, N. E. Wong and G. K. H. Shimizu, *Chem. Soc. Rev.*, 2014, **43**, 5913–5932.
38 M. Zhang, G. Feng, Z. Song, Y.-P. Zhou, H.-Y. Chao, D. Yuan, T. T. Y. Tan, Z. Guo, Z. Hu, B. Z. Tang, B. Liu and D. Zhao, *J. Am. Chem. Soc.*, 2014, **136**, 7241–7244.
39 T. Zhang and W. Lin, *Chem. Soc. Rev.*, 2014, **43**, 5982–5993.
40 J. Lee, J. H. Kwak and W. Choe, *Nat. Commun.*, 2017, **8**, 14070.
41 Q.-L. Zhu and Q. Xu, *Chem. Soc. Rev.*, 2014, **43**, 5468–5512.
42 S. S. Nagarkar, B. Joarder, A. K. Chaudhari, S. Mukherjee and S. K. Ghosh, *Angew. Chem., Int. Ed.*, 2013, **52**, 2881–2885.
43 C. Jo, H. J. Lee and M. Oh, *Adv. Mater.*, 2011, **23**, 1716–1719.
44 B. Van de Voorde, B. Bueken, J. Denayer and D. De Vos, *Chem. Soc. Rev.*, 2014, **43**, 5766–5788.
45 L. Wang, Y. Han, X. Feng, J. Zhou, P. Qi and B. Wang, *Coord. Chem. Rev.*, 2016, **307**, 361–381.
46 P. Hu, J. V. Morabito and C.-K. Tsung, *ACS Catal.*, 2014, **4**, 4409–4419.
47 P. Falcaro, R. Ricco, A. Yazdi, I. Imaz, S. Furukawa, D. Maspoch, R. Ameloot, J. D. Evans and C. J. Doonan, *Coord. Chem. Rev.*, 2016, **307**, 237–254.
48 C. M. Doherty, D. Buso, A. J. Hill, S. Furukawa, S. Kitagawa and P. Falcaro, *Acc. Chem. Res.*, 2014, **47**, 396–405.
49 D. Farrusseng, S. Aguado and C. Pinel, *Angew. Chem., Int. Ed.*, 2009, **48**, 7502–7513.
50 Z. Wang and S. M. Cohen, *Chem. Soc. Rev.*, 2009, **38**, 1315–1329.
51 F. Vermoortele, B. Bueken, G. Le Bars, B. Van de Voorde, M. Vandichel, K. Houthoofd, A. Vimont, M. Daturi, M. Waroquier, V. Van Speybroeck, C. Kirschhock and D. E. De Vos, *J. Am. Chem. Soc.*, 2013, **135**, 11465–11468.
52 Z.-R. Jiang, H. Wang, Y. Hu, J. Lu and H.-L. Jiang, *ChemSusChem*, 2015, **8**, 878–885.
53 G. Akiyama, R. Matsuda, H. Sato, M. Takata and S. Kitagawa, *Adv. Mater.*, 2011, **23**, 3294–3297.
54 Y.-X. Zhou, Y.-Z. Chen, Y. Hu, G. Huang, S.-H. Yu and H.-L. Jiang, *Chem. – Eur. J.*, 2014, **20**, 14976–14980.
55 D. Feng, Z.-Y. Gu, J.-R. Li, H.-L. Jiang, Z. Wei and H.-C. Zhou, *Angew. Chem., Int. Ed.*, 2012, **51**, 10307–10310.
56 A. Dhakshinamoorthy, M. Alvaroa and H. García, *Chem. Commun.*, 2012, **48**, 11275–11288.
57 J. Lee, O. K. Farha, J. Roberts, K. A. Scheidt, S. T. Nguyen and J. T. Hupp, *Chem. Soc. Rev.*, 2009, **38**, 1450–1459.
58 A. H. Chughtai, N. Ahmad, H. A. Younus, A. Laypkov and F. Verpoort, *Chem. Soc. Rev.*, 2015, **44**, 6804–6849.
59 B. Li, M. Chrzanowski, Y. Zhang and S. Ma, *Coord. Chem. Rev.*, 2016, **307**, 106–129.
60 R.-Q. Zou, H. Sakurai, S. Han, R.-Q. Zhong and Q. Xu, *J. Am. Chem. Soc.*, 2007, **129**, 8402–8403.
61 S. Horike, M. Dincă, K. Tamaki and J. R. Long, *J. Am. Chem. Soc.*, 2008, **130**, 5854–5855.
62 T. Devic, P. Horcajada, C. Serre, F. Salles, G. Maurin, B. Moulin, D. Heurtaux, G. Clet, A. Vimont, J.-M. Grenèche, B. Le Ouay, F. Moreau, E. Magnier, Y. Filinchuk, J. Marrot, J.-C. Lavalley, M. Daturi and G. Férey, *J. Am. Chem. Soc.*, 2010, **132**, 1127–1136.
63 P. Horcajada, F. Salles, S. Wuttke, T. Devic, D. Heurtaux, G. Maurin, A. Vimont, M. Daturi, O. David, E. Magnier, N. Stock, Y. Filinchuk, D. Popov, C. Riekel, G. Férey and C. Serre, *J. Am. Chem. Soc.*, 2011, **133**, 17839–17847.
64 M. Kandiah, M. H. Nilsen, S. Usseglio, S. Jakobsen, U. Olsbye, M. Tilset, C. Larabi, E. A. Quadrelli, F. Bonino and K. P. Lillerud, *Chem. Mater.*, 2010, **22**, 6632–6640.
65 D. J. Lun, G. I. N. Waterhouse and S. G. Telfer, *J. Am. Chem. Soc.*, 2011, **133**, 5806–5809.
66 S. M. Cohen, *J. Am. Chem. Soc.*, 2017, **139**, 2855–2863.
67 R. J. White, R. Luque, V. L. Budarin, J. H. Clark and D. J. Macquarrie, *Chem. Soc. Rev.*, 2009, **38**, 481–494.
68 S. Goel, Z. Wu, S. I. Zones and E. Iglesia, *J. Am. Chem. Soc.*, 2012, **134**, 17688–17695.
69 Q.-L. Zhu and Q. Xu, *Chem*, 2016, **1**, 220–245.
70 A. Dhakshinamoorthy and H. Garcia, *Chem. Soc. Rev.*, 2012, **41**, 5262–5284.
71 H. R. Moon, D.-W. Limb and M. P. Suh, *Chem. Soc. Rev.*, 2013, **42**, 1807–1824.
72 M. Meilikhov, K. Yusenko, D. Esken, S. Turner, G. V. Tendeloo and R. A. Fischer, *Eur. J. Inorg. Chem.*, 2010, 3701–3714.
73 A. Aijaz and Q. Xu, *J. Phys. Chem. Lett.*, 2014, **5**, 1400–1411.
74 C. Röslera and R. A. Fischer, *CrystEngComm*, 2015, **17**, 199–217.
75 C. R. Kim, T. Uemura and S. Kitagawa, *Chem. Soc. Rev.*, 2016, **45**, 3828–3845.
76 Y. Liu and Z. Tang, *Adv. Mater.*, 2013, **25**, 5819–5825.
77 Y. Zhang, Y. Zhou, Y. Zhao and C.-J. Liu, *Catal. Today*, 2016, **263**, 61–68.
78 B. Rungtaweevoranit, Y. Zhao, K. M. Choi and O. M. Yaghi, *Nano Res.*, 2016, **9**, 47–58.

79 H. Kobayashi, Y. Mitsuka and H. Kitagawa, *Inorg. Chem.*, 2016, **55**, 7301–7310.
80 A. Dhakshinamoorthy, A. M. Asiri and H. Garcia, *ACS Catal.*, 2017, **7**, 2896–2919.
81 Q. Yang, Q. Xu, S.-H. Yu and H.-L. Jiang, *Angew. Chem., Int. Ed.*, 2016, **55**, 3685–3689.
82 Y.-Z. Chen, Y.-X. Zhou, H. Wang, J. Lu, T. Uchida, Q. Xu, S.-H. Yu and H.-L. Jiang, *ACS Catal.*, 2015, **5**, 2062–2069.
83 Y.-Z. Chen, Z. U. Wang, H. Wang, J. Lu, S.-H. Yu and H.-L. Jiang, *J. Am. Chem. Soc.*, 2017, **139**, 2035–2044.
84 M. Sabo, A. Henschel, H. Froede, E. Klemm and S. Kaskel, *J. Mater. Chem.*, 2007, **17**, 3827–3832.
85 Y. Pan, B. Yuan, Y. Li and D. He, *Chem. Commun.*, 2010, **46**, 2280–2282.
86 Y. Huang, Z. Lin and R. Cao, *Chem. – Eur. J.*, 2011, **17**, 12706–12712.
87 Y. Zhao, J. Zhang, J. Song, J. Li, J. Liu, T. Wu, P. Zhang and B. Han, *Green Chem.*, 2011, **13**, 2078–2082.
88 H. Khajavi, H. A. Stil, H. P. C. E. Kuipers, J. Gascon and F. Kapteijn, *ACS Catal.*, 2013, **3**, 2617–2626.
89 B. Yuan, Y. Pan, Y. Li, B. Yin and H. Jiang, *Angew. Chem., Int. Ed.*, 2010, **49**, 4054–4058.
90 Y. Huang, S. Liu, Z. Lin, W. Li, X. Li and R. Cao, *J. Catal.*, 2012, **292**, 111–117.
91 G. Huang, Q. Yang, Q. Xu, S.-H. Yu and H.-L. Jiang, *Angew. Chem., Int. Ed.*, 2016, **55**, 7379–7383.
92 C. Zlotea, R. Campesi, F. Cuevas, E. Leroy, P. Dibandjo, C. Volkringer, T. Loiseau, G. Férey and M. Latroche, *J. Am. Chem. Soc.*, 2010, **132**, 2991–2997.
93 W.-T. Koo, S.-J. Choi, S.-J. Kim, J.-S. Jang, H. L. Tuller and I.-D. Kim, *J. Am. Chem. Soc.*, 2016, **138**, 13431–13437.
94 B. Volosskiy, K. Niwa, Y. Chen, Z. Zhao, N. O. Weiss, X. Zhong, M. Ding, C. Lee, Y. Huang and X. Duan, *ACS Nano*, 2015, **9**, 3044–3049.
95 M. S. El-Shall, V. Abdelsayed, A. E. R. S. Khder, H. M. A. Hassan, H. M. El-Kaderi and T. E. Reich, *J. Mater. Chem.*, 2009, **19**, 7625–7631.
96 H.-L. Jiang, T. Akita, T. Ishida, M. Haruta and Q. Xu, *J. Am. Chem. Soc.*, 2011, **133**, 1304–1306.
97 Y. K. Hwang, D. Y. Hong, J. S. Chang, S. H. Jhung, Y.-K. Seo, J. Kim, A. Vimont, M. Daturi, C. Serre and G. Férey, *Angew. Chem., Int. Ed.*, 2008, **47**, 4144–4148.
98 X. Gu, Z.-H. Lu, H.-L. Jiang, T. Akita and Q. Xu, *J. Am. Chem. Soc.*, 2011, **133**, 11822–11825.
99 Z. Guo, C. Xiao, R. V. Maligal-Ganesh, L. Zhou, T. W. Goh, X. Li, D. Tesfagaber, A. Thiel and W. Huang, *ACS Catal.*, 2014, **4**, 1340–1348.
100 B. Gole, U. Sanyal and P. S. Mukherjee, *Chem. Commun.*, 2015, **51**, 4872–4875.
101 B. Gole, U. Sanyal, R. Banerjee and P. S. Mukherjee, *Inorg. Chem.*, 2016, **55**, 2345–2354.
102 Y.-Z. Chen, L. Liang, Q. Yang, M. Hong, Q. Xu, S.-H. Yu and H.-L. Jiang, *Mater. Horiz.*, 2015, **2**, 606–612.
103 H. R. Moon, J. H. Kim and M. P. Suh, *Angew. Chem., Int. Ed.*, 2005, **44**, 1261–1265.
104 M. P. Suh, H. R. Moon, E. Y. Lee and S. Y. Jang, *J. Am. Chem. Soc.*, 2006, **128**, 4710–4718.
105 Y. E. Cheon and M. P. Suh, *Chem. – Eur. J.*, 2008, **14**, 3961–3967.
106 Y. E. Cheon and M. P. Suh, *Angew. Chem., Int. Ed.*, 2009, **48**, 2899–2903.
107 Y. Wei, S. Han, D. A. Walker, P. E. Fuller and B. A. Grzybowski, *Angew. Chem., Int. Ed.*, 2012, **51**, 7435–7439.
108 L. Shen, M. Luo, L. Huang, P. Feng and L. Wu, *Inorg. Chem.*, 2015, **54**, 1191–1193.
109 C. Wang, K. E. deKrafft and W. Lin, *J. Am. Chem. Soc.*, 2012, **134**, 7211–7214.
110 Y. Horiuchi, T. Toyao, M. Saito, K. Mochizuki, M. Iwata, H. Higashimura, M. Anpo and M. Matsuoka, *J. Phys. Chem. C*, 2012, **116**, 20848–20853.
111 R. Liang, F. Jing, L. Shen, N. Qin and L. Wu, *Nano Res.*, 2015, **8**, 3237–3249.
112 H.-X. Zhang, M. Liu, X. Bu and J. Zhang, *Sci. Rep.*, 2014, **4**, 3923.
113 A. Aijaz, A. Karkamkar, Y. J. Choi, N. Tsumori, E. Rönnebro, T. Autrey, H. Shioyama and Q. Xu, *J. Am. Chem. Soc.*, 2012, **134**, 13926–13929.
114 Q. Yang, Y.-Z. Chen, Z. U. Wang, Q. Xu and H.-L. Jiang, *Chem. Commun.*, 2015, **51**, 10419–10422.
115 D. Sun and Z. Li, *J. Phys. Chem. C*, 2016, **120**, 19744–19750.
116 A. Dhankhar, R. K. Rai, D. Tyagi, X. Yao and S. K. Singh, *ChemistrySelect*, 2016, **1**, 3223–3227.
117 Q.-L. Zhu, J. Li and Q. Xu, *J. Am. Chem. Soc.*, 2013, **135**, 10210–10213.
118 Y.-Z. Chen, Q. Xu, S.-H. Yu and H.-L. Jiang, *Small*, 2015, **11**, 71–76.
119 S. Hermes, M.-K. Schröter, R. Schmid, L. Khodeir, M. Muhler, A. Tissler, R. W. Fischer and R. A. Fischer, *Angew. Chem., Int. Ed.*, 2005, **44**, 6237–6241.
120 F. Schröder, D. Esken, M. Cokoja, M. W. E. van den Berg, O. I. Lebedev, G. Van Tendeloo, B. Walaszek, G. Buntkowsky, H.-H. Limbach, B. Chaudret and R. A. Fischer, *J. Am. Chem. Soc.*, 2008, **130**, 6119–6130.
121 M. Müller, S. Hermes, K. Kähler, M. W. E. van den Berg, M. Muhler and R. A. Fischer, *Chem. Mater.*, 2008, **20**, 4576–4587.
122 F. Schröder, S. Henke, X. Zhang and R. A. Fischer, *Eur. J. Inorg. Chem.*, 2009, 3131–3140.
123 S. Hermes, F. Schröder, S. Amirjalayer, R. Schmid and R. A. Fischer, *J. Mater. Chem.*, 2006, **16**, 2464–2472.
124 S. Proch, J. Hermannsdörfer, R. Kempe, C. Kern, A. Jess, L. Seyfarth and J. Senker, *Chem. – Eur. J.*, 2008, **14**, 8204–8212.
125 M. Müller, O. I. Lebedev and R. A. Fischer, *J. Mater. Chem.*, 2008, **18**, 5274–5281.
126 J. Hermannsdöfer and R. Kempe, *Chem. – Eur. J.*, 2011, **17**, 8071–8077.
127 J. Hermannsdörfer, M. Friedrich, N. Miyajima, R. Q. Albuquerque, S. Kümmel and R. Kempe, *Angew. Chem., Int. Ed.*, 2012, **51**, 11473–11477.
128 P. Z. Li, K. Aranishi and Q. Xu, *Chem. Commun.*, 2012, **48**, 3173–3175.

 

129 Y. K. Park, S. B. Choi, H. J. Nam, D.-Y. Jung, H. C. Ahn, K. Choi, H. Furukawa and J. Kim, *Chem. Commun.*, 2010, **46**, 3086–3088.
130 D.-W. Lim, J. W. Yoon, K. Y. Ryu and M. P. Suh, *Angew. Chem., Int. Ed.*, 2012, **51**, 9814–9817.
131 T. Ishida, M. Nagaoka, T. Akita and M. Haruta, *Chem. – Eur. J.*, 2008, **14**, 8456–8460.
132 T. Ishida, N. Kawakita, T. Akita and M. Haruta, *Gold Bull.*, 2009, **42**, 267–274.
133 H.-L. Jiang, B. Liu, T. Akita, M. Haruta, H. Sakurai and Q. Xu, *J. Am. Chem. Soc.*, 2009, **131**, 11302–11303.
134 H.-L. Jiang, Q.-P. Lin, T. Akita, B. Liu, H. Ohashi, H. Oji, T. Honma, T. Takei, M. Haruta and Q. Xu, *Chem. – Eur. J.*, 2011, **17**, 78–81.
135 M. Mukoyoshi, H. Kobayashi, K. Kusada, M. Hayashi, T. Yamada, M. Maesato, J. M. Taylor, Y. Kubota, K. Kato, M. Takata, T. Yamamoto, S. Matsumura and H. Kitagawa, *Chem. Commun.*, 2015, **51**, 12463–12466.
136 G. Li, H. Kobayashi, K. Kusada, J. M. Taylor, Y. Kubota, K. Kato, M. Takata, T. Yamamoto, S. Matsumura and H. Kitagawa, *Chem. Commun.*, 2014, **50**, 13750–13753.
137 K. Sugikawa, Y. Furukawa and K. Sada, *Chem. Mater.*, 2011, **23**, 3132–3134.
138 T. Tsuruoka, H. Kawasaki, H. Nawafune and K. Akamatsu, *ACS Appl. Mater. Interfaces*, 2011, **3**, 3788–3791.
139 G. Maurin-Pasturel, J. Long, Y. Guari, F. Godiard, M.-G. Willinger, C. Guerin and J. Larionova, *Angew. Chem., Int. Ed.*, 2014, **53**, 3872–3876.
140 G. Lu, S. Li, Z. Guo, O. K. Farha, B. G. Hauser, X. Qi, Y. Wang, X. Wang, S. Han, X. Liu, J. S. DuChene, H. Zhang, Q. Zhang, X. Chen, J. Ma, S. C. J. Loo, W. D. Wei, Y. Yang, J. T. Hupp and F. Huo, *Nat. Chem.*, 2012, **4**, 310–316.
141 T. Ohhashi, T. Tsuruoka, T. Matsuyama, Y. Takashima, H. Nawafune, H. Minami and K. Akamatsu, *J. Colloid Interface Sci.*, 2015, **451**, 212–215.
142 H. Jiang, Q. Yan, R. Chen and W. Xing, *Microporous Mesoporous Mater.*, 2016, **225**, 33–40.
143 W. Zhang, G. Lu, C. Cui, Y. Liu, S. Li, W. Yan, C. Xing, Y. R. Chi, Y. Yang and F. Huo, *Adv. Mater.*, 2014, **26**, 4056–4060.
144 H. Li, M. R. Hill, C. Doblin, S. Lim, A. J. Hill and P. Falcaro, *Adv. Funct. Mater.*, 2016, **26**, 4815–4821.
145 G. Li, H. Kobayashi, J. M. Taylor, R. Ikeda, Y. Kubota, K. Kato, M. Takata, T. Yamamoto, S. Toh, S. Matsumura and H. Kitagawa, *Nat. Mater.*, 2014, **13**, 802–806.
146 M. Zhao, K. Deng, L. He, Y. Liu, G. Li, H. Zhao and Z. Tang, *J. Am. Chem. Soc.*, 2014, **136**, 1738–1741.
147 X. Liu, L. He, J. Zheng, J. Guo, F. Bi, X. Ma, K. Zhao, Y. Liu, R. Song and Z. Tang, *Adv. Mater.*, 2015, **27**, 3273–3277.
148 W. Zhang, L. Wang, K. Wang, M. U. Khan, M. Wang, H. Li and J. Zeng, *Small*, 2017, **13**, DOI: 10.1002/smll.201602583.
149 J.-D. Xiao, Q. Shang, Y. Xiong, Q. Zhang, Y. Luo, S.-H. Yu and H.-L. Jiang, *Angew. Chem., Int. Ed.*, 2016, **55**, 9389–9393.
150 Z. Gu, L. Chen, B. Duan, Q. Luo, J. Liu and C. Duan, *Chem. Commun.*, 2016, **52**, 116–119.
151 B. Rungtaweevoranit, J. Baek, J. R. Araujo, B. S. Archanjo, K. M. Choi, O. M. Yaghi and G. A. Somorjai, *Nano Lett.*, 2016, **16**, 7645–7649.
152 K. M. Choi, D. Kim, B. Rungtaweevoranit, C. A. Trickett, J. T. D. Barmanbek, A. S. Alshammari, P. Yang and O. M. Yaghi, *J. Am. Chem. Soc.*, 2017, **139**, 356–362.
153 F. Ke, J. Zhu, L.-G. Qiu and X. Jiang, *Chem. Commun.*, 2013, **49**, 1267–1269.
154 F. Ke, L. Wang and J. Zhu, *Nanoscale*, 2015, **7**, 1201–1208.
155 J. Zhou, P. Wang, C. Wang, Y. T. Goh, Z. Fang, P. B. Messersmith and H. Duan, *ACS Nano*, 2015, **9**, 6951–6960.
156 P. Hu, J. Zhuang, L.-Y. Chou, H. K. Lee, X. Y. Ling, Y.-C. Chuang and C.-K. Tsung, *J. Am. Chem. Soc.*, 2014, **136**, 10561–10564.
157 G. Zheng, S. de Marchi, V. López-Puente, K. Sentosun, L. Polavarapu, I. Pérez-Juste, E. H. Hill, S. Bals, L. M. Liz-Marzán, I. Pastoriza-Santos and J. Pérez-Juste, *Small*, 2016, **12**, 3935–3943.
158 P. Wang, J. Zhao, X. Li, Y. Yang, Q. Yang and C. Li, *Chem. Commun.*, 2013, **49**, 3330–3332.
159 K. Khaletskaya, J. Reboul, M. Meilikhov, M. Nakahama, S. Diring, M. Tsujimoto, S. Isoda, F. Kim, K. I. Kamei, R. A. Fischer, S. Kitagawa and S. Furukawa, *J. Am. Chem. Soc.*, 2013, **135**, 10998–11005.
160 Y. Zhao, N. Kornienko, Z. Liu, C. Zhu, S. Asahina, T.-R. Kuo, W. Bao, C. Xie, A. Hexemer, O. Terasaki, P. Yang and O. M. Yaghi, *J. Am. Chem. Soc.*, 2015, **137**, 2199–2202.
161 Z. Li, R. Yu, J. Huang, Y. Shi, D. Zhang, X. Zhong, D. Wang, Y. Wu and Y. Li, *Nat. Commun.*, 2015, **6**, 8248.
162 L. Chen, H. Li, W. Zhan, Z. Cao, J. Chen, Q. Jiang, Y. Jiang, Z. Xie, Q. Kuang and L. Zheng, *ACS Appl. Mater. Interfaces*, 2016, **8**, 31059–31066.
163 I. Luz, A. Loiudice, D. T. Sun, W. L. Queen and R. Buonsanti, *Chem. Mater.*, 2016, **28**, 3839–3849.
164 M. Sindoro and S. Granick, *J. Am. Chem. Soc.*, 2014, **136**, 13471–13473.
165 C.-H. Kuo, Y. Tang, L.-Y. Chou, B. T. Sneed, C. N. Brodsky, Z. Zhao and C.-K. Tsung, *J. Am. Chem. Soc.*, 2012, **134**, 14345–14348.
166 Y. Liu, J. Zhang, L. Song, W. Xu, Z. Guo, X. Yang, X. Wu and X. Chen, *ACS Appl. Mater. Interfaces*, 2016, **8**, 22745–22750.
167 Y. Liu, T. Liu, L. Tian, L. Zhang, L. Yao, T. Tan, J. Xu, X. Han, D. Liu and C. Wang, *Nanoscale*, 2016, **8**, 19075–19085.
168 X. Wang, M. Li, C. Cao, C. Liu, J. Liu, Y. Zhu, S. Zhang and W. Song, *ChemCatChem*, 2016, **8**, 3224–3228.
169 S. Wang, Y. Fan, J. Teng, Y.-Z. Fan, J.-J. Jiang, H.-P. Wang, H. Grützmacher, D. Wang and C.-Y. Su, *Small*, 2016, **12**, 5702–5709.
170 Y. Yang, F. Wang, Q. Yang, Y. Hu, H. Yan, Y.-Z. Chen, H. Liu, G. Zhang, J. Lu, H.-L. Jiang and H. Xu, *ACS Appl. Mater. Interfaces*, 2014, **6**, 18163–18171.
171 J. Long, H. Liu, S. Wu, S. Liao and Y. Li, *ACS Catal.*, 2013, **3**, 647–654.
172 M. Zhao, K. Yuan, Y. Wang, G. Li, J. Guo, L. Gu, W. Hu, H. Zhao and Z. Tang, *Nature*, 2016, **539**, 76–80.
173 H. Liu, L. Chang, L. Chen and Y. Li, *ChemCatChem*, 2016, **8**, 946–951.

174 L. He, Y. Liu, J. Liu, Y. Xiong, J. Zheng, Y. Liu and Z. Tang, *Angew. Chem., Int. Ed.*, 2013, **52**, 3741–3745.
175 F. Ke, L. Wang and J. Zhu, *Nanoscale*, 2015, **7**, 8321–8325.
176 L. Chen, H. Chen, R. Luque and Y. Li, *Chem. Sci.*, 2014, **5**, 3708–3714.
177 H. Liu, L. Chang, C. Bai, L. Chen, R. Luque and Y. Li, *Angew. Chem., Int. Ed.*, 2016, **55**, 5019–5023.
178 H. Liu, L. Chang, L. Chen and Y. Li, *J. Mater. Chem. A*, 2015, **3**, 8028–8033.
179 R. J. T. Houk, B. W. Jacobs, F. El Gabaly, N. N. Chang, A. A. Talin, D. D. Graham, S. D. House, I. M. Robertson and M. D. Allendorf, *Nano Lett.*, 2009, **9**, 3413–3418.
180 L. Chen, B. Huang, X. Qiu, X. Wang, R. Luque and Y. Li, *Chem. Sci.*, 2016, **7**, 228–233.
181 X. Li, Z. Guo, C. Xiao, T. W. Goh, D. Tesfagaber and W. Huang, *ACS Catal.*, 2014, **4**, 3490–3497.
182 S. Turner, O. I. Lebedev, F. Schröder, D. Esken, R. A. Fischer and G. Van Tendeloo, *Chem. Mater.*, 2008, **20**, 5622–5627.
183 L. Chen, X. Chen, H. Liu and Y. Li, *Small*, 2015, **11**, 2642–2648.
184 Y. Bai, Y. Dou, L.-H. Xie, W. Rutledge, J.-R. Li and H.-C. Zhou, *Chem. Soc. Rev.*, 2016, **45**, 2327–2367.
185 J. H. Cavka, S. Jakobsen, U. Olsbye, N. Guillou, C. Lamberti, S. Bordiga and K. P. Lillerud, *J. Am. Chem. Soc.*, 2008, **130**, 13850–13851.
186 H.-L. Jiang, D. Feng, K. Wang, Z.-Y. Gu, Z. Wei, Y.-P. Chen and H.-C. Zhou, *J. Am. Chem. Soc.*, 2013, **135**, 13934–13938.
187 D. Esken, S. Turner, O. I. Lebedev, G. Van Tendeloo and R. A. Fischer, *Chem. Mater.*, 2010, **22**, 6393–6401.
188 A. Aijaz, T. Akita, N. Tsumori and Q. Xu, *J. Am. Chem. Soc.*, 2013, **135**, 16356–16359.
189 S. Gao, N. Zhao, M. Shu and S. Che, *Appl. Catal., A*, 2010, **388**, 196–201.
190 H. Li, Z. Zhu, F. Zhang, S. Xie, H. Li, P. Li and X. Zhou, *ACS Catal.*, 2011, **1**, 1604–1612.
191 M. Yadav and Q. Xu, *Chem. Commun.*, 2013, **49**, 3327–3329.
192 Y. Huang, T. Ma, P. Huang, D. Wu, Z. Lin and R. Cao, *ChemCatChem*, 2013, **5**, 1877–1883.
193 N. Cao, L. Yang, H. Dai, T. Liu, J. Su, X. Wu, W. Luo and G. Cheng, *Inorg. Chem.*, 2014, **53**, 10122–10128.
194 C. Hou, G. Zhao, Y. Ji, Z. Niu, D. Wang and Y. Li, *Nano Res.*, 2014, **7**, 1364–1369.
195 V. Pascanu, F. Carson, M. V. Solano, J. Su, X. Zou, M. J. Johansson and B. Martín-Matute, *Chem. – Eur. J.*, 2016, **22**, 3729–3737.
196 F. Carson, V. Pascanu, A. Bermejo Gómez, Y. Zhang, A. E. Platero-Prats, X. Zou and B. Martín-Matute, *Chem. – Eur. J.*, 2015, **21**, 10896–10902.
197 S.-T. Gao, W.-H. Liu, N.-Z. Shang, C. Feng, Q.-H. Wu, Z. Wang and C. Wang, *RSC Adv.*, 2014, **4**, 61736–61742.
198 Y.-A. Li, S. Yang, Q.-K. Liu, G.-J. Chen, J.-P. Ma and Y.-B. Dong, *Chem. Commun.*, 2016, **52**, 6517–6520.
199 X. Zhao, Y. Jin, F. Zhang, Y. Zhong and W. Zhu, *Chem. Eng. J.*, 2014, **239**, 33–41.
200 H. Zhao, H. Song and L. Chou, *Inorg. Chem. Commun.*, 2012, **15**, 261–265.
201 J. Hermannsdörfer, M. Friedrich and R. Kempe, *Chem. – Eur. J.*, 2013, **19**, 13652–13657.
202 R. Fang, H. Liu, R. Luque and Y. Li, *Green Chem.*, 2015, **17**, 4183–4188.
203 J. Chen, R. Liu, Y. Guo, L. Chen and H. Gao, *ACS Catal.*, 2015, **5**, 722–733.
204 I. E. Ertas, M. Gulcan, A. Bulut, M. Yurderi and M. Zahmakiran, *Microporous Mesoporous Mater.*, 2016, **226**, 94–103.
205 Y. Qi, Y. Luan, X. Peng, M. Yang, J. Hou and G. Wang, *Eur. J. Inorg. Chem.*, 2015, 5099–5105.
206 I. E. Ertas, M. Gulcan, A. Bulut, M. Yurderi and M. Zahmakiran, *J. Mol. Catal. A: Chem.*, 2015, **410**, 209–220.
207 G.-l. Zhuang, J.-q. Bai, X. Zhou, Y.-f. Gao, H.-l. Huang, H.-q. Cui, X. Zhong, C.-L. Zhong and J.-g. Wang, *Eur. J. Inorg. Chem.*, 2017, 172–178.
208 P. Huang, W. Ma, P. Yu and L. Mao, *Chem. – Asian J.*, 2016, **11**, 2705–2709.
209 X. Liu, X. Zhao, M. Zhou, Y. Cao, H. Wu and J. Zhu, *Eur. J. Inorg. Chem.*, 2016, 3338–3343.
210 N.-Z. Shang, C. Feng, S.-T. Gao and C. Wang, *Int. J. Hydrogen Energy*, 2016, **41**, 944–950.
211 L. Liu, Y. Song, H. Chong, S. Yang, J. Xiang, S. Jin, X. Kang, J. Zhang, H. Yua and M. Zhu, *Nanoscale*, 2016, **8**, 1407–1412.
212 L. Chen, W. Huang, X. Wang, Z. Chen, X. Yang, R. Luque and Y. Li, *Chem. Commun.*, 2017, **53**, 1184–1187.
213 F. Zhang, Y. Jin, Y. Fu, Y. Zhong, W. Zhu, A. A. Ibrahim and M. S. El-Shall, *J. Mater. Chem. A*, 2015, **3**, 17008–17015.
214 F. Zhang, S. Zheng, Q. Xiao, Y. Zhong, W. Zhu, A. Lin and M. Samy El-Shall, *Green Chem.*, 2016, **18**, 2900–2908.
215 M. Zhang, J. Guan, B. Zhang, D. Su, C. T. Williams and C. Liang, *Catal. Lett.*, 2012, **142**, 313–318.
216 J. Juan-Alcañiz, J. Ferrando-Soria, I. Luz, P. Serra-Crespo, E. Skupien, V. P. Santos, E. Pardo, F. X. Llabrés i Xamena, F. Kapteijn and J. Gascon, *J. Catal.*, 2013, **307**, 295–304.
217 V. Pascanu, Q. Yao, A. B. Gómez, M. Gustafsson, Y. Yun, W. Wan, L. Samain, X. Zou and B. Martín-Matute, *Chem. – Eur. J.*, 2013, **19**, 17483–17493.
218 Y. Huang, Z. Zheng, T. Liu, J. Lü, Z. Lin, H. Li and R. Cao, *Catal. Commun.*, 2011, **14**, 27–31.
219 Y. Huang, S. Gao, T. Liu, J. Lü, X. Lin, H. Li and R. Cao, *ChemPlusChem*, 2012, **77**, 106–112.
220 K. Jayaramulu, K. K. R. Datta, M. V. Suresh, G. Kumari, R. Datta, C. Narayana, M. Eswaramoorthy and T. K. Maji, *ChemPlusChem*, 2012, **77**, 743–747.
221 L. Liu, X. Zhang, J. Gao and C. Xu, *Green Chem.*, 2012, **14**, 1710–1720.
222 S. Wang, X. He, L. Song and Z. Wang, *Synlett*, 2009, 447–450.
223 Z. Li and H. C. Zeng, *Chem. Mater.*, 2013, **25**, 1761–1768.
224 Y. Wan, C. Chen, W. Xiao, L. Jian and N. Zhang, *Microporous Mesoporous Mater.*, 2013, **171**, 9–13.
225 P. Liu, X. Gu, K. Kang, H. Zhang, J. Cheng and H. Su, *ACS Appl. Mater. Interfaces*, 2017, **9**, 10759–10767.
226 H.-L. Jiang, S. K. Singh, J.-M. Yan, X.-B. Zhang and Q. Xu, *ChemSusChem*, 2010, **3**, 541–549.
227 M. Martis, K. Mori, K. Fujiwara, W.-S. Ahn and H. Yamashita, *J. Phys. Chem. C*, 2013, **117**, 22805–22810.

 

228 H. Liu, Y. Liu, Y. Li, Z. Tang and H. Jiang, *J. Phys. Chem. C*, 2010, **114**, 13362–13369.
229 V. Pascanu, A. Bermejo Gómez, C. Ayats, A. E. Platero-Prats, F. Carson, J. Su, Q. Yao, M. À. Pericàs, X. Zou and B. Martín-Matute, *ACS Catal.*, 2015, **5**, 472–479.
230 G.-J. Chen, J.-S. Wang, F.-Z. Jin, M.-Y. Liu, C.-W. Zhao, Y.-A. Li and Y.-B. Dong, *Inorg. Chem.*, 2016, **55**, 3058–3064.
231 D. Tilgner, M. Friedrich, J. Hermannsdörfer and R. Kempe, *ChemCatChem*, 2015, **7**, 3916–3922.
232 G. Chen, S. Wu, H. Liu, H. Jiang and Y. Li, *Green Chem.*, 2013, **15**, 230–235.
233 L. Chen, Y. Peng, H. Wang, Z. Gu and C. Duan, *Chem. Commun.*, 2014, **50**, 8651–8654.
234 Y.-B. Huang, M. Shen, X. Wang, P.-C. Shi, H. Li and R. Cao, *J. Catal.*, 2015, **330**, 452–457.
235 B. Xi, Y. C. Tan and H. C. Zeng, *Chem. Mater.*, 2016, **28**, 326–336.
236 Z. Xu, W. Zhang, J. Weng, W. Huang, D. Tian and F. Huo, *Nano Res.*, 2016, **9**, 158–164.
237 C. J. Stephenson, J. T. Hupp and O. K. Farha, *Inorg. Chem.*, 2016, **55**, 1361–1363.
238 C. J. Stephenson, J. T. Hupp and O. K. Farha, *Inorg. Chem. Front.*, 2015, **2**, 448–452.
239 S. Aguado, S. El-Jamal, F. Meunier, J. Canivet and D. Farrusseng, *Chem. Commun.*, 2016, **52**, 7161–7163.
240 Y.-Z. Chen, G. Cai, Y. Wang, Q. Xu, S.-H. Yu and H.-L. Jiang, *Green Chem.*, 2016, **18**, 1212–1217.
241 A. Aijaz, Q.-L. Zhu, N. Tsumori, T. Akita and Q. Xu, *Chem. Commun.*, 2015, **51**, 2577–2580.
242 W. Zhang, G. Lu, S. Li, Y. Liu, H. Xu, C. Cui, W. Yan, Y. Yang and F. Huo, *Chem. Commun.*, 2014, **50**, 4296–4298.
243 Y. Liu, W. Zhang, S. Li, C. Cui, J. Wu, H. Chen and F. Huo, *Chem. Mater.*, 2014, **26**, 1119–1125.
244 T. T. Dang, Y. Zhu, S. C. Ghosh, A. Chen, C. L. L. Chai and A. M. Seayad, *Chem. Commun.*, 2012, **48**, 1805–1807.
245 Z. Zhang, Y. Chen, S. He, J. Zhang, X. Xu, Y. Yang, F. Nosheen, F. Saleem, W. He and X. Wang, *Angew. Chem., Int. Ed.*, 2014, **53**, 12517–12521.
246 X. Huang, B. Zheng, Z. Liu, C. Tan, J. Liu, B. Chen, H. Li, J. Chen, X. Zhang, Z. Fan, W. Zhang, Z. Guo, F. Huo, Y. Yang, L.-H. Xie, W. Huang and H. Zhang, *ACS Nano*, 2014, **8**, 8695–8701.
247 H. Liu, Y. Li, R. Luque and H. Jiang, *Adv. Synth. Catal.*, 2011, **353**, 3107–3113.
248 L. Chen, H. Chen and Y. Li, *Chem. Commun.*, 2014, **50**, 14752–14755.
249 Z. Zhang, Y. Chen, X. Xu, J. Zhang, G. Xiang, W. He and X. Wang, *Angew. Chem., Int. Ed.*, 2014, **53**, 429–433.
250 Y. Pan, D. Ma, H. Liu, H. Wu, D. He and Y. Li, *J. Mater. Chem.*, 2012, **22**, 10834–10839.
251 S. Opelt, S. Türk, E. Dietzsch, A. Henschel, S. Kaskel and E. Klemm, *Catal. Commun.*, 2008, **9**, 1286–1290.
252 L. Chen, X. Chen, H. Liu, C. Bai and Y. Li, *J. Mater. Chem. A*, 2015, **3**, 15259–15264.
253 W. Zhou, B. Zou, W. Zhang, D. Tian, W. Huang and F. Huo, *Nanoscale*, 2015, **7**, 8720–8724.
254 D. Teschner, J. Borsodi, A. Wootsch, Z. Révay, M. Hävecker, A. Knop-Gericke, S. D. Jackson and R. Schlögl, *Science*, 2008, **320**, 86–89.
255 M. Zahmakiran, *Dalton Trans.*, 2012, **41**, 12690–12696.
256 V. I. Isaeva, O. P. Tkachenko, E. V. Afonina, L. M. Kozlova, G. I. Kapustin, W. Grünert, S. E. Solov'eva, I. S. Antipin and L. M. Kustov, *Microporous Mesoporous Mater.*, 2013, **166**, 167–175.
257 X.-H. Liu, J.-G. Ma, Z. Niu, G.-M. Yang and P. Cheng, *Angew. Chem., Int. Ed.*, 2015, **54**, 988–991.
258 Y. Huang, Y. Zhang, X. Chen, D. Wu, Z. Yi and R. Cao, *Chem. Commun.*, 2014, **50**, 10115–10117.
259 R. Wu, X. Qian, K. Zhou, H. Liu, B. Yadian, J. Wei, H. Zhu and Y. Huang, *J. Mater. Chem. A*, 2013, **1**, 14294–14299.
260 P. Wang, J. Liu, C. Liu, B. Zheng, X. Zou, M. Jia and G. Zhu, *Chem. – Eur. J.*, 2016, **22**, 16613–16620.
261 K. M. Choi, K. Na, G. A. Somorjai and O. M. Yaghi, *J. Am. Chem. Soc.*, 2015, **137**, 7810–7816.
262 X. Li, T. W. Goh, L. Li, C. Xiao, Z. Guo, X. C. Zeng and W. Huang, *ACS Catal.*, 2016, **6**, 3461–3468.
263 Y.-B. Huang, M. Shen, X. Wang, P. Huang, R. Chen, Z.-J. Lin and R. Cao, *J. Catal.*, 2016, **333**, 1–7.
264 D. Sun, W. Liu, Y. Fu, Z. Fang, F. Sun, X. Fu, Y. Zhang and Z. Li, *Chem. – Eur. J.*, 2014, **20**, 4780–4788.
265 W. Guo, H. Lv, Z. Chen, K. P. Sullivan, S. M. Lauinger, Y. Chi, J. M. Sumliner, T. Lian and C. L. Hill, *J. Mater. Chem. A*, 2016, **4**, 5952–5957.
266 M. Wen, K. Mori, T. Kamegawa and H. Yamashita, *Chem. Commun.*, 2014, **50**, 11645–11648.
267 C. S. Hinde, W. R. Webb, B. K. J. Chew, H. R. Tan, W.-H. Zhang, T. S. A. Hor and R. Raja, *Chem. Commun.*, 2016, **52**, 6557–6560.
268 J.-S. Wang, F.-Z. Jin, H.-C. Ma, X.-B. Li, M.-Y. Liu, J.-L. Kan, G.-J. Chen and Y.-B. Dong, *Inorg. Chem.*, 2016, **55**, 6685–6691.
269 L. H. Wee, N. Janssens, S. P. Sree, C. Wiktor, E. Gobechiya, R. A. Fischer, C. E. A. Kirschhock and J. A. Martens, *Nanoscale*, 2014, **6**, 2056–2060.
270 Q. Liu, Z.-X. Low, L. Li, A. Razmjou, K. Wang, J. Yao and H. Wang, *J. Mater. Chem. A*, 2013, **1**, 11563–11569.
271 T. Zhang, X. Zhang, X. Yan, L. Kong, G. Zhang, H. Liu, J. Qiu and K. L. Yeung, *Chem. Eng. J.*, 2013, **228**, 398–404.
272 W. Wang, Y. Li, R. Zhang, D. He, H. Liu and S. Liao, *Catal. Commun.*, 2011, **12**, 875–879.
273 R. Li, J. Hu, M. Deng, H. Wang, X. Wang, Y. Hu, H.-L. Jiang, J. Jiang, Q. Zhang, Y. Xie and Y. Xiong, *Adv. Mater.*, 2014, **26**, 4783–4788.
274 S. Jung, Y. Kim, S.-J. Kim, T.-H. Kwon, S. Huh and S. Park, *Chem. Commun.*, 2011, **47**, 2904–2906.
275 V. Lykourinou, Y. Chen, X.-S. Wang, L. Meng, T. Hoang, L.-J. Ming, R. L. Musselman and S. Ma, *J. Am. Chem. Soc.*, 2011, **133**, 10382–10385.
276 W.-L. Liu, N.-S. Yang, Y.-T. Chen, S. Lirio, C.-Y. Wu, C.-H. Lin and H.-Y. Huang, *Chem. – Eur. J.*, 2015, **21**, 115–119.
277 J. Huo, J. Aguilera-Sigalat, S. El-Hankari and D. Bradshaw, *Chem. Sci.*, 2015, **6**, 1938–1943.

278 F. Lyu, Y. Zhang, R. N. Zare, J. Ge and Z. Liu, *Nano Lett.*, 2014, **14**, 5761–5765.
279 F.-K. Shieh, S.-C. Wang, C.-I. Yen, C.-C. Wu, S. Dutta, L.-Y. Chou, J. V. Morabito, P. Hu, M.-H. Hsu, K. C.-W. Wu and C.-K. Tsung, *J. Am. Chem. Soc.*, 2015, **137**, 4276–4279.
280 J. Aguilera-Sigalat and D. Bradshaw, *Coord. Chem. Rev.*, 2016, **307**, 267–291.
281 S. Saha, G. Das, J. Thote and R. Banerjee, *J. Am. Chem. Soc.*, 2014, **136**, 14845–14851.
282 L. Bromberg, Y. Diao, H. Wu, S. A. Speakman and T. A. Hatton, *Chem. Mater.*, 2012, **24**, 1664–1675.
283 N. V. Maksimchuk, K. A. Kovalenko, S. S. Arzumanov, Y. A. Chesalov, M. S. Melgunov, A. G. Stepanov, V. P. Fedin and O. A. Kholdeeva, *Inorg. Chem.*, 2010, **49**, 2920–2930.
284 J. Song, Z. Luo, D. K. Britt, H. Furukawa, O. M. Yaghi, K. I. Hardcastle and C. L. Hill, *J. Am. Chem. Soc.*, 2011, **133**, 16839–16846.
285 S.-S. Wang and G.-Y. Yang, *Chem. Rev.*, 2015, **115**, 4893–4962.
286 L. H. Wee, S. R. Bajpe, N. Janssens, I. Hermans, K. Houthoofd, C. E. A. Kirschhock and J. A. Martens, *Chem. Commun.*, 2010, **46**, 8186–8188.
287 X.-J. Kong, Z. Lin, Z.-M. Zhang, T. Zhang and W. Lin, *Angew. Chem., Int. Ed.*, 2016, **55**, 6411–6416.
288 Y. Zhang, V. Degirmenci, C. Li and E. J. M. Hensen, *ChemSusChem*, 2011, **4**, 59–64.
289 C.-Y. Sun, S.-X. Liu, D.-D. Liang, K.-Z. Shao, Y.-H. Ren and Z.-M. Su, *J. Am. Chem. Soc.*, 2009, **131**, 1883–1888.

 